Electronic Thesis and Dissertation Repository

8-29-2017 12:00 AM

Modelling the thermal conductivity of layered materials from photothermal measurements

Sina Kazemian, *The University of Western Ontario*

A thesis submitted in partial fulfillment of the requirements for the Doctor of Philosophy degree in Physics
© Sina Kazemian 2017

Follow this and additional works at: https://ir.lib.uwo.ca/etd

Abstract

The optimal methodology to determine the thermal properties of solids is particularly influenced by their thinness and morphology. As far as highly thermally conducting and ultra-thin layered materials on transparent and insulating substrates are concerned, contactless measurements that deposit a modest amount of heat on the sample are essential. In our thesis a combination of analytical and numerical solutions of Fourier's equation of heat is used, with the appropriate boundary conditions, for modelling the thermally modulated optical response of solids, in phase and amplitude, as a function of a their periodical illumination by a light beam that generates a heating of the thin-film substrate system at the same periodicity. Inverse solutions of Fourier's heat equation are required to extract the thermal conductivity and specific heat of the system in these cases. Two configurations are specifically considered. In the first configuration, in which the thermal properties are uniform at the macroscopic level in the directions orthogonal to the light beam, a photothermal deflection (PTD) configuration is considered and modeled under the assumption that the thermo-optical properties can be measured both from the thin film-side and the substrate-side of the system. We find that, on both sides, the phases of the PTD principally depend on the thermal diffusivity of the thin film, while the amplitudes also depend on the specific heat. In a second configuration, in which the thermal conductivity changes from point to point of the surface at the mesoscopic level, we developed a numerical method to solve Fourier's equation in configurations in which the thermo-optical properties are measured by scanning near-field optical techniques.

This configuration has been used graphene thin films decorated with a copper nanoparticle (Cu-NP) layer, before and after the deposition of Cu-NPs and after Cu-NP removal. In this system, we have been able to show that the decrease of thermal conductivity of graphene in contact to metal nanoparticles is due to phonon scattering by Dirac electrons in graphene, and not to metal-graphene interfacial thermal resistance, solving a long-standing debate in the literature. A description of this phenomenon in terms of diagrammatic quantum field theory will be offered.

Co-Authorship Statement

The work presented in Chapter 2 was done in collaboration with Dr. Reg Bauld. Dr. Reg Bauld ran the experiment on the PDS system which resulted in measuring the amplitude on the front and back side of the PDS system. I did the theoretical modeling. This work has not been published yet.

The work done on chapter 3 and 4 was done in collaboration with Dr. Sebastian Ezugwu. Dr. Sebastine Ezugwu ran the experiment on the NeSTRI system which resulted in measuring the amplitude, topography, reflectance and phase shift of the graphene flake. I did the theoretical modeling, the numerical modeling and acquired the thermal conductivity and heat capacity maps with the aforementioned data collected by Dr. Ezugwu. The work has been published in the nanoscale journal.

The work on chapter 5 was done in collaboration with Dr. Sebastian Ezugwu. Dr. Ezugwu ran the experiment on the NeSTRI system which resulted in measuring the amplitude, topography, reflectance and phase shift of the doped graphene flake. I did the theoretical modeling, the numerical modeling and acquired the thermal conductivity with the aforementioned data collected by Dr. Ezugwu. I also compared the thermal conductivity maps in the different phases of the experiment using several graphs. This work has not been published yet.

I have also been helped and assisted by Professor Giovanni Fanchini throughout chapters 2 to 6 with the theoretical and numerical modeling.

Acknowledgment

Firstly, I would like to express my sincere gratitude to my supervisor Prof. Giovanni Fanchini for the continuous support of my Ph.D. study and related research, for his patience, motivation, immense knowledge, and for all the stimulating discussions we had in the last four years. His guidance helped me in all the time of research and writing of this thesis. I could not have imagined having a better advisor and mentor for my Ph.D. study.

Besides Giovanni, I would like to thank my advisory committee Prof. Andrea Soddu and Prof. Eugene Wong, for their insightful comments and encouragement. I would also like to thank Professor Martin Houde for his help and support during the last 4 years.

I would like thank all my fellow colleagues and graduate students in Western University: Ghazal, Sahar, Bushra, Carolyn, Edith, Kendra, Zahra, Hoori, Masoud, Mark, James, Sayantan, Amir, Ali, Ezugwu, Matin, Pranav, Mohammed, Daniel, Tony, Dave, Sina, Neven, Jeff, Shahab, Yeh, William, Teeno, Arash, Dimuthu and Coco. You guys are amazing. Also, I would like to thank my three friends in London outside school: Don Hickey, John Fowler, and Michele.

My sincere thanks also goes to all my friends back home: Nikrooz, Yazdi, Roozbeh, Ali, Mohammad, Amir, Ehsan, Shayan, Sadra, Iman, Saeed, Younes, Shojaie, Ghuchani, and Hosein. You guys have always been helpful and supportive of me.

Last but not the least, I would like to thank my family: my parents, my aunts and my brother for all their help and support.

Dedicated to my Dearly Beloved Lili, Shahla, Nasrin & Simin

Table of Contents

List of Figures

List of Acronyms

SThM	Scanning thermal microscopy
NeSTRI	Near-field scanning thermoreflectance imaging
PDS	Photothermal deflection spectroscopy
SNOM	Scanning near-field optical spectroscopy
AFM	Atomic force microscopy

List of variables

$c(x,y)$	Heat capacity
$T(x,y,t)$	Temperature
$k_{th}(x,y)$	Thermal conductivity
$q_0(x,y,t)$	Heat generated per unit volume
$D(x,y)$	Thermal diffusivity
$J(x,y,t)$	Heat flow
$\varphi(x,y,t)$	Deflection angle of the PDS system
$\omega(t)$	Frequency
P_0	Power
η	Optical absorption coefficient
$Amp(\varphi)$	Amplitude of the deflected angle for the PDS system
$Ph(\varphi)$	Phase shift of the deflected angle for the PDS system
$d(x,y)$	Thickness
$H(x,y,t)$	Amount of heat locally deposited per unit volume
$\delta\rho(x,y)$	Amplitude of thermoreflectance oscillations for the NeSTRI system
$\delta\varphi(x,y)$	Phase lag for the NeSTRI system
$A_0(x,y)$	Samples absorptance
L_{th}	Thermal diffusion length
E	Electric field
$\boldsymbol{\mu}$	Magnetic moment
$\boldsymbol{p}$	Electric dipole moment
λ	Wavelength
k	Wavenumber
$\mathbf{S}$	Scattering matrix
$f(\theta,\varphi)$	Form factor
m	Optical constant coefficient
$\lambda(x,y)$	Thermal conductivity first order perturbation
$\theta(x,y,t)$	Temperature first order perturbation
$\varphi_{n,l}$	Phonon wave function

M_l	Mass of the atom
ε_λ	Phonon polarization vector
ω_q	Frequency of the lattice vibration
V_l	Thomas Fermi potential
V_Q	Thomas Fermi potential in the momentum space
$R_{n,l}$	Location of the ion in the unit cell
k	Electrons momentum
q	Phonons momentum
$S_F(x_2\text{-}x_1)$	Fermions propagator
v_f	Fermi velocity
W	Transition probability for the electron-phonon interaction
E_F	Energy of Dirac electrons
c_v	Specific heat of the phonon
c	Speed of sound inside a specific medium

"I do not know what I may appear to the world, but to myself I seem to have been only like a boy playing on the sea-shore, and diverting myself in now and then finding a smoother pebble or a prettier shell than ordinary, whilst the great ocean of truth lay all undiscovered before me."

Isaac Newton

Chapter 1

Background and literature review

1.1 Introduction

Recent years have seen a rapid growth of interest in the scientific communities in the thermal properties of materials. Heat removal has become a crucial issue for continuing progress in the electronics industry, and thermal conduction in low-dimensional structures has revealed truly intriguing features[1]. The search for systems composed of different materials that conduct heat well has become essential for the design of the next generation of integrated circuits and three-dimensional (3D) electronics[2]. Similar thermal issues have been encountered in optoelectronic and photonic devices[1].

A systems ability to conduct heat is rooted in, the microscopic atomic structure of its composed materials and their macroscopic configuration with respect to one another and the environment. Thermal conductivity is introduced through Fourier's heat equation which is[3, 4]:

$$c(x,y)\frac{\partial T(x,y,t)}{\partial t} - \nabla \cdot \left[k_{th}(x,y)\nabla T(x,y,t)\right] = -q(x,y,t) , \qquad (1.1)$$

where $T(x,y,t)$ is the temperature, $c(x,y)$ is the heat capacity and $k_{th}(x,y)$ is the thermal conductivity of the system. $q(x,y,t)$ is the heat generated per unit volume within the system. Eq. (1.1) is reminiscent of the conservation of energy in a homogeneous control region of solid, in which heat can be generated by the right-hand term of the equation, $c(x,y)(\partial T(x,y,t)/\partial t)$ is the amount of heat accumulated over time and $-\nabla \cdot [k_{th}(x,y)\nabla T(x,y,t)]$ is the amount of heat transferred or leaked through the control region boundaries. In solids, heat is carried by acoustic phonons which are, ion-core vibrations in a crystal lattice and electrons so $k_{th} = k_{th,p} + k_{th,e}$, where $k_{th,p}$ and $k_{th,e}$ are the phonon and electron contributions, respectively. In metals such as

copper, $k_{th,e}$ is dominant owing to large concentrations of free carriers while in carbon-based materials thermal conductivity is usually dominated by phonons[5].

The temperature profile in a homogeneous and isotropic system is governed by Fourier's heat equation which is[6]:

$$\frac{\partial^2 T(x,y,t)}{\partial x^2} + \frac{\partial^2 T(x,y,t)}{\partial y^2} = \frac{1}{D}\frac{\partial T(x,y,t)}{\partial t}, \tag{1.2}$$

where D is the thermal diffusivity that is assumed to be independent of the Euclidean coordinate axis x, y, and z and is defined as $D = k/c$. We write the temperature profile as a series of solutions with different eigenvalues and due to the linear characteristic of Fourier's equation, for which the principle of superposition is valid we are able to add and subtract the temperature profiles with each other. In the next sections, we will solve Fourier's heat equation in the presence of a harmonic heating pulse and study the macroscopic and microscopic nature of thermal conductivity in materials along with some examples from the state of art methods.

1.2.1 Fourier's heat equation in the presence of harmonic heating pulse

To find the equation of heat we first write the amount of heat flow within a system. Due to experiments, we know that the heat flow is proportional to the gradient of temperature[6]:

$$J(x,y,t) = -k(x,y)\nabla T(x,y,t). \tag{1.3}$$

By applying Stokes theorem[7] we get that the heat flowing out of volume V, bounded by a surface S, is:

$$\int_S \vec{J} \cdot \hat{n} dS = \int_V \nabla \cdot \vec{J} dV. \tag{1.4}$$

We write the total energy within the volume V as:

$$E = \int_V c(x,y)T(x,y,t)dV. \tag{1.5}$$

The rate of energy loss through the surface will be:

$$-\frac{\partial}{\partial t}\int_V cT dV = -c\int_V \frac{\partial T}{\partial t}dV. \tag{1.6}$$

Equating Eq. (1.6) and Eq. (1.8) we get:

$$\nabla \cdot J(x,y,t) = -c(x,y)\frac{\partial T(x,y,t)}{\partial t}, \tag{1.7}$$

and by substituting Eq. (1.9) into Eq. (1.5) we get:

$$\nabla^2 T(x,y,t) = \frac{1}{D}\frac{\partial T(x,y,t)}{\partial t} \ . \qquad (1.8)$$

For the solution of the two-dimensional heat equation in the presence of a periodic square pulse with the frequency ω, we write the temperature profile as a series of solutions $\theta(x,y,t)$ with different eigenvalues a. To solve the temperature profile we use the technique of separation of variables[7] in along the x and y-direction. We then impose certain boundary conditions related to the problem in hand. The first boundary condition that we use throughout this thesis comes from conservation of energy which we assume the total heat flux is continuous[3] throughout the system under study. We write it as:

$$k_q \frac{\partial T_q}{\partial n} = k_p \frac{\partial T_p}{\partial n} \ , \qquad (1.9)$$

where the subscripts p and q indicate the two different materials that are in contact with each other. The derivative n is the direction of heat flow between the two materials.

The second boundary condition which we will use in subsequent chapters expresses the continuity of temperature. We assume that the interfacial thermal resistivity[32, 33] between different layers of a single material and also throughout the system composed of different materials is negligible and we have a continuity in temperature which we write as:

$$T_q(x=x_0,y) = T_p(x=x_0,y) \ , \qquad (1.10)$$

where the temperature at the surface of contact $x=x_0$ is equal between two different materials.

By solving Fourier's heat equation in the foretold manner Eq. (1.2) we can calculate the thermal properties of the system such as the thermal conductivity via various methods, some which we have used in the following chapters.

1.2.2 Microscopic origin of thermal conductivity

The transport of thermal properties between different materials is intimately connected to the presence of interfaces, through electron-phonon interaction[8] and phonon-phonon interaction[9-11]. In the context of heat transfer, the effect of increased thermal resistance due to an interface was discovered by Kapitza in 1941[12,13] in the liquid helium-metal system and later on was demonstrated to be ever-present in any type of interfaces[14]. In nonmetallic solids, thermal energy is predominantly carried by lattice vibrations or phonons while in metals it is carried by electrons. If we have a material which has a perfect infinite lattice without any defects[9], phonons

would propagate without scattering resulting in an infinite thermal conductivity. The interaction of lattice waves with each other which is referred to as the phonon-phonon scattering in materials with an anharmonic lattice results in a decrease in the thermal conductivity of such materials. However, in an elastic 4continuum, thermal resistance does not only arise from the lattice being anharmonic but it is the discrete nature of the crystal lattice itself that makes anharmonic thermal resistance possible[15].

An important concept in explaining how anharmonic phonon interactions in the crystal lattice lead to finite thermal conductivity is that of normal vs umklapp phonon-phonon scattering. Umklapp processes (U-processes) are scattering processes among elementary excitations in crystals where momentum conservation is fulfilled with a contribution from the lattice[4].The normal process conserves the phonon momentum and doesn't contribute to the thermal resistance while in the umklapp processes, the wave vector conservation involves a reciprocal lattice vector which changes the momentum and thereby causes thermal resistance[16-22]. We should pay attention that although this definition might seem appealing the distinction between normal and umklapp processes is to some extent artificial and depends on our convention in choosing the basic cell of the reciprocal lattice[4, 23, 24].

An example of the umklapp process would be in isolated single-walled carbon nanotube's where the thermal conductivity increases with the increase of temperature at low temperature, which shows a peak behavior at about 85 K before falling off at higher temperature[25]. Umklapp processes also play a role in noncrystalline structures without any periodic order such as a monatomic liquid in which inelastic excitations can be interpreted as the noncrystalline counterpart of Umklapp peaks[26].

We solve the thermal conductivity introduced through Fourier's heat equation Eq. (1.1) and apply electron-phonon scattering along with the umklapp process to explain the local decrease in thermal conductivity in certain regions of the composite samples under study.

1.3.1 Limits of state-of-the-art methods for measuring the thermal properties of thin films

In recent years, the so-called 3ω method Figure 1.1 has emerged as the technique of choice for measuring the thermal conductivity in thin films due to its reliability and simplicity of implementation[27]. In the 3ω method, a thin metallic resistor deposited on the thin film specimen

to be measured acts at the same time as a heat source and a thermistor. An AC current at frequency ω is applied to this resistor, which causes the power delivered by the metal to the sample to oscillate periodically at double frequency, 2ω. Since the intensity of the thermal power absorbed by the thin film specimen from the metallic resistor depends on the specimen's thermal conductivity as well as the periodic fluctuations in the thermal resistivity of the metal, the AC voltage at the two ends of the metallic resistor presents a modulation at 3ω frequency, which is also proportional, in its intensity, to the thermal conductivity of the sample. Nevertheless, if the interfacial (Kapitza-type) thermal resistivity from the heating resistor to the sample is comparable to the sample's thermal resistance, the intrinsic thermal conductivity of the thin film measured by the 3ω method will be grossly underestimated[27]. This issue causes major problems for thermal measurements in thin film materials with extremely high thermal conductivities in contact based techniques including the 3ω method. Contactless methods for measuring the thermal conductivity are in extremely high demand when measurements in highly thermally conducting thin films are needed. In addition, the contribution of the substrate in evacuating heat is very difficult to take into account when using the 3ω method.
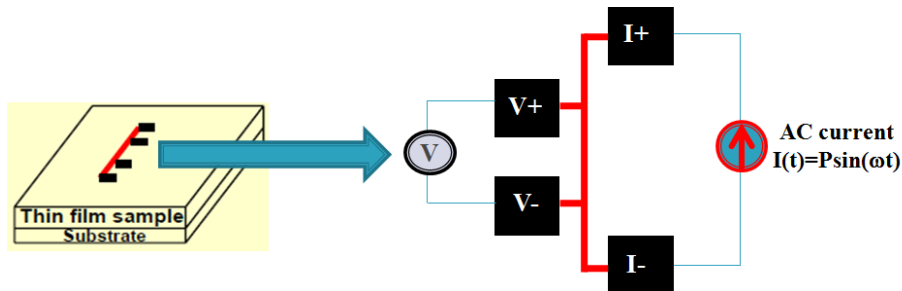
Figure 1.1: The 3ω method is based on the radial heat flow. An AC current at frequency ω is applied to this resistor, which causes the power delivered by the metal to the sample to oscillate periodically at double frequency, 2ω.

1.3.2 Limits of state-of-the-art methods for thermal imaging

Despite great demands, experimental techniques capable of imaging thermal conductivity at the high lateral resolution demanded by state-of-the-art electronic components, pose a tremendous challenge to both academia and industry. Most of the methods used to determine the thermal conductivity of thin solid films, including the 3 ω method, laser flash techniques[28] and others[29,]

[30], are macroscopic in nature and average the thermal properties over large areas. They are unable to recognize the local fluctuations in sample composition and in the local variations of the thermal properties at the nanoscale.

To date, nanoscale thermal measurements mostly rely on scanning thermal microscopy (SThM), a family of contact-mode scanning probe microscopy techniques that utilize thermal sensors integrated with cantilever probes. In SThM architectures that have been proposed to date, both the cantilever acts as the thermal sensor and simultaneously as a heat generator, or the heat generated by electrical current flowing through the scanning probe cantilever and the sample is detected by local thermometers based on infrared spectroscopy, thermoelectric effects or a combination of these methods. Unfortunately, in all these cases, relatively voluminous scanning probe cantilevers are required to be in contact with the sample. The measuring probe acts as an important thermal sink and the strong coupling between the probe and the sample cannot be neglected. Significant interfacial thermal resistivity also affects SThM measurements.

Thermal sinks and interfacial thermal resistivity effects associated to SThM probes are largely irreproducible due to the irreproducibility of the distance and the thermal contact between the probe and the sample, an issue that is particularly problematic in samples with nanoscale roughness. SThM measurements in which the cantilever is immersed in a fluid have been attempted with the objective of improving the thermal contacts. However, fundamental studies have shown that a solid-liquid interface also constitutes a large thermal barrier. Subsequently, liquid-immersion SThM is unlikely to mitigate many of the thermal sink issues commonly associated with SThM techniques. Different approaches are required to overcome the constraints of SThM[31].

1.3.3 Methods for calculating the thermal properties of graphene-based materials and the limitation of the electron-phonon interaction method

Controlling the thermal properties of graphene thin films by assembling metallic structures on their surface is a promising direction with significant applications in industry and electronic devices. Explanations such as interfacial thermal resistivity between the metals and graphene thin films [34-36], phonon-phonon scattering caused by metals creating defects on the surface of the graphene flake[37, 38], disorder-assisted electron-phonon scattering[39] and charge impurity scattering on the surface of the graphene flake [40-44] have been given for the thermal property

variations of graphene composites. However, the role of electron-phonon scattering in affecting the thermal properties of graphene composites has never been investigated in detail.

It has been shown that by applying metals on the surface of graphene its electronic band structure alters[45]. For example, when metals such as (Cu, Al, Ag, Au, and Pt) are applied on the surface of graphene they cause a shift in the graphene Fermi energy. To this end, the use of specific metals, such as copper [46-48], has been explored for graphene-based devices. Using classical calculations, Ziman et al.[49] showed that the thermal conductivity of a material can decrease due to electron-phonon scattering. Although Zimans three particle process with an electron and phonon on one side and an electron on the other side is true in many cases it is unlikely to happen in graphene-based materials. This due to the fact that the electron-phonon interaction for the three particle process is not resonant and zone boundary electrons couple weakly with acoustic phonons that are mostly zone centered. To this end higher order electron-phonon interactions are required.

1.4 Conclusion and thesis overview

Understanding heat evacuation in thin films and low dimensional systems is vital to design heat spreaders for efficient thermal management. The microstructure of thin films and coatings produced by chemical and physical deposition processes is heterogeneous by nature and their thermal conductivity may experience strong local fluctuations at the nanoscale due to the nonhomogeneous morphology of these coatings and the presence of interfaces, therefore making thermal conductivity measurements on thin films very challenging. The thesis is divided into three major sections, studying the thermal properties at the macroscopic, mesoscopic and microscopic level. In chapter 2 of the thesis, we study the thermal properties of a system at the macroscopic level. We use a new method for calculating the thermal properties of the thin film-substrate system which is photothermal deflection spectroscopy (PDS). In chapter 3, 4 and 5 of the thesis, we study the thermal properties of a material at the mesoscopic level. We introduce a new method for acquiring thermal imaging at the nanoscale which is near-field scanning thermoreflectance imaging (NeSTRI) which we use to image the thermal conductivity and heat capacity of a graphene flake. In chapter 5 we also image the thermal conductivity of a graphene flake with copper particles embedded on its surface through applying the perturbation method. Then we investigate the role of electron-phonon interaction on the thermal conductivity of

graphene thin films. In chapter 6, we study the thermal properties of the graphene flake with embedded copper particles on its surface at the microscopic level. We write the second quantization Hamiltonian for electron-phonon interactions and by using Feynman diagrams we compare the thermal conductivity of the graphene flake before and after copper particles are embedded on its surface. Finally, in chapter 7, we summarize our study and suggest future research directions for our work.

1.5 References

[1]   Alexander A. Balandin, *Thermal properties of graphene and nanostructured carbon materials*, Nature Materials, 08/2011, Volume 10, Issue 8

[2]   A. A. Balandin, *Better computing through CPU cooling*, *IEEE Spectrum* 29–33 (October 2009)

[3]   H. S. Carslaw and J. C. Jaeger, *Conduction of Heat in Solids (2nd ed.)*, Oxford University Press, London 1959

[4]   N. W. Ashcroft and D. N. Mermin, *Solid State Physics*, Saunders College, Philadelphia, 1976

[5]   P. G. Klemens, *Theory of the A-plane thermal conductivity of graphite*, J. Wide Bandgap Mater. 7 332–339, 2000

[6]   S. J. Blundell and K. M. Blundell, *Concepts in Thermal Physics* (OUP), 1st ed

[7]   M. L. Boas *Mathematical Methods in the Physical Science* (John Wiley & Sons), 3rd ed

[8]   G. D. Whitfield, Phys. Rev., Phys. Rev. 121, 720, Feb. 1961

[9]   J. Callaway, Journal of Mathematical Physics, June 1964, Volume 5, Number 6

[10]   Miles V. Klein, Phys. Rev, Volume 141, Number 2, Jan 1966

[11]   R. F. Caldwell, Miles V. Klein, Phys. Rev, Volume158, Number3, June 1967

[12]   P. L. Kapitza, Zh. Eksp. *Teor. Fiz.* 11, 1 (1941) (J. Phys. (USSR)4, 181, 1941); also in Collected Papers of P. L. Kapitza, Vol. 2, D. ter Haar, ed. (Pergamon, Oxford, 1965), p. 581

[13]   Z. Wei, Z. Ni, K. Bi, M. Chen, Y. Chen, Phys. Lett. A, Volume 375, Issue 8, Pages 1195-1199, Feb 2011

[14]   E.T. Swartz, R.O. Pohl, Rev. Mod. Phys.61, 605 of Modern Physics, July 1989

[15] R. Peierls, *Zur kinetischen Theorie der W€armeleitung in Kristallen*, Ann. Phys. 395, 1055–1101 (1929)

[16] C. Kittel, *Introduction to Solid State Physics* (Wiley, Hoboken, 2005)

[17] J. S. Blakemore, *Solid State Physics* (Cambridge U.P., Cambridge, 1985).

[18] G. P. Srivastava, *Elements of Solid State Physics* (Prentice-Hall, Englewood Cliffs, NJ, 2006)

[19] G. Chen, *Nanoscale Energy Transport and Conversion* (Oxford U.P., Oxford, 2005)

[20] Z. M. Zhang, *Nano/Microscale Heat Transfer* (McGraw-Hill, NewYork, 2007)

[21] L. F. Lou, *Introduction to Phonons and Electrons* (World Scientific, Singapore, 2003).

[22] D. B. Sirdeshmukh and L. Sirdeshmukh, *Atomistic Properties of Solids*, (Springer, Berlin, 2011)

[23] H. E. Hall, *Solid State Physics* (Wiley, London, 1974)

[24] P. L. Taylor and O. Heinonen, *A Quantum Approach to Condensed Matter Physics* (Cambridge U.P., Cambridge, 2002)

[25] J. X. Cao, X. H. Yan, Y. Xiao and J. W. Ding, Phys. Rev. B, 69, 073407, 2004

[26] T. Scopigno, M. D'astuto, M. Krisch, F. Sette, and G. Ruocco, Phys. Rev. B, Volume 64, Issue 1, 2001

[27] H. Wang, M. Sen, *Analysis of the 3-omega method for thermal conductivity measurement*, International Journal of Heat and Mass Transfer, March 2009

[28] W. J. Parker, R. J. Jenkins, and G. L. Abbot, J. Appl. Phys., 1964, 32, 1679

[29] W. B. Jackson, N. M. Amer, and D. Fournier, Appl. Optics, 1981, 20, 1333

[30] S. Ezugwu, M. S. Ahmed, R. Divigalpitiya, and G. Fanchini, Thin Solid Films, 2013, 534, 520-528.

[31] S. Ezugwu, S. Kazemian, D. W. Choi, and G. Fanchini, Nanoscale 2017, 9, 4097-4106

[32] Barrat, Jean-Louis, Chiaruttini, Molecular Physics, 2003, Volume 101, Issue 11

[33] Deng, Chernatynskiy, J. Appl. Phys., 2014, Volume 115, Issue 8

[34] L. Hu, T. Desai, P. Keblinski, Phys. Rev. B 83, 195423, 10 May 2011

[35] Q. X. Pei, Y. W. Zhang, Z. D. Sha, V. B. Shenoy, Appl. Phys. Lett. 100, 101901, 2012

[36] B. S. Lee, J. S. Lee, Appl. Phys. A, Volume 121, Issue 3, pp 1193–1202, Nov 2015

[37] D. Liu, P. Yang, X. Yuan, J. Guo, N. Liao, Phys. Lett. A, Volume 379, Issue 9, Pages 810-814, Apr 2015

[38]   B. S. Lee, J. S. Lee, Appl. Phys. A, Volume 121, Issue 3, pp 1193–1202, Nov 2015

[39]   J. C. W. Song, M. Y. Reizer, and L. S. Levitov, Phys. Rev. Lett. 109, 106602, 2012

[40]   J. H. Chen, C. Jang, S. Adam, M. S. Fuhrer, E. D. Williams, M. Ishigami, Nat. Phys 4, 377 – 381, Apr 2008

[41]   D. S. Novikov, Applied Physics Letter, Appl. Phys. Lett. 91, 102102, Aug 2007

[42]   M. Trushin, J. Schliemann, Phys. Rev. Lett. 99, 216602, 21 Nov 2007

[43]   X. Z. Yan, Y. Romiah, C. S. Ting, Phys. Rev. B 77, 125409, 13 Mar 2008

[44]   G. Giovannetti, P.A. Khomyakov, G. Brocks, V.M. Karpan, J. Van den Brink, P.J. Kelly, Phys. Rev. Let., 101 (2008), pp. 026803-026804

[45]   S. Xiao, J.H. Chen, S. Adam, E.D. Williams, and M.S. Fuhrer, Phys. Rev. B 82, 041406, July 2010

[46]   F. Sola, J. Niu, Z.H. Xia, J. Phys. D Appl. Phys., 46 (2013), pp. 065309-065316

[47]   N.A. Luechinger, E.K. Athanassiou, W.J. Stark, Nanotechnology, 19 (2008), p. 445201

[48]   A. Akbari-Sharbaf, S. Ezugwu, M.S. Ahmed, M.G. Cottam, and G. Fanchini, Carbon, 95 (2015) 199-207

[49]   J. M. Ziman, The *effect of free electron on lattice conduction*, Philosophical Magazine, Volume 1, Issue 2, 1956

"Heat, like gravity, penetrates every substance of the universe, its rays occupy all parts of space. The object of our work is to set forth the mathematical laws which this element obeys. The theory of heat will hereafter form one of the most important branches of general physics."

Joseph Fourier

Chapter 2

Thermal conductivity measurements by Photothermal Deflection Spectroscopy

2.1 Introduction

Photothermal Deflection Spectroscopy (PDS) has been frequently used to measure the thermal diffusivity of thin films on their substrates. However, in the most commonly used models to interpret PDS data, the substrate is assumed to be highly thermally insulating, which poses restrictions on the reliability of thermal diffusivity measurements by PDS and limits the possibility to use this technique for also measuring the thermal capacity of the samples. Simultaneous knowledge of thermal capacity and thermal diffusivity is necessary to determine the thermal conductivity of thin film materials, which is critical, both fundamentally and technologically. In this chapter, we calculate the deflection angle of the PDS signals both on the front and back side of a thin-film substrate system with different properties. We also calculate the phase and amplitude of the PDS signal at the two opposites sides of a thin-film substrate system. We find that, on both faces, the phases of the PDS signal depend on the thermal diffusivity of the thin film, while the amplitudes depend on its thermal capacity. By using the phase difference and amplitude difference at the two faces, we show that the accuracy of thermal measurements by PDS is significantly improved. We validate our analytical method by comparing it with experiments done on thin gold films attached to glass substrate being illuminated at different frequencies.

2.2 Photothermal deflection spectroscopy

Photoexcitation spectroscopies are a group of high sensitivity spectroscopy techniques capable of simultaneously measuring the optical absorption coefficient and several thermal characteristics of a sample. Examples of photoexcitation spectroscopies are photoacoustic spectroscopy[1] and photothermal bending spectroscopy[2]. Measurements performed by these techniques rely on the change in of the thermal state of an ambient/thin film/substrate system, which results from deliberate absorption of light directly inside the film. Consequently, they can be relatively free from artefacts associated with interfacial thermal resistivity[10-13] effects and the contributions from the non-zero thermal conductivity of the substrate may also be taken into account. The temperature profiles in the thin film specimen and the adjacent media are governed by the Fourier equation of heat for isotropic media[3],

$$\frac{\partial^2 T_q(x,y,t)}{\partial x^2} + \frac{\partial^2 T_q(x,y,t)}{\partial y^2} = \frac{1}{D_q}\frac{\partial T_q(x,y,t)}{\partial t} , \qquad (2.1)$$

where T_q is the temperature in the sample and the adjacent media (substrate and air, or another fluid) and D_q are their thermal diffusivities. After heat is being generated in the sample, it will transmit to the surrounding medium, also modifying their thermal state. PDS is a specific photoexcitation spectroscopy in which a thin film is periodically heated from illumination by a strong pulsed light beam at frequency ω (also known as the "pump" beam) and the consequent, periodic, thermal gradient at the thin film/ambient interface is detected from the periodic changes in refractive index of the ambient materials resulting from its delayed periodical heating and its subsequent changes in density. As a consequence of these changes in refractive index, a weak ("probe") laser beam traveling in the proximity of the substrate will be deflected at an angle ϕ Figure 2.1, according to the following equation, which is a consequence of Fermat's principle for ray optics[4].

$$\phi = \frac{1}{n}\frac{\partial n}{\partial T_f} \int_{-\infty}^{+\infty} \frac{\partial T_f}{\partial x}\bigg|_s dy \qquad (2.2),$$

where the subscript s indicates that the integral has to be performed exactly at the sample/ambient interface, x is the direction normal to the sample/ambient interface and y is the direction along with the "probe" beam is traveling prior to crossing the heated region. It is worth noting that, in general, x and y are *not* necessarily orthogonal. Since the delay in the thermal

gradient to appear at the ambient/sample interface depends on the thermal diffusivity of the sample, D_s can be measured from the phase lag between the illuminating "pump" beam and the "probe" beam signal if Eq. (2.1) is solved for the appropriate geometry and with the suitable periodic and boundary conditions[5]. Consequently, PDS can be used to calculate the thermal conductivity of the thin film specimen as:

$$k_{th,s} = D_s \cdot C_s . \qquad (2.3)$$
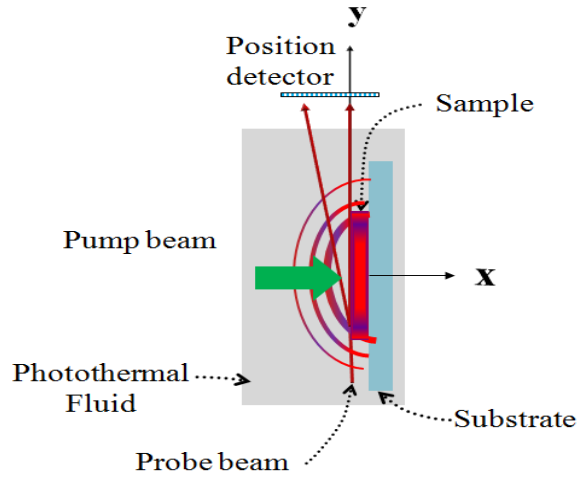
Figure 2.1: The system gets heated up by a pulsed pump beam with a certain frequency. The consequent, periodic, thermal gradient at the thin film/ambient interface is detected from the periodic changes in refractive index of the ambient materials resulting from its delayed periodical heating and its subsequent changes in density. As a consequence of these changes in refractive index, a weak ("probe") laser beam traveling in the proximity of the substrate will be deflected.

In order for the probe beam to have a bigger deflection, we use a photothermal fluid. Photothermal fluids are liquids that experience strong changes in refractive index n from relatively small changes in fluid temperature, T_f. Since air has relatively poor photothermal properties (with Thermo-optical coefficient $(dn/dT_f)/n \sim 10^{-9}$ K^{-1}) samples for PDS experiments are normally immersed in special fluids, including carbon tetrachloride $(dn/dT_f)/n \sim 10^{-3}$ K^{-1}) or Fluorinert[TM] $(dn/dT_f)/n \sim 10^{-4}$ K^{-1}to increase the amplitude of the photothermal signal, which also depends on the thermal capacity C_s of the specimen[4, 6]. PDS has been used by our group to determine the thermal conductivity of several types of materials, including amorphous silicon[4],

graphene thin films[7], and graphene-polymer nanocomposites[8].

2.3 Analytical model for thin film-substrate system

2.3.1 Measuring the temperature profile for the thin film-substrate

In PDS an absorbing sample is heated by a pulsed light beam and the effects of such heating on the optical properties of a nonabsorbing medium surrounding the samples are probed by a second, continuous light beam. Measurements performed by these techniques rely on the change of the thermal state of an ambient/thin film/substrate system, which results from deliberate absorption of light directly inside the film.

Consequently, they can be relatively free from artefacts associated with interfacial thermal resistivity effects and the contributions from the non-zero thermal conductivity of the substrate may also be taken into account.

We assume that the interfacial thermal resistivity is zero between the thin film, substrate and the fluid and therefore the temperature is continuous. By using the method of separation of variables alongside with assumption that temperature is continuous throughout the system, we have four temperature profiles. The temperature profiles would be the temperature profile of the thin film, the temperature profile of the substrate and temperature profiles of the photothermal fluid on the front and back side of the system.

The subscripts s, f and b will refer to the thermal diffusivity (D) and conductivity (k) of the thin film specimen, fluid, and substrate (background), respectively and i will be the imaginary unit. Also, q_0 is the amount of heat absorbed by the sample and ω is the frequency that our laser beam is illuminating the sample.

In this section, we assume that the thin film has a much higher thermal conductivity than the substrate and it absorbs all the heat illuminated by the pump beam. The temperature profile for the thin film is:

$$T_s(y,t) = \frac{q_0}{2k_{th,s}} \sqrt{\frac{D_s}{\omega}} e^{-i\pi/4} e^{-(1+i)\sqrt{\frac{\omega}{2D_s}}|y|} e^{i\omega t}, \qquad (2.4)$$

where we have taken the thin film to be two dimensional with no thickness and therefore Eq. (2.4) has no x components. Also, we assume that the thin film is being illuminated at a pinpoint

14

in the center and therefore the temperature decays exponentially as we move along the positive and negative directions on the *y*-axis.

The temperature profile for the fluid on the front side of our PDS system is:

$$T_{f,front}(x,y,t) = \frac{q_0}{2k_{th,s}}\sqrt{\frac{D_s}{\omega}}e^{-i\pi/4}e^{-(1+i)\sqrt{\frac{\omega}{2D_s}}|y|}e^{(1+i)(\frac{\omega}{2D_f}-\frac{\omega}{2D_s})^{\frac{1}{2}}x}e^{i\omega t},$$ (2.5)

where we move from minus infinity to zero along the *x*-axis. We assume that the fluid doesn't absorb any heat from the pump beam passing through it and only absorbs heat from the thin film. The temperature profile decays exponentially along the *y*-axis as we move away from the center and it also decays exponentially along the *x*-axis as we move away from the thin film.

The temperature profile for the substrate is:

$$T_b(x,y,t) = \frac{q_0}{4k_{th,s}}\sqrt{\frac{D_s}{\omega}}e^{-i\pi/4}e^{-(1+i)\sqrt{\frac{\omega}{2D_s}}|y|}e^{i\omega t}.$$

$$\left[\left(e^{(\frac{i\omega}{D_b}-\frac{i\omega}{D_s})^{\frac{1}{2}}x}+e^{-(\frac{i\omega}{D_b}-\frac{i\omega}{D_s})^{\frac{1}{2}}x}\right)+\frac{k_f}{k_b}\left(\frac{D_b.(D_s-D_f)}{D_f.(D_s-D_b)}\right)^{1/2}.\left(e^{-(\frac{i\omega}{D_b}-\frac{i\omega}{D_s})^{\frac{1}{2}}x}-e^{(\frac{i\omega}{D_b}-\frac{i\omega}{D_s})^{\frac{1}{2}}x}\right)\right],$$ (2.6)

where we move from zero to the substrate's thickness L_x along the *x*-axis. Also, the temperature drops exponentially along the *y*-axis as we move away from the center of illumination.

The temperature profile for the fluid on the right side of the system is:

$$T_{f,back}(x,y,t) = \frac{q_0}{4k_{th,s}}\sqrt{\frac{D_s}{\omega}}e^{-i\pi/4}e^{-(1+i)\sqrt{\frac{\omega}{2D_s}}|y|}e^{-(\frac{i\omega}{D_f}-\frac{i\omega}{D_s})^{\frac{1}{2}}x}e^{i\omega t}.$$

$$e^{(\frac{i\omega}{D_f}-\frac{i\omega}{D_s})^{\frac{1}{2}}L_x}.\left[\left(e^{(\frac{i\omega}{D_b}-\frac{i\omega}{D_s})^{\frac{1}{2}}L_x}+e^{-(\frac{i\omega}{D_b}-\frac{i\omega}{D_s})^{\frac{1}{2}}L_x}\right)+\frac{k_f}{k_b}\left(\frac{D_b.(D_s-D_f)}{D_f.(D_s-D_b)}\right)^{1/2}.\left(e^{-(\frac{i\omega}{D_b}-\frac{i\omega}{D_s})^{\frac{1}{2}}L_x}-e^{(\frac{i\omega}{D_b}-\frac{i\omega}{D_s})^{\frac{1}{2}}L_x}\right)\right].$$

(2.7)

where we move from L_x to positive infinity along the *x*-axis. The temperature along the *y*-axis again drops exponentially as we move away from the center. From the following equations, it can easily be seen that temperature profile is continuous along the fluid, thin film and substrate. Having the temperature profile of the fluid on the front and back side of the system we can calculate the deflection angle of the PDS beam.

2.3.2 Calculating the deflection angle of the probe beam along the y-axis

The configuration sketched in Figure 2.2 shows the PDS system being illuminated at the center by a pump beam and a probe beam directed in the *y*-direction is being deflected.
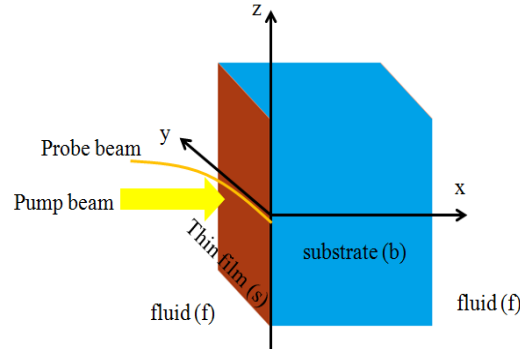
Figure 2.2: The thin film-substrate being illuminated at the center by a pump beam and the probe beam being emitted along the *y*-axis.

Figure 2.3 shows the sample is illuminated by a thin beam (a) and a thick beam (b). In order to get the deflection angle on the front and back side of the system, we first assume that the width of the pump beam is extremely thin which means that we are only heating a point at the center of the sample which can be approximated to be delta-shaped. This argument is based on the fact that the width of the pump beam is much smaller than the thermal diffusion length in the thin film. Then for analyzing problems more similar to the experimental setup, we study the deflection angle for when the pump beam is thick and is illuminating a certain area on the surface of the sample. In this case, we write the width of the beam as a series of delta functions and add them all up.
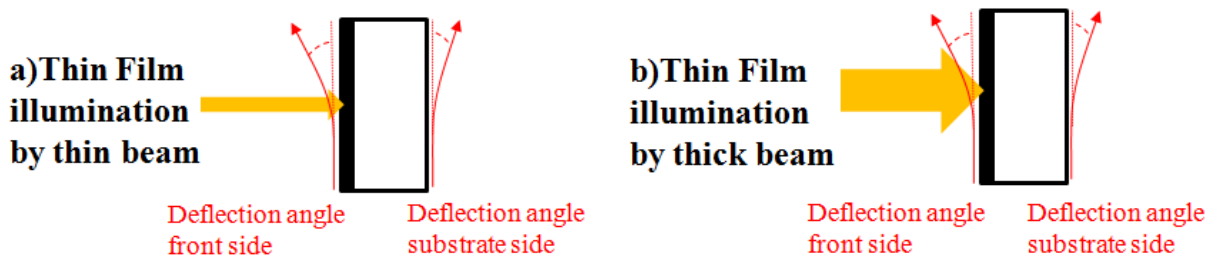
Figure 2.3: a) The thin film is illuminated by a thin beam that can be approximated as a Dirac delta distribution. b) The thin film is illuminated by a thick beam with a certain width that can be written as the accumulation of thin beams.

The results of the deflection angle for the front and back side of the PDS system for when the probe beam is being emitted along the *y*-direction for the thin beam configuration is:

$$\phi_{front} = \frac{q_0 D_s}{(2\omega)^{\frac{1}{2}} k_{th,s}} \frac{1}{n_f} \frac{\partial n_f}{\partial T_f} (\frac{1}{D_f} - \frac{1}{D_s})^{\frac{1}{2}} e^{-i\pi/4} e^{i\omega t} , \tag{2.8}$$

$$\phi_{back} = \frac{q_0}{k_{th,s} n_f} \frac{D_s}{(2\omega)^{\frac{1}{2}}} \frac{\partial n_f}{\partial T_f} e^{-(1+i)(\frac{\omega}{2D_f} - \frac{\omega}{2D_s})^{\frac{1}{2}} L_x} \left[(\frac{1}{D_f} - \frac{1}{D_s})^{\frac{1}{2}} - (\frac{1}{D_b} - \frac{1}{D_s})^{\frac{1}{2}} (\frac{k_{th,b}}{k_{th,f}} e^{(1+i)(\frac{2\omega}{D_b} - \frac{2\omega}{D_s})^{\frac{1}{2}} L_x} - 1) \right] e^{-i\pi/4} e^{i\omega t} ,$$

$$\tag{2.9}$$

where Eq. (2.8) is the deflection angle on the front side of the PDS system and Eq. (2.9) is the deflection angle on its backside.

Due to the linear characteristic of Eq. (2.1), the temperature profile obtained in this way, $G_q(x, y - y_0)$, represents the Green function[9, 14] that, by summing an infinite array of delta-shaped sources at $y = [-L_y/2; + L_y/2]$ offers the actual temperature profile in the fluid/thin film/substrate system:

$$T_q(x, y, \omega) = \int_{-L_y/2}^{+L_y/2} G_q(x, y - y_0) \cdot dy . \tag{2.10}$$

Having the temperature profiles for the fluid on the front and back side of our system from Eq. (2.5) and Eq. (2.7) and implementing them into Eq. (2.9) we get the new temperature profile for the thick pump beam Figure 2.3(b).

For measuring the amount of heat being absorbed by the thin film for the thick beam configuration we write q_0 as:

$$q_0 = \frac{P_0}{L_y \cdot L_z} \cdot \eta \cdot \exp(-\eta x) , \tag{2.11}$$

where P_0 is the power of the laser beam, η is the optical absorption coefficient of the thin film, and $L_y \times L_z$ is the area illuminated by the thick beam. Computing the average amount of the heat absorbed by the sample we get:

$$\bar{q}_0 = \frac{P_0}{L_y L_z} \cdot \eta \cdot \langle \exp(-\eta x) \rangle = \frac{P_0(1 - \exp(-\eta d))}{d \cdot L_y \cdot L_z} , \tag{2.12}$$

17

where d is the thickness of the sample. Implementing the new temperature profile for the thick beam into Eq. (2.11) we get the new deflection angle on the front and back side of the PDS system which is:

$$\phi_{front} = \frac{1}{n_f} \cdot \frac{\partial n_f}{\partial T_f} \cdot \frac{P_0(1-\exp(-\eta d))}{k_{th,s} \cdot d \cdot L_y \cdot L_z} \cdot \frac{D_s}{\omega^{1/2}} \left(\frac{D_s - D_f}{D_s D_f} \right)^{1/2} \exp(-i\pi/4), \tag{2.13}$$

$$\phi_{back} = -\frac{1}{n_f} \cdot \frac{\partial n_f}{\partial T_f} \cdot \frac{P_0(1-\exp(-\eta d))}{2k_{th,s} \cdot d \cdot L_y \cdot L_z} \cdot \frac{D_s}{\omega^{1/2}} \cdot \left(\frac{D_s - D_f}{D_s D_f} \right)^{1/2} \cdot \exp\left[-\left(\frac{\omega}{2D_f} - \frac{\omega}{2D_s} \right)^{1/2} L_x \right] \times$$

$$\left[(1-\alpha + \cos\beta\exp(\beta) + \alpha \cdot \cos\beta\exp(\beta))^2 + (\sin\beta\exp(\beta) + \alpha \cdot \sin\beta\exp(\beta))^2 \right]^{1/2} \times \tag{2.14}$$

$$\exp\left\{ i \left[\arctan\left(\frac{\sin\beta\exp(\beta) + \alpha\sin\beta\exp(\beta)}{1-\alpha + \cos\beta\exp(\beta) + \alpha\cos\beta\exp(\beta)} \right) - \left(\frac{\omega}{2D_f} - \frac{\omega}{2D_s} \right)^{1/2} L_x - \pi/4 \right] \right\}$$

where L_x, L_y, and L_z are, respectively, the thickness, length, and width of the PDS system. Also for simplifying our equations, we define two new variables α and β which are defined as:

$$\alpha = \frac{k_{th,f}}{k_{th,b}} \cdot \left(\frac{D_b(D_s - D_f)}{D_f(D_s - D_b)} \right)^{1/2}, \beta = \left(\frac{2\omega}{D_b} - \frac{2\omega}{D_s} \right)^{1/2} L_x \tag{2.15}$$

We will extract the amplitude and the phase shift from the deflection angle. The amplitude on the front and back side of the system is equal to the real terms in Eq. (2.12) and (2.13). The phase shift is equal to the imaginary components of the exponential.

$$Amp(\phi_{front}) = \frac{1}{n_f} \cdot \frac{\partial n_f}{\partial T_f} \cdot \frac{P_0(1-\exp(-\eta d))}{k_{th,s} \cdot d \cdot L_y \cdot L_z} \cdot \frac{D_s}{\omega^{1/2}} \left(\frac{D_s - D_f}{D_s D_f} \right)^{1/2}, \tag{2.16}$$

$$Ph(\phi_{front}) = -\frac{\pi}{4}, \tag{2.17}$$

$$Amp(\phi_{back}) = -\frac{1}{n_f} \cdot \frac{\partial n_f}{\partial T_f} \cdot \frac{P_0(1-\exp(-\eta d))}{k_{th,s} \cdot d \cdot L_y \cdot L_z} \cdot \frac{D_s}{\omega^{1/2}} \left(\frac{D_s - D_f}{D_s D_f} \right)^{1/2} \cdot \exp\left[-\left(\frac{\omega}{2D_f} - \frac{\omega}{2D_s} \right)^{1/2} L_x \right] \times \tag{2.18}$$

$$\left[(1-\alpha + \cos\beta\exp(\beta) + \alpha\cos\beta\exp(\beta))^2 + (\sin\beta\exp(\beta) + \alpha\sin\beta\exp(\beta))^2 \right]^{1/2}$$

$$Ph(\phi_{back}) = \arctan\left(\frac{\sin\beta\exp(\beta) + \alpha\sin\beta\exp(\beta)}{1-\alpha + \cos\beta\exp(\beta) + \alpha\cos\beta\exp(\beta)} \right) - \left(\frac{\omega}{2D_f} - \frac{\omega}{2D_s} \right)^{1/2} L_x - \pi/4. \tag{2.19}$$

Finding the phase shift and amplitude along the *y*-axis does not give us a complete set of equations to calculate the thermal conductivity since the temperature was solved in the two dimensions *x* and *y* and taking an integral over *y* Eq. (2.10) diminishes one of the variables. As can be seen from Eq. (2.22) the phase shift for the front of our PDS system is constant for all thin films and substrates and this won't be useful in developing new models with different thin film coatings and substrates. To solve this problem we emit the probe beam of the PDS system along the *z*-direction.

2.3.3 Measuring the deflection angle of the probe beam along the *z*-axis

The major difference of this section with the previous one is that in the new configuration Figure (2.4), the probe beam is emitted along the *z*-axis rather than the *y*-axis. Hence, in Eq. (2.2) we integrate the path covered by the probe beam over the *z*-axis instead of the *y*-axis. Due to the different measurement configuration used in this model, deflection of light occurs both longitudinally to the probe-beam axis (along *y*-direction) and transversally (along with the *x*-direction). These two components can be evaluated by replacing the first-derivatives of the temperature profile in Eq. (2.2), along with the out-of-plane (*x*) and in-plane (*y*) directions relative to the sample surface, in which two distinct temperature gradient occur due to sampling heating. These lead to the following expressions for the periodical deflection angle in longitudinal direction:

$$\phi = \frac{1}{n_f} \frac{\partial n_f}{\partial T_f} \int_{-\infty}^{+\infty} \frac{\partial T_f}{\partial y} \bigg|_s dz, \tag{2.20}$$

while the corresponding deflection angle in transversal direction is given by:

$$\phi = \frac{1}{n_f} \frac{\partial n_f}{\partial T_f} \int_{-\infty}^{+\infty} \frac{\partial T_f}{\partial x} \bigg|_s dz. \tag{2.21}$$

The temperature profiles of the system for the fluid, thin film and substrate remain the same as before, equations (2.4), (2.5), (2.6), (2.7).

Since the probe beam will be moving along the surface of the thin film, pointing along the *z*-direction, we would have two profiles for the deflection angle. Figure 2.4(a) is for when the probe beam is not emitted within the surface area illuminated by the pump beam, and Figure 2.4(b) is for when the probe beam is being emitted within the surface area illuminated by the pump beam. Due to the fact that Fourier's heat equation is a second order differential equation,

the amplitude and the deflection angle should remain continuous as we move the probe beam along the *y*-direction.
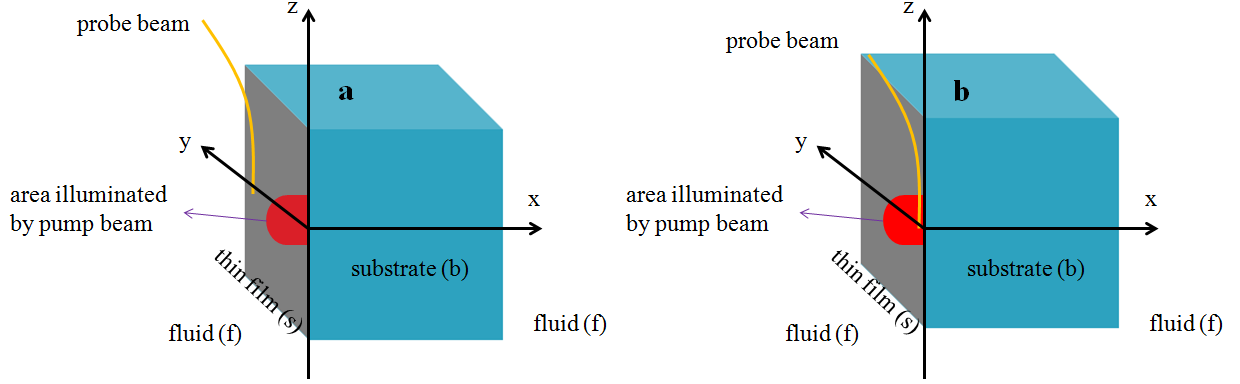
Figure 2.4: a) The emitted probe beam along the z-direction not passing by the surface area illuminated directly by the pump beam. b) The emitted probe beam along the z-direction not passing by the surface area illuminated directly by the pump beam.

To proceed with the calculations we take δ to be the length of the area illuminated by the pump beam along the *y*-axis. For when the probe beam is not emitted within the surface area illuminated by the pump beam *y> δ* and *y<-δ* Figure 2.4(a), the deflection angle on the front side is:

$$
\begin{aligned}
\phi_{front,x} &= \frac{1}{n_f}\cdot\frac{\partial n_f}{\partial T_f}\cdot\frac{P_0\left(1-\exp(-\eta d)\right)}{k_{th,s}\cdot d\cdot L^2{}_y}\cdot\left(\frac{D_s}{\omega}\right)\cdot\left(\frac{\omega}{D_f}-\frac{\omega}{D_s}\right)^{1/2}\times\exp\left(-\left(\frac{\omega}{2D_s}\right)^{1/2}y\right)\\
&\times\left[(\sinh\gamma\cos\gamma)^2+(\sin\gamma\cosh\gamma)^2\right]^{1/2}\exp\left[i\left(arctg(-tg\gamma\cdot ctgh\gamma)-\left(\frac{\omega}{2D_s}\right)^{1/2}y-\frac{\pi}{4}\right)\right],
\end{aligned}
\tag{2.22}
$$

$$
\begin{aligned}
\phi_{front,y} &= \frac{1}{n_f}\cdot\frac{\partial n_f}{\partial T_f}\cdot\frac{P_0\left(1-\exp(-\eta d)\right)}{k_{th,s}\cdot d\cdot L^2{}_y}\cdot\left(\frac{D_s}{\omega}\right)^{1/2}\times\exp\left(-\left(\frac{\omega}{2D_s}\right)^{1/2}y\right)\\
&\times\left[(\sinh\gamma\cos\gamma)^2+(\sin\gamma\cosh\gamma)^2\right]^{1/2}\exp\left[i\left(arctg(-tg\gamma\cdot ctgh\gamma)-\left(\frac{\omega}{2D_s}\right)^{1/2}y+\frac{3\pi}{4}\right)\right].
\end{aligned}
\tag{2.23}
$$

The *x* and *y* subscripts indicate whether the deflection is transversal or longitudinal. Also for simplifying our equations we define γ to be:

$$
\gamma=\left(\frac{\omega}{2D_s}\right)^{1/2}\delta.
\tag{2.24}
$$

Writing the amplitude and the phase shift along the *x*-axis for Eq. (2.27) we have:

$$Amp\left(\phi_{front,x}\right)=\frac{1}{n_f}\cdot\frac{\partial n_f}{\partial T_f}\cdot\frac{P_0\left(1-\exp(-\eta d)\right)}{k_{th,s}\cdot d\cdot L^2{}_y}\cdot\left(\frac{D_s}{\omega}\right)\left(\frac{\omega}{D_f}-\frac{\omega}{D_s}\right)^{1/2}\times\exp\left(-\left(\frac{\omega}{2D_s}\right)^{1/2}y\right),$$

$$\times\left[\left(\sinh\gamma\cos\gamma\right)^2+\left(\sin\gamma\cosh\gamma\right)^2\right]^{1/2} \tag{2.25}$$

$$Ph\left(\phi_{front,x}\right)=arctg\left(-tg\gamma\cdot ctgh\gamma\right)-\left(\frac{\omega}{2D_s}\right)^{1/2}y-\frac{\pi}{4}. \tag{2.26}$$

Writing the amplitude and the phase shift along the *y*-axis for Eq. (2.23) we have:

$$Amp\left(\phi_{front,y}\right)=\frac{1}{n_f}\cdot\frac{\partial n_f}{\partial T_f}\cdot\frac{P_0\left(1-\exp(-\eta d)\right)}{k_{th,s}\cdot d\cdot L^2{}_y}\cdot\left(\frac{D_s}{\omega}\right)^{1/2}\times\exp\left(-\left(\frac{\omega}{2D_s}\right)^{1/2}y\right),$$

$$\times\left[\left(\sinh\gamma\cos\gamma\right)^2+\left(\sin\gamma\cosh\gamma\right)^2\right]^{1/2} \tag{2.27}$$

$$Ph\left(\phi_{front,y}\right)=arctg\left(-tg\gamma\cdot ctgh\gamma\right)-\left(\frac{\omega}{2D_s}\right)^{1/2}y+\frac{3\pi}{4}. \tag{2.28}$$

With the same assumption that the probe beam is emitted along the *z*-axis outside the surface area illuminated by the pump beam, the deflection angle of the back side PDS signal for the corresponding transversal and longitudinal is:

$$\phi_{back,x}=\frac{1}{n_f}\cdot\frac{\partial n_f}{\partial T_f}\cdot\frac{P_0\left(1-\exp(-\eta d)\right)}{2k_{th,s}\cdot d\cdot L^2{}_y}\cdot\left(\frac{D_s}{\omega}\right)\cdot\left(\frac{\omega}{D_f}-\frac{\omega}{D_s}\right)^{1/2}\times\exp\left(-\left(\frac{\omega}{2D_s}\right)^{1/2}y\right)\times\exp\left(-\left(\frac{\omega}{D_f}-\frac{\omega}{D_s}\right)^{1/2}L_x\right)$$

$$\times\left[\left(\sinh\gamma\cos\gamma\right)^2+\left(\sin\gamma\cosh\gamma\right)^2\right]^{1/2}\times\left[\left(1-\alpha+e^\beta\cos\beta+\alpha e^\beta\cos\beta\right)^2+\left(e^\beta\sin\beta+\alpha e^\beta\sin\beta\right)^2\right]^{1/2},$$

$$\times\exp\left[i\left(-\left(\frac{\omega}{D_f}-\frac{\omega}{D_s}\right)^{1/2}L_x+arctg\left(-tg\gamma\cdot ctgh\gamma\right)-\left(\frac{\omega}{2D_s}\right)^{1/2}y+\frac{3\pi}{4}+arctg\left(\frac{e^\beta\sin\beta+\alpha e^\beta\sin\beta}{1-\alpha+e^\beta\cos\beta+\alpha e^\beta\cos\beta}\right)\right)\right]$$

$$\tag{2.29}$$

$$\phi_{back,y}=\frac{1}{n_f}\cdot\frac{\partial n_f}{\partial T_f}\cdot\frac{P_0\left(1-\exp(-\eta d)\right)}{2k_{th,s}\cdot d\cdot L^2{}_y}\cdot\left(\frac{D_s}{\omega}\right)^{1/2}\times\exp\left(-\left(\frac{\omega}{2D_s}\right)^{1/2}y\right)\times\exp\left(-\left(\frac{\omega}{D_f}-\frac{\omega}{D_s}\right)^{1/2}L_x\right)$$

$$\times\left[\left(\sinh\gamma\cos\gamma\right)^2+\left(\sin\gamma\cosh\gamma\right)^2\right]^{1/2}\times\left[\left(1-\alpha+e^\beta\cos\beta+\alpha e^\beta\cos\beta\right)^2+\left(e^\beta\sin\beta+\alpha e^\beta\sin\beta\right)^2\right]^{1/2}$$

$$\times\exp\left[i\left(-\left(\frac{\omega}{D_f}-\frac{\omega}{D_s}\right)^{1/2}L_x+arctg\left(-tg\gamma\cdot ctgh\gamma\right)-\left(\frac{\omega}{2D_s}\right)^{1/2}y+\frac{3\pi}{4}+arctg\left(\frac{e^\beta\sin\beta+\alpha e^\beta\sin\beta}{1-\alpha+e^\beta\cos\beta+\alpha e^\beta\cos\beta}\right)\right)\right]$$

$$.\tag{2.30}$$

Writing the amplitude and the phase shift along the *x*-axis for Eq. (2.29) we have:

$$Amp(\phi_{back,x}) = \frac{1}{n_f} \cdot \frac{\partial n_f}{\partial T_f} \cdot \frac{P_0(1 - \exp(-\eta d))}{2k_{th,s} \cdot d \cdot L^2_y} \cdot \left(\frac{D_s}{\omega}\right) \cdot \left(\frac{\omega}{D_f} - \frac{\omega}{D_s}\right)^{1/2} \times \exp\left(-\left(\frac{\omega}{2D_s}\right)^{1/2} y\right) \times \exp\left(-\left(\frac{\omega}{D_f} - \frac{\omega}{D_s}\right)^{1/2} L_x\right),$$

$$\times \left[(\sinh\gamma\cos\gamma)^2 + (\sin\gamma\cosh\gamma)^2\right]^{1/2} \times \left[(1 - \alpha + e^\beta\cos\beta + \alpha e^\beta\cos\beta)^2 + (e^\beta\sin\beta + \alpha e^\beta\sin\beta)^2\right]^{1/2}$$

$$(2.31)$$

$$Ph(\phi_{back,x}) = -\left(\frac{\omega}{D_f} - \frac{\omega}{D_s}\right)^{1/2} L_x \, arctg(-tg\gamma \cdot ctgh\gamma) - \left(\frac{\omega}{2D_s}\right)^{1/2} y + \frac{3\pi}{4} + arctg\left(\frac{e^\beta\sin\beta + \alpha e^\beta\sin\beta}{1 - \alpha + e^\beta\cos\beta + \alpha e^\beta\cos\beta}\right).$$

$$(2.32)$$

Writing the amplitude and the phase shift along the y-axis for Eq. (2.30) we have:

$$Amp(\phi_{back,y}) = \frac{1}{n_f} \cdot \frac{\partial n_f}{\partial T_f} \cdot \frac{P_0(1 - \exp(-\eta d))}{2k_{th,s} \cdot d \cdot L^2_y} \cdot \left(\frac{D_s}{\omega}\right)^{1/2} \times \exp\left(-\left(\frac{\omega}{2D_s}\right)^{1/2} y\right) \times \exp\left(-\left(\frac{\omega}{D_f} - \frac{\omega}{D_s}\right)^{1/2} L_x\right),$$

$$\times \left[(\sinh\gamma\cos\gamma)^2 + (\sin\gamma\cosh\gamma)^2\right]^{1/2} \times \left[(1 - \alpha + e^\beta\cos\beta + \alpha e^\beta\cos\beta)^2 + (e^\beta\sin\beta + \alpha e^\beta\sin\beta)^2\right]^{1/2}$$

$$(2.33)$$

$$Ph(\phi_{back,y}) = -\left(\frac{\omega}{D_f} - \frac{\omega}{D_s}\right)^{1/2} L_x + arctg(-tg\gamma \cdot ctgh\gamma) - \left(\frac{\omega}{2D_s}\right)^{1/2} y + \frac{3\pi}{4} + arctg\left(\frac{e^\beta\sin\beta + \alpha e^\beta\sin\beta}{1 - \alpha + e^\beta\cos\beta + \alpha e^\beta\cos\beta}\right).$$

$$(2.34)$$

We have calculated the amplitude and phase shift for the probe beam being emitted along the z-axis outside the surface area illuminated by the pump beam in equations (2.22-2.34). We observe that the amplitude and phase shift decrease exponentially as a function of y as we move away from the center which is being illuminated by the pump beam. This is expected since the temperature profile also decreases exponentially as a function of y which indicates that less heat is being propagated in that direction. This results in the thermal gradient and the deflection angle of the probe beam to also decrease in a similar manner.

For when the probe beam is emitted within the surface area illuminated by the pump beam $-\delta < y < \delta$ Figure 2.4(b), the deflection angle on the front side is:

$$\phi_{front,x} = \frac{1}{n_f} \cdot \frac{\partial n_f}{\partial T_f} \cdot \frac{P_0\left(1-\exp(-\eta d)\right)}{k_{th,s} \cdot d \cdot L^2_y} \cdot \left(\frac{D_s}{\omega}\right) \cdot \left(\frac{\omega}{D_f} - \frac{\omega}{D_s}\right)^{1/2}$$

$$\times \left[\left[1 - \left[\cos\left(\frac{\omega}{2D_s}\right)^{1/2} y \cdot \cosh\left(\frac{\omega}{2D_s}\right)^{1/2} y + \sin\left(\frac{\omega}{2D_s}\right)^{1/2} y \cdot \sinh\left(\frac{\omega}{2D_s}\right)^{1/2} y \right] \cdot \left[\exp(-\gamma) \cdot \cos\gamma\right] \right]^2 + \right.$$

$$\left. \left(\sin\gamma \cdot \left[\cos\left(\frac{\omega}{2D_s}\right)^{1/2} y \cdot \cosh\left(\frac{\omega}{2D_s}\right)^{1/2} y + \sin\left(\frac{\omega}{2D_s}\right)^{1/2} y \cdot \sinh\left(\frac{\omega}{2D_s}\right)^{1/2} y \right] \right)^2 \right]^{1/2}$$

$$\times \exp\left[i \left(arctg \left(\frac{\sin\gamma \cdot \left[\cos\left(\frac{\omega}{2D_s}\right)^{1/2} y \cdot \cosh\left(\frac{\omega}{2D_s}\right)^{1/2} y + \sin\left(\frac{\omega}{2D_s}\right)^{1/2} y \cdot \sinh\left(\frac{\omega}{2D_s}\right)^{1/2} y \right]}{1 - \left[\cos\left(\frac{\omega}{2D_s}\right)^{1/2} y \cdot \cosh\left(\frac{\omega}{2D_s}\right)^{1/2} y + \sin\left(\frac{\omega}{2D_s}\right)^{1/2} y \cdot \sinh\left(\frac{\omega}{2D_s}\right)^{1/2} y \right] \cdot \left[\exp(-\gamma) \cdot \cos\gamma\right]} \right) - \frac{\pi}{4} \right) \right]$$

(2.35)

Writing the amplitude and the phase shift along the *x*-axis for Eq. (2.35) we have:

$$Amp\left(\phi_{front,x}\right) = \frac{1}{n_f} \cdot \frac{\partial n_f}{\partial T_f} \cdot \frac{P_0\left(1-\exp(-\eta d)\right)}{k_{th,s} \cdot d \cdot L^2_y} \cdot \left(\frac{D_s}{\omega}\right) \cdot \left(\frac{\omega}{D_f} - \frac{\omega}{D_s}\right)^{1/2}$$

$$\left[\left(1 - \left[\cos\left(\frac{\omega}{2D_s}\right)^{1/2} y \cdot \cosh\left(\frac{\omega}{2D_s}\right)^{1/2} y + \sin\left(\frac{\omega}{2D_s}\right)^{1/2} y \cdot \sinh\left(\frac{\omega}{2D_s}\right)^{1/2} y \right] \cdot \left[\exp(-\gamma) \cdot \cos\gamma\right] \right)^2 \right.$$

$$\left. + \left(\sin\gamma \cdot \left[\cos\left(\frac{\omega}{2D_s}\right)^{1/2} y \cdot \cosh\left(\frac{\omega}{2D_s}\right)^{1/2} y + \sin\left(\frac{\omega}{2D_s}\right)^{1/2} y \cdot \sinh\left(\frac{\omega}{2D_s}\right)^{1/2} y \right] \right)^2 \right]^{1/2}$$

, (2.36)

$$Ph\left(\phi_{front,x}\right) = arctg \left(\frac{\sin\gamma \cdot \left[\cos\left(\frac{\omega}{2D_s}\right)^{1/2} y \cdot \cosh\left(\frac{\omega}{2D_s}\right)^{1/2} y + \sin\left(\frac{\omega}{2D_s}\right)^{1/2} y \cdot \sinh\left(\frac{\omega}{2D_s}\right)^{1/2} y \right]}{1 - \left[\cos\left(\frac{\omega}{2D_s}\right)^{1/2} y \cdot \cosh\left(\frac{\omega}{2D_s}\right)^{1/2} y + \sin\left(\frac{\omega}{2D_s}\right)^{1/2} y \cdot \sinh\left(\frac{\omega}{2D_s}\right)^{1/2} y \right] \cdot \left[\exp(-\gamma) \cdot \cos\gamma\right]} \right) - \frac{\pi}{4} .$$

(2.37)

With the same assumption that the probe beam is emitted along the *z*-axis inside the surface area illuminated by the pump beam, the deflection angle of the back side PDS signal for the corresponding transversal direction is:

$$\phi_{back,x} = \frac{1}{n_f} \cdot \frac{\partial n_f}{\partial T_f} \cdot \frac{P_0(1 - \exp(-\eta d))}{2k_s \cdot d \cdot L_y^2} \cdot \left(\frac{D_s}{\omega}\right) \cdot \left(\frac{\omega}{D_f} - \frac{\omega}{D_s}\right)^{1/2} \times \exp\left(-\left(\frac{\omega}{D_f} - \frac{\omega}{D_s}\right)^{1/2} L_x\right)$$

$$\times \left[(1 - \alpha + e^\beta \cos\beta + \alpha e^\beta \cos\beta)^2 + (e^\beta \sin\beta + \alpha e^\beta \sin\beta)^2\right]^{1/2}$$

$$\times \left[\left[1 - \left[\cos\left(\frac{\omega}{2D_s}\right)^{1/2} y \cdot \cosh\left(\frac{\omega}{2D_s}\right)^{1/2} y + \sin\left(\frac{\omega}{2D_s}\right)^{1/2} y \cdot \sinh\left(\frac{\omega}{2D_s}\right)^{1/2} y\right] \cdot [\exp(-\gamma) \cdot \cos\gamma]\right]^2\right.$$

$$\left.+ \left(\sin\gamma \cdot \left[\cos\left(\frac{\omega}{2D_s}\right)^{1/2} y \cdot \cosh\left(\frac{\omega}{2D_s}\right)^{1/2} y + \sin\left(\frac{\omega}{2D_s}\right)^{1/2} y \cdot \sinh\left(\frac{\omega}{2D_s}\right)^{1/2} y\right]\right)^2\right]^{1/2}$$

$$\times \exp\left[i\left(-\left(\frac{\omega}{D_f} - \frac{\omega}{D_s}\right)^{1/2} L_x + \frac{3\pi}{4} + arctg\left(\frac{e^\beta \sin\beta + \alpha e^\beta \sin\beta}{1 - \alpha + e^\beta \cos\beta + \alpha e^\beta \cos\beta}\right)\right)\right]$$

$$\times \exp\left[i\left(arctg\left(\frac{\sin\gamma \cdot \left[\cos\left(\frac{\omega}{2D_s}\right)^{1/2} y \cdot \cosh\left(\frac{\omega}{2D_s}\right)^{1/2} y + \sin\left(\frac{\omega}{2D_s}\right)^{1/2} y \cdot \sinh\left(\frac{\omega}{2D_s}\right)^{1/2} y\right]}{1 - \left[\cos\left(\frac{\omega}{2D_s}\right)^{1/2} y \cdot \cosh\left(\frac{\omega}{2D_s}\right)^{1/2} y + \sin\left(\frac{\omega}{2D_s}\right)^{1/2} y \cdot \sinh\left(\frac{\omega}{2D_s}\right)^{1/2} y\right] \cdot [\exp(-\gamma) \cdot \cos\gamma]}\right)\right)\right].$$

$$(2.38)$$

Writing the amplitude and the phase shift along the *x*-axis for Eq. (2.38) we have:

$$Amp(\phi_{back,x}) = \phi_{back,x} = \frac{1}{n_f} \cdot \frac{\partial n_f}{\partial T_f} \cdot \frac{P_0(1 - \exp(-\eta d))}{2k_{th,s} \cdot d \cdot L_y^2} \cdot \left(\frac{D_s}{\omega}\right) \cdot \left(\frac{\omega}{D_f} - \frac{\omega}{D_s}\right)^{1/2} \times \exp\left(-\left(\frac{\omega}{D_f} - \frac{\omega}{D_s}\right)^{1/2} L_x\right)$$

$$\times \left[(1 - \alpha + e^\beta \cos\beta + \alpha e^\beta \cos\beta)^2 + (e^\beta \sin\beta + \alpha e^\beta \sin\beta)^2\right]^{1/2}$$

$$\times \left[\left[1 - \left[\cos\left(\frac{\omega}{2D_s}\right)^{1/2} y \cdot \cosh\left(\frac{\omega}{2D_s}\right)^{1/2} y + \sin\left(\frac{\omega}{2D_s}\right)^{1/2} y \cdot \sinh\left(\frac{\omega}{2D_s}\right)^{1/2} y\right] \cdot [\exp(-\gamma) \cdot \cos\gamma]\right]^2\right. \qquad , (2.39)$$

$$\left.+ \left(\sin\gamma \cdot \left[\cos\left(\frac{\omega}{2D_s}\right)^{1/2} y \cdot \cosh\left(\frac{\omega}{2D_s}\right)^{1/2} y + \sin\left(\frac{\omega}{2D_s}\right)^{1/2} y \cdot \sinh\left(\frac{\omega}{2D_s}\right)^{1/2} y\right]\right)^2\right]^{1/2}$$

$$Ph(\phi_{back,x}) = -\left(\frac{\omega}{D_f} - \frac{\omega}{D_s}\right)^{1/2} L_x + \frac{3\pi}{4} + arctg\left(\frac{e^\beta \sin\beta + \alpha e^\beta \sin\beta}{1 - \alpha + e^\beta \cos\beta + \alpha e^\beta \cos\beta}\right)$$

$$+ arctg\left(\frac{\sin\gamma \cdot \left[\cos\left(\frac{\omega}{2D_s}\right)^{1/2} y \cdot \cosh\left(\frac{\omega}{2D_s}\right)^{1/2} y + \sin\left(\frac{\omega}{2D_s}\right)^{1/2} y \cdot \sinh\left(\frac{\omega}{2D_s}\right)^{1/2} y\right]}{1 - \left[\cos\left(\frac{\omega}{2D_s}\right)^{1/2} y \cdot \cosh\left(\frac{\omega}{2D_s}\right)^{1/2} y + \sin\left(\frac{\omega}{2D_s}\right)^{1/2} y \cdot \sinh\left(\frac{\omega}{2D_s}\right)^{1/2} y\right] \cdot [\exp(-\gamma) \cdot \cos\gamma]}\right). (2.40)$$

We have calculated the amplitude and phase shift for the probe beam being emitted along the *z*-axis inside the surface area illuminated by the pump beam in equations (2.35-2.40). Since the probe beam is emitted across the surface area illuminated by the pump beam $-\delta<y<\delta$, the phase shift and amplitude decrease exponentially as a function of $[1-(\delta-y)]$ as we move from the center to the point $\delta=y$.

In this section, the deflection angle of the probe beam has been calculated along the *z*-direction on the front and back side of the PDS system. From the deflection angle, we have computed the amplitude and the phase shift of the PDS signal. As can be seen by equations (2.26), (2.28) and (2.37) the phase shift is no longer a constant on the front side of the PDS system and its value depends on the geometrical and thermal properties of the system.

2.4 Analytical model for substrate-side photothermal deflection

2.4.1 Substrate being illuminated by the pump beam

In the new configuration of the PDS system, we illuminate the thin film-substrate from the substrate side. First, we assume we only have a 3-dimensional substrate with a limited thickness being illuminated by a thin pump beam. By illuminating the substrate at the center the substrate heats up and propagates heat throughout itself as well as the photothermal fluid surrounding it. Due to the substrate heating up, the refractive index of the photothermal fluid surrounding it changes and the probe beam passing alongside the front and back side surface of the substrate gets deflected as can be seen in Figure 2.5.
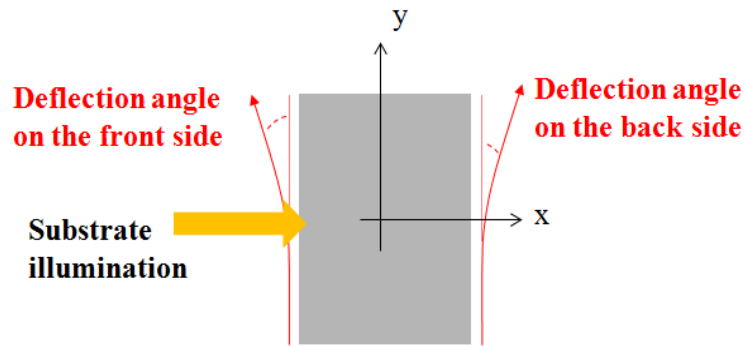
Figure 2.5: The substrate immersed in a photothermal fluid is being illuminated by a thin beam from one side. Due to the substrate heating up the refractive index the photothermal fluid surrounding it changes and the probe beam passing alongside the front and back surface of the substrate gets deflected.

The model can later be expanded by putting a 2-dimensional thin film on the other side of the PDS system with various thermal properties with respect to the substrate.

2.4.2 Calculating the temperature profile

The temperature profiles in the substrate and the surrounding medium are governed by the Fourier equation of heat Eq. (2.4). Since we are illuminating the center of the substrate with a thin beam we assume that the temperature drops exponentially on the surface of the substrate once we start to go further away from the center. By using separation of variables method we find the temperature profile as a series of solutions with different eigenvalues for the photothermal fluid on the front side, the substrate and the photothermal fluid on the back side. We write them in order as:

$$\theta_{fF}(x,y,t) = A e^{-a|y|} e^{(\frac{i\omega}{D_f}-a^2)^{1/2}x} e^{i\omega t}, \tag{2.41}$$

$$\theta_{b'}(x,y,t) = e^{-b|y|}(A'e^{(\frac{i\omega}{D_b}-b^2)^{1/2}x} + B'e^{-(\frac{i\omega}{D_b}-b^2)^{1/2}x})e^{i\omega t}, \tag{2.42}$$

$$\theta_{fB}(x,y,t) = A''e^{-c|y|} e^{-(\frac{i\omega}{D_{f'}}-c^2)^{1/2}x} e^{i\omega t}. \tag{2.43}$$

The subscripts *fF* and *fB* indicate the fluid on the front and back side of the substrate while the subscript *b′* indicates the substrate (background medium). The *D* is the thermal diffusivity and *a*, *b* and *c* indicate the different eigenvalues of the temperature which should be summed over. *A*, *A′*, *B′* and *A″* are constants that we evaluate by imposing the certain boundary conditions related to the system under study.

2.4.3 Temperature profile of the substrate

To compute the temperature profile of the substrate we divide it into two symmetric and antisymmetric profiles. We then have a set of Fourier harmonics for the different sets of eigenvalues for the symmetric and antisymmetric temperature profiles. Due to the linear characteristic of Fourier's equation, for which the principle of superposition is valid, we add the two symmetric and antisymmetric temperature profiles with each other and get the final result.

To get a symmetric temperature profile we assume that we illuminate the substrate from both sides, Figure 2.6(a) and to get the antisymmetric temperature profile we assume we are heating the sample from one side and extracting the same amount of heat from the other side,

26

Figure 2.6(b). Summing the two aforementioned models gives us a model equivalent to the substrate being illuminated from one side, Figure 2.6(c).
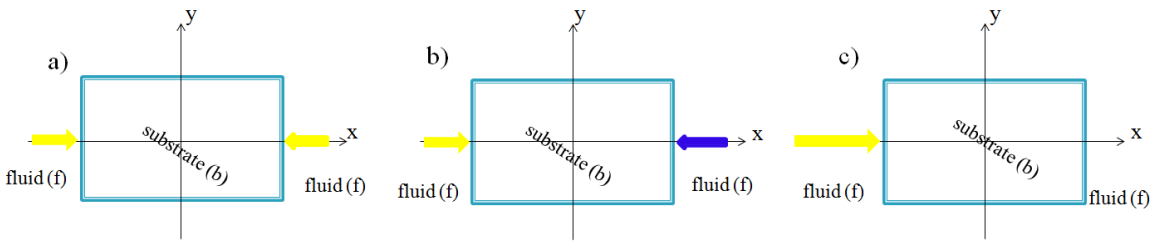
Figure 2.6: a) The substrate being illuminated from both sides creating a symmetric temperature profile. b) The substrate is illuminated from one side while the exact amount of heat is being taken away from the system on the other side creating an antisymmetric temperature profile. c) Summing the two models will give us the exact setup that we have with the substrate being illuminated from one side.

The symmetric and antisymmetric temperature profiles which are the result of the models discussed in Figure 2.6 are shown in Figure 2.7(a) and 2.7(b). The green and red lines for the temperature profiles of Figure 2.7(a) and 2.7(b) indicate different thermal diffusivities within the substrate, with green line showing a substrate with low thermal diffusivity which the substrate reaches its maximum temperature very close to the surface of illumination and the red line shows a substrate with high thermal diffusivity which heat penetrates within the substrate much more and therefore the maximum temperature is much further from its surface of illumination. Due to the linear character of Fourier's equation, we add the two temperature profiles together and arrive at the temperature profile of the PDS system in use Figure 2.7(c).
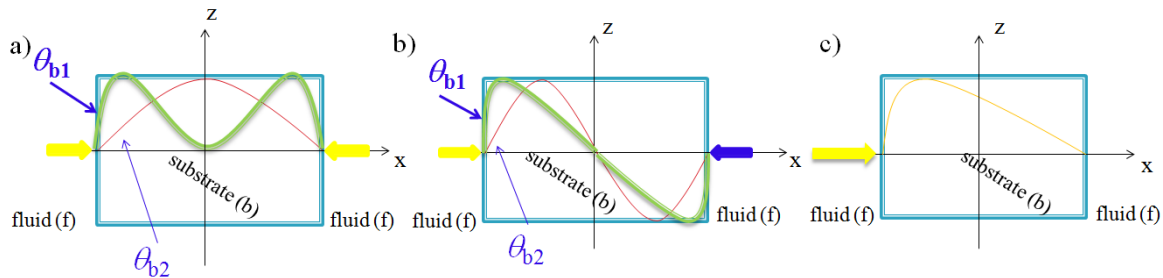
Figure 2.7: a) The symmetric temperature profile designated by red and green lines with the red line indicating a substrate with low thermal diffusivity and the green line indicating a substrate with high thermal diffusivity. b) The antisymmetric temperature profile designated by red and green lines. c) The sum of the two temperature profiles which gives us the temperature profile of the PDS system in hand.

27

To get the temperature profile we also use the rule of conservation of energy at the boundaries where the heat flow should be conserved throughout the substrate and the photothermal fluid surrounding it. Unlike the model we had in the previous section where heat was absorbed only by the 2-dimensional thin film, in this case, the heat penetrates through the surface of the substrate as shown in Figure 2.8. The equation for the boundary condition is written as:

$$2k_{th,b'} \frac{\partial \theta_{b'}(x,y,t)}{\partial y} + k_{th,b'} \frac{\partial \theta_{b'}(x,y,t)}{\partial x} + k_{th,f} \frac{\partial \theta_f(x,y,t)}{\partial x} = q_0 , \qquad (2.44)$$

where $k_{th,b'}$ and $k_{th,f}$ are the thermal conductivity of the substrate and the fluid and q_0 is the amount of heat absorbed by the substrate. Since the thermal conductivity of the photothermal fluid is much less than the thermal conductivity of the substrate we can write Eq. (2.44) as:

$$2k_{th,b'} \frac{\partial \theta_{b'}(x,y,t)}{\partial y} + k_{th,b'} \frac{\partial \theta_{b'}(x,y,t)}{\partial x} = q_0 . \qquad (2.45)$$
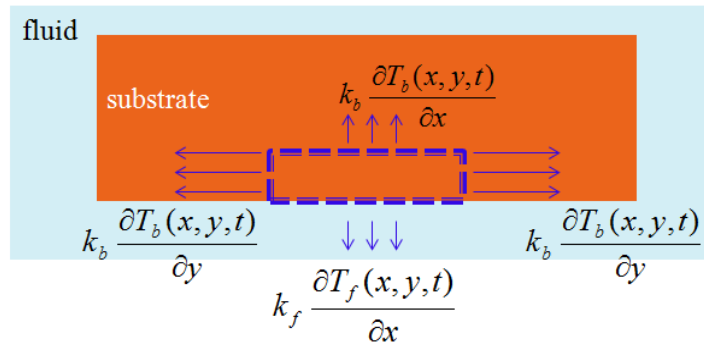
Figure 2.8: The heat flow throughout the substrate once being illuminated by the pump beam.

Now we have all the necessary tools for calculating the temperature profile for the symmetric and antisymmetric model and then add them up to get the actual temperature profile.

a) Symmetric temperature profile

In this model, the back and the front side of the substrate is being illuminated, creating a symmetric temperature profile. Implementing this boundary condition for Eq. (2.42) we have:

$$\theta_{b'}(x = -\frac{L}{2}, y) = \theta_{b'}(x = \frac{L}{2}, y) \Rightarrow A' = B' , \qquad (2.46)$$

28

where L is the thickness of the substrate. Also by implementing the boundary conditions at the surface of contact between the substrate and the fluid we have:

$$\theta_f(x = -\frac{L}{2}, y) = \theta_{b'}(x = -\frac{L}{2}, y) \Rightarrow a = b, \tag{2.47}$$

$$\theta_{b'}(x = \frac{L}{2}, y) = \theta_{f'}(x = \frac{L}{2}, y) \Rightarrow a = b = c. \tag{2.48}$$

By implementing the above boundary conditions into Eq. (2.42) the temperature profile for the substrate in the symmetric model is:

$$\theta_{b'}(x, y, t, b) = A' e^{-b|y|}(e^{(\frac{i\omega}{D_b} - b^2)^{1/2} x} + e^{-(\frac{i\omega}{D_b} - b^2)^{1/2} x}) e^{i\omega t}. \tag{2.49}$$

To find the constant value A' we insert Eq. (2.49) into Eq. (2.46) and get:

$$-2k_b b A'[e^{(\frac{i\omega}{D_b} - b^2)^{1/2} \frac{L}{2}} + e^{-(\frac{i\omega}{D_b} - b^2)^{1/2} \frac{L}{2}}] + k_b(\frac{i\omega}{D_b} - b^2)^{1/2} A'[e^{(\frac{i\omega}{D_b} - b^2)^{1/2} \frac{L}{2}} - e^{-(\frac{i\omega}{D_b} - b^2)^{1/2} \frac{L}{2}}] = q_0,$$

$$\Rightarrow A' = \frac{\left(\dfrac{q_0}{k_{th,b}}\right)}{\left[\left(\dfrac{i\omega}{D_b} - b^2\right)^{\frac{1}{2}} - 2b\right] \cdot e^{-\left(\frac{i\omega}{D_b} - b^2\right)^{\frac{1}{2}} \frac{L}{2}} - \left[\left(\dfrac{i\omega}{D_b} - b^2\right)^{\frac{1}{2}} + 2b\right] \cdot e^{\left(\frac{i\omega}{D_b} - b^2\right)^{\frac{1}{2}} \frac{L}{2}}}. \tag{2.50}$$

To get the temperature profile for the symmetric model we write it as a series of solutions with energy eigenvalues b. Inserting the constant value A' into Eq. (2.49) we write the temperature profile as:

$$T_{b'}(x, y, t) = \frac{q_0 e^{i\omega t}}{k_{th,b}} \int_0^\infty db \frac{e^{-\left(\frac{i\omega}{D_b} - b^2\right)^{1/2} x} + e^{\left(\frac{i\omega}{D_b} - b^2\right)^{1/2} x}}{\left[\left(\dfrac{i\omega}{D_b} - b^2\right)^{1/2} - 2b\right] \cdot e^{-\left(\frac{i\omega}{D_b} - b^2\right)^{1/2} \frac{L}{2}} - \left[\left(\dfrac{i\omega}{D_b} - b^2\right)^{1/2} + 2b\right] \cdot e^{\left(\frac{i\omega}{D_b} - b^2\right)^{1/2} \frac{L}{2}}} \cdot e^{-b|y|}. \tag{2.51}$$

To solve this integral and find the symmetric temperature profile of the substrate we go to the complex space and draw a contour to find the poles necessary to solve the integral. The complete solution can be found in Appendix I. The final temperature profile for the symmetric temperature profile is:

$$T_b(x, y, t) = 2\pi i\left(\frac{q_0}{k_b}\right)e^{i\omega t}$$

$$\left[\left(e^{-\left(\frac{i\omega}{D_b}-z_1^4\right)^{1/2}x} + e^{\left(\frac{i\omega}{D_b}-z_1^4\right)^{1/2}x}\right)\cdot e^{-z_1^2|y|}\cdot 2z_1 + \left(e^{-\left(\frac{i\omega}{D_b}-z_2^4\right)^{1/2}x} + e^{\left(\frac{i\omega}{D_b}-z_2^4\right)^{1/2}x}\right)\cdot e^{-z_2^2|y|}\cdot 2z_2\right],\quad(2.52)$$

where z_1 and z_2 are the specific eigenvalues of the temperature profile which are:

$$z_1 =^+_- \frac{\left(+4+(16-4i\frac{\omega L^2}{D_b})^{1/2}\right)^{1/2}}{L^{1/2}},\quad z_2 =^+_- \frac{\left(+4-(16-4i\frac{\omega L^2}{D_b})^{1/2}\right)^{1/2}}{L^{1/2}}.\quad(2.53)$$

b) Antisymmetric temperature profile

In this case, the front side of the substrate is being illuminated by the pump beam while the same amount of heat is being extracted from the back side, creating an antisymmetric temperature profile. Implementing this boundary condition from Eq. (2.42) we have:

$$\theta_{b'}(x=-\frac{L}{2}, y) = -\theta_{b'}(x=\frac{L}{2}, y) \Rightarrow A' = -B'.\quad(2.54)$$

This leads to the following:

$$\theta_{b'}(x, y, t, b) = A'e^{-b|y|}(e^{(\frac{i\omega}{D_b}-b^2)^{1/2}x} - e^{-(\frac{i\omega}{D_b}-b^2)^{1/2}x})e^{i\omega t}.\quad(2.55)$$

To find the constant value A' we insert Eq. (2.54) into Eq. (2.42) and get:

$$-2k_{th,b}bA'[e^{-(\frac{i\omega}{D_b}-b^2)^{1/2}\frac{L}{2}} - e^{(\frac{i\omega}{D_b}-b^2)^{1/2}\frac{L}{2}}] + k_{th,b}(\frac{i\omega}{D_b}-b^2)^{1/2}A'[e^{-(\frac{i\omega}{D_b}-b^2)^{1/2}\frac{L}{2}} + e^{(\frac{i\omega}{D_b}-b^2)^{1/2}\frac{L}{2}}] = q_0,$$

$$\Rightarrow A' = \frac{\left(\frac{q_0}{k_b}\right)}{\left[\left(\frac{i\omega}{D_b}-b^2\right)^{\frac{1}{2}} - 2b\right]\cdot e^{-\left(\frac{i\omega}{D_b}-b^2\right)^{\frac{1}{2}}\frac{L}{2}} + \left[\left(\frac{i\omega}{D_b}-b^2\right)^{\frac{1}{2}} + 2b\right]\cdot e^{\left(\frac{i\omega}{D_b}-b^2\right)^{\frac{1}{2}}\frac{L}{2}}}.\quad(2.56)$$

Just like the symmetric temperature profile we write the antisymmetric temperature profile as a series of solutions with energy eigenvalues b. We write the temperature profile for the substrate as:

$$T_{b'}(x,y,t) = \frac{q_0 e^{i\omega t}}{k_{th,b}} \int_0^\infty db \frac{\left(e^{\left(\frac{i\omega}{D_b}-b^2\right)^{1/2}x} - e^{-\left(\frac{i\omega}{D_b}-b^2\right)^{1/2}x} \right)\cdot e^{-b|y|}}{\left[\left(\frac{i\omega}{D_b}-b^2\right)^{1/2}-2b\right]\cdot e^{-\left(\frac{i\omega}{D_b}-b^2\right)^{1/2}\frac{L}{2}} + \left[\left(\frac{i\omega}{D_b}-b^2\right)^{1/2}+2b\right]\cdot e^{\left(\frac{i\omega}{D_b}-b^2\right)^{1/2}\frac{L}{2}}},$$

(2.57)

To solve this integral and find the antisymmetric temperature profile of the substrate we go to the complex space and draw a contour to find the poles necessary to solve the integral. The complete solution can be found in Appendix I. The final temperature profile for the antisymmetric temperature profile is:

$$T_b(x,y,t) = 2\pi i \left(\frac{q_0}{k_{th,b}}\right) e^{i\omega t} \left(e^{\left(\frac{i\omega}{D_b}-z_3^4\right)^{1/2}x} - e^{-\left(\frac{i\omega}{D_b}-z_3^4\right)^{1/2}x} \right)\cdot e^{-z_3^2|y|} z_3,$$

(2.58)

where z_3 is the specific eigenvalue of the temperature profile which is:

$$z_3 = \overset{+}{_{-}} i\sqrt{\frac{1}{L}}.$$

(2.59)

c) Final temperature profile of the substrate

Since the superposition principle is valid for Fourier's heat equation we add the symmetric and antisymmetric temperature profiles with each other. The temperature profile of the substrate is:

$$T_b(x,y,t) = 2\pi\ i \left(\frac{q_0}{k_{th,b}}\right) e^{i\omega t}$$

$$\left\{ 2z_1 \left(e^{-\left(\frac{i\omega}{D_b}-z_1^4\right)^{1/2}x} + e^{\left(\frac{i\omega}{D_b}-z_1^4\right)^{1/2}x} \right) e^{-z_1^2|y|} + 2z_2 \left(e^{-\left(\frac{i\omega}{D_b}-z_2^4\right)^{1/2}x} + e^{\left(\frac{i\omega}{D_b}-z_2^4\right)^{1/2}x} \right) e^{-z_2^2|y|} + z_3 \left(e^{\left(\frac{i\omega}{D_b}-z_3^4\right)^{1/2}x} - e^{-\left(\frac{i\omega}{D_b}-z_3^4\right)^{1/2}x} \right) e^{-z_3^2|y|} \right\}.$$

(2.60)

The temperature profile of the substrate computed has three eigenvalues which are the positive values of z_1, z_2 and z_3.

2.4.4 Temperature profile of the fluid

To find the deflection angle of the probe beam passing through the surface of the substrate we need to find the temperature profile of the fluid. We assume that the temperature profile is

continuous passing through the substrate to the fluid. Therefore the boundary condition we apply on the surface of the interface between the fluid and the substrate is:

$$\theta_f(x =^+_- \frac{L}{2}, y) = \theta_b(x =^+_- \frac{L}{2}, y). \tag{2.61}$$

We find the constant values A Eq. (2.41) and A'' Eq. (2.43) by using the aforementioned boundary condition. Again we write the temperature profile in a Fourier set of harmonics, solve the integral and find the specific eigenvalues for the temperature.

The temperature profile of the fluid for the front side of the PDS system is:

$$T_{fF}(x, y, t) = -2\pi i \frac{q_0 e^{i\omega t}}{k_{th,b}}$$

$$\left\{ z_3 \cdot \left[L + \left(\frac{i\omega}{D_f} - z_3^4 \right)^{1/2} \frac{L^2}{2} \right] \cdot e^{(\frac{i\omega}{D_f} - z_3^4)^{1/2} x} \cdot e^{-z_3^2 |y|} + \right.$$

$$\left. 4 z_1 \cdot \left[1 + (\frac{i\omega}{D_f} - z_1^4)^{1/2} \frac{L}{2} \right] \cdot e^{(\frac{i\omega}{D_f} - z_1^4)^{1/2} x} e^{-z_1^2 |y|} + 4 z_2 \cdot \left[1 + (\frac{i\omega}{D_f} - z_2^4)^{1/2} \frac{L}{2} \right] \cdot e^{(\frac{i\omega}{D_f} - z_2^4)^{1/2} x} e^{-z_2^2 |y|} \right\} \tag{2.62}$$

The temperature profile of the fluid for the back side the PDS system is:

$$T_{fB}(x, y, t) = -2\pi i \frac{q_0 e^{i\omega t}}{k_{th,b}}$$

$$\left\{ -z_3 \cdot \left[L + \left(\frac{i\omega}{D_f} - z_3^4 \right)^{1/2} \frac{L^2}{2} \right] \cdot e^{-(\frac{i\omega}{D_f} - z_3^4)^{1/2} x} \cdot e^{-z_3^2 |y|} + \right.$$

$$\left. 4 z_1 \cdot \left[1 + (\frac{i\omega}{D_f} - z_1^4)^{1/2} \frac{L}{2} \right] \cdot e^{-(\frac{i\omega}{D_f} - z_1^4)^{1/2} x} e^{-z_1^2 |y|} + 4 z_2 \cdot \left[1 + (\frac{i\omega}{D_f} - z_2^4)^{1/2} \frac{L}{2} \right] \cdot e^{-(\frac{i\omega}{D_f} - z_2^4)^{1/2} x} e^{-z_2^2 |y|} \right\} \tag{2.63}$$

Having the temperature profile of the fluid on the front and back side of the substrate we can use Fermat's principle to calculate the deflection angle.

2.4.5 Measuring deflection angle of the probe beam

After heat is generated in the substrate, it will transmit to the photothermal fluid. In the system under study, the substrate is periodically heated from illumination by the pump beam at a frequency ω and the consequent, periodic, thermal gradient at the substrate interface with the photothermal fluid is detected from the periodic changes in refractive index of the photothermal fluid.

Implementing Eq. (2.62) and Eq. (2.63), the temperature profile of the fluid on the front and back side of the substrate into Eq. (2.2) we measure the deflection angle of the system with the *y*-axis going from +*h* to -*h*.

The deflection angle on the front side is:

$$\phi_F = \frac{1}{n_f}\frac{\partial n_f}{\partial T_f}\int_{-h}^{+h}\left.\frac{\partial T_{fF}}{\partial x}\right|_s dy \Rightarrow$$

$$\phi_F = -\frac{2\pi i}{n_f}\frac{\partial n_f}{\partial T_f}\frac{q_0 e^{i\omega t}}{k_{th,b}}\cdot$$

$$
\left\{ z_3\cdot\left[L+\left(\frac{i\omega}{D_f}-z_3{}^4\right)^{\frac{1}{2}}\frac{L^2}{2}\right]\cdot\left[\left(\frac{i\omega}{D_f}-z_3{}^4\right)^{\frac{1}{2}}\right]\cdot e^{-\left(\frac{i\omega}{D_f}-z_3{}^4\right)^{\frac{1}{2}}\left(\frac{L}{2}\right)}\cdot\left[\frac{2}{z_3{}^2}-\frac{e^{-hz_3{}^2}}{z_3{}^2}\right]+ \right.
$$

$$
4z_1\cdot\left[1+\left(\frac{i\omega}{D_f}-z_1{}^4\right)^{\frac{1}{2}}\frac{L}{2}\right]\cdot\left[\left(\frac{i\omega}{D_f}-z_1{}^4\right)^{\frac{1}{2}}\right]\cdot e^{-\left(\frac{i\omega}{D_f}-z_1{}^4\right)^{\frac{1}{2}}\left(\frac{L}{2}\right)}\cdot\left[\frac{2}{z_1{}^2}-\frac{e^{-hz_1{}^2}}{z_1{}^2}\right]+
$$

$$
\left. 4z_2\cdot\left[1+\left(\frac{i\omega}{D_f}-z_2{}^4\right)^{\frac{1}{2}}\frac{L}{2}\right]\cdot\left[\left(\frac{i\omega}{D_f}-z_2{}^4\right)^{\frac{1}{2}}\right]\cdot e^{-\left(\frac{i\omega}{D_f}-z_2{}^4\right)^{\frac{1}{2}}\left(\frac{L}{2}\right)}\cdot\left[\frac{2}{z_2{}^2}-\frac{e^{-hz_2{}^2}}{z_2{}^2}\right] \right\}
$$

(2.64)

and the deflection angle on the back side is:

$$\phi_F = \frac{1}{n_f}\frac{\partial n_f}{\partial T_f}\int_{-h}^{+h}\left.\frac{\partial T_{fF}}{\partial x}\right|_s dy \Rightarrow$$

$$\phi_F = -\frac{2\pi i}{n_f}\frac{\partial n_f}{\partial T_f}\frac{q_0 e^{i\omega t}}{k_{th,b}}\cdot$$

$$
\left\{ z_3\cdot\left[L+\left(\frac{i\omega}{D_f}-z_3{}^4\right)^{\frac{1}{2}}\frac{L^2}{2}\right]\cdot\left[\left(\frac{i\omega}{D_f}-z_3{}^4\right)^{\frac{1}{2}}\right]\cdot e^{-\left(\frac{i\omega}{D_f}-z_3{}^4\right)^{\frac{1}{2}}\left(\frac{L}{2}\right)}\cdot\left[\frac{2}{z_3{}^2}-\frac{e^{-hz_3{}^2}}{z_3{}^2}\right]- \right.
$$

$$
4z_1\cdot\left[1+\left(\frac{i\omega}{D_f}-z_1{}^4\right)^{\frac{1}{2}}\frac{L}{2}\right]\cdot\left[\left(\frac{i\omega}{D_f}-z_1{}^4\right)^{\frac{1}{2}}\right]\cdot e^{-\left(\frac{i\omega}{D_f}-z_1{}^4\right)^{\frac{1}{2}}\left(\frac{L}{2}\right)}\cdot\left[\frac{2}{z_1{}^2}-\frac{e^{-hz_1{}^2}}{z_1{}^2}\right]-
$$

$$
\left. 4z_2\cdot\left[1+\left(\frac{i\omega}{D_f}-z_2{}^4\right)^{\frac{1}{2}}\frac{L}{2}\right]\cdot\left[\left(\frac{i\omega}{D_f}-z_2{}^4\right)^{\frac{1}{2}}\right]\cdot e^{-\left(\frac{i\omega}{D_f}-z_2{}^4\right)^{\frac{1}{2}}\left(\frac{L}{2}\right)}\cdot\left[\frac{2}{z_2{}^2}-\frac{e^{-hz_2{}^2}}{z_2{}^2}\right] \right\}
$$

(2.65)

The eigenvalues in Eq. (2.64) and Eq. (2.65) which come from equations (2.53) and (2.59) depend on the width of the substrate *L*, the frequency of the chopper ω and the thermal

diffusivity of the substrate itself D_b. Therefore the deflection angle would vary by applying substrates with different thermal diffusivities and different thicknesses.

We have calculated the deflection angle of the 3-dimensional substrate. Later on, we can attach a 2-dimensional thin film to the substrate and find the deflection angle for the thin film-substrate system. If the thermal conductivity of the substrate is much higher than the thermal conductivity of the thin film the same results that were conducted in Eq. (2.64) and Eq. (65) will hold. By applying a specific substrate with a known thermal diffusivity and a known thickness we can find the amplitude and the phase shift for the front side Eq. (2.65) and back side Eq. (2.66) of the PDS system which are required to compute the thermal conductivity of the system.

2.5 Results and Discussion

In this section, we analyze the analytical results which we have acquired for the thin film-substrate and compare them with the experimental results. We take the probe beam to be directed along the *z*-direction and to be moving along the *y*-axis passing near the front and back side of the thin film-substrate. We then analyze our results at different frequencies and compare them with the experimental measurements done on the system. We also analyze the results for the substrate with various thicknesses.

Figure 2.9 shows the analytical solution for the front and back side amplitude of the probe beam deflected in the transversal direction for the thin film-substrate. We assume the thin film side is being illuminated by the pump beam and the thin film has a much higher thermal conductivity than the substrate, equations (2.25), (2.31), (2.36), (2.39). The PDS system under consideration is composed of a 200nm thin gold film attached to a 0.23mm glass substrate. The pump beam has a wavelength of 407nm and is emitted at frequencies equal to 10Hz, 20Hz and 40Hz.
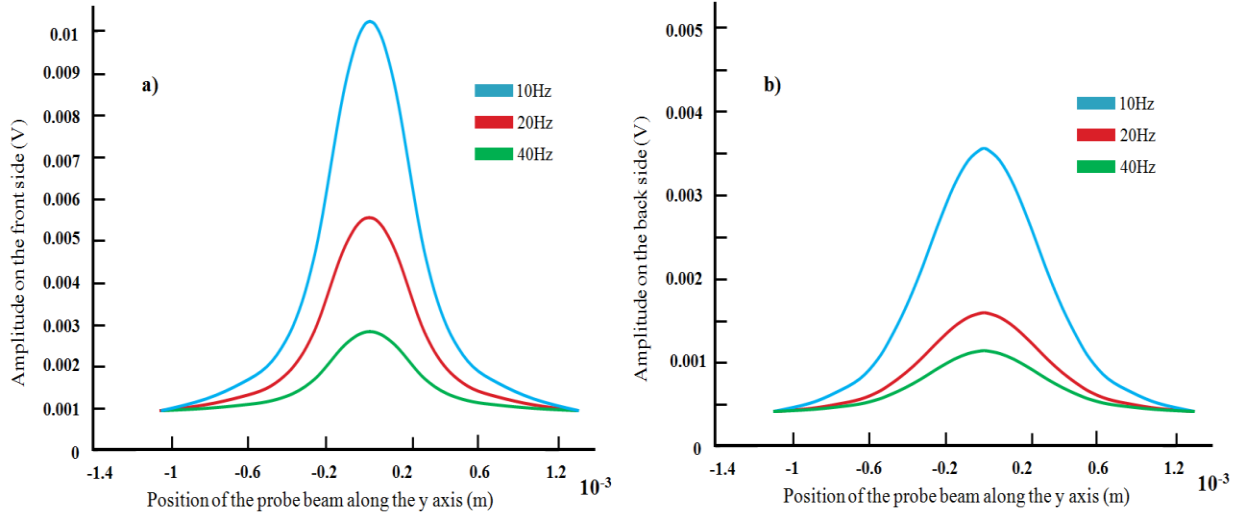
Figure 2.9: a) The front side amplitude of the deflected probe beam in the transversal direction Eq. (2.25), Eq. (2.36) for three different frequencies. b) The back side amplitude of the deflected probe beam in the transversal direction Eq. (2.31), Eq. (2.39) for three different frequencies.

Since the amount of heat absorbed by the front side of the thin film-substrate is more than the amount of heat absorbed by its backside, there is more heat exchange between the thin film-substrate and the fluid on the front side than on the back side. Therefore we expect the amplitude on the front side to be greater Figure 2.9(a) than the amplitude on the back side Figure 2.9(b). Furthermore, as the frequency of the pump beam increases the amplitude decreases. This is expected since as the frequency increases the sample has less time to absorb heat and increase its amplitude. Analyzing the amplitude peaks Figure 2.9 we observe a broader amplitude peak on the back side than on the front side of the thin film-substrate. We can explain this phenomenon by stating that we when heat propagates throughout the substrate from the front side to the back side it not only propagates in the x-direction but it also propagates in the y-direction resulting in a broader amplitude peak on the back side than on the front side.

Figure 2.10 shows the experimental measurements carried out on the thin gold film attached to a glass substrate at frequencies 10Hz, 20Hz and 40Hz. By comparing Figures 2.9 and 2.10 for the amplitude on the front and back side of the PDS system for the thin film-substrate system, we see that the experiment is in accordance with the analytical solution that has been devised for the PDS system.

35
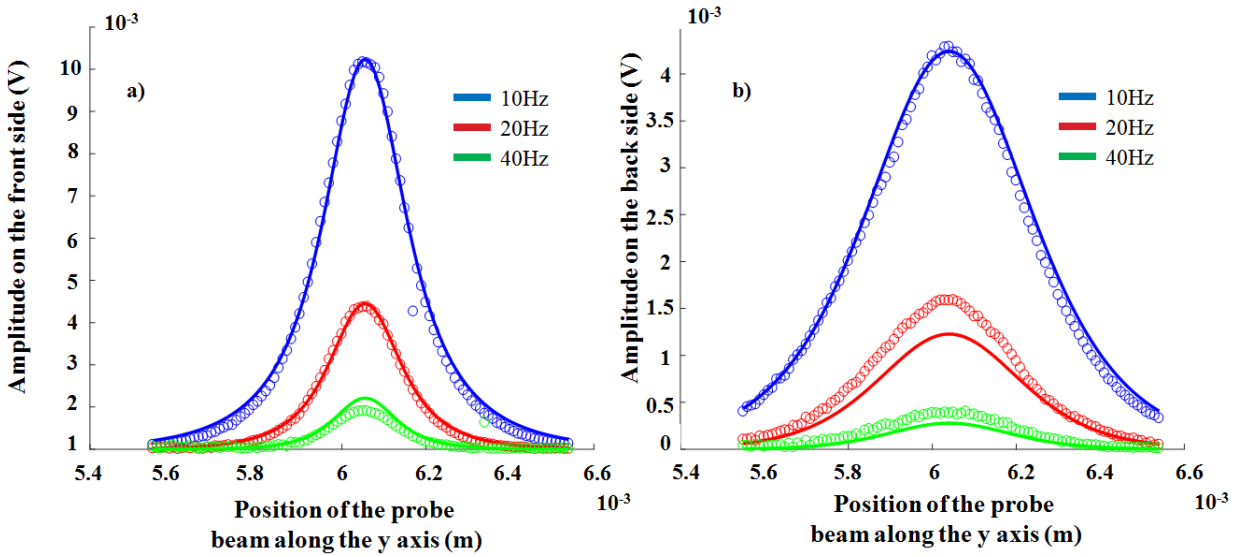
Figure 2.10: a) The front side amplitude of the probe beam being emitted along the *z*-direction and being deflected in the x-direction at three different frequencies. b) The back side amplitude of the probe beam being emitted along the *z*-direction and being deflected in the x-direction at three different frequencies. The continuous lines are the numerical fittings of the experimental results.

Figure 2.11 shows the analytical solution for the back side amplitude of the probe beam deflected in the transversal direction, Eq. (2.33) and Eq. (2.39), with the substrate having various thicknesses. We again take the probe beam to be directed along the *z*-direction and to be moving along the *y*-axis passing near the back side of the thin film-substrate. The PDS system is composed of a 200nm thin gold film attached to a glass substrate with thicknesses equal to 0.23mm, 2.3mm and 23 mm. The pump beam has a wavelength of 407nm and is illuminating the thin film at a frequency 10Hz.

As we increase the thickness of the substrate the deflection angle on the back side decreases. This is as expected since as the substrate gets thicker there would be less heat penetration from the front side to the back side of the sample. The deflection angle remains the same on the front side and the thickness of the substrate doesn't affect it at all.

36
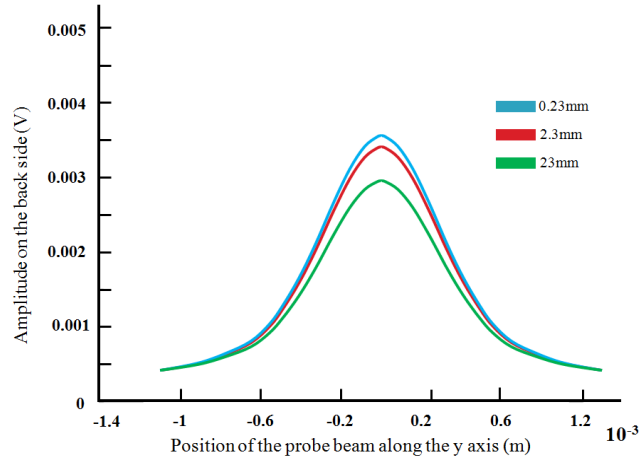
Figure 2.11: The back side amplitude of the deflected probe beam in the transversal direction Eq. (2.31), Eq. (2.39) for the substrate having three different thickness. The amplitude decreases as the thickness of the substrate increases.

2.6 Conclusion

In this chapter, we have used PDS which is a contactless method to come up with the quantities necessary to measure thermal conductivity for the first time. Using different models constructed for measuring two-side PDS systems we managed to compute the amplitude and phase shift of the deflection angle for the PDS system. This will lead to the measurement of the thermal conductivity in such systems.

We devise two models to construct our measurements for the thin film-substrate system where the thin film is being illuminated by the pump beam and has a much higher thermal conductivity than the substrate. The first model is measuring the deflection angle of the probe beam being emitted along the *y*-direction for metallic thin films on a substrate. The major problem of this model is arriving with a constant phase shift for the front side deflection angle no matter what kind of thin film and substrate we use. For the second model, we measure the deflection angle of the probe beam being emitted along the *z*-direction. We write the theory for the front and back side of the PDS system for both when the probe beam is passing the surface area illuminated by the pump beam and when the probe beam doesn't pass the surface area illuminated by the pump beam. We compare the analytical results with the experimental measurements and find that they are in good co ordinance with one another.

We also devised a model for the thin film-substrate system where the substrate is being illuminated by the pump beam and has a much higher thermal conductivity than the thin film. We

37

illuminate the substrate from one side by a thin laser beam and divide the temperature profiles into symmetric and antisymmetric modes and write them in terms of a series of Fourier solutions with different eigenvalues. The eigenvalues depend on the width of the substrate L, the frequency of the chopper ω and the thermal diffusivity of the substrate itself D_b. By using Fermat's principle in optics we compute the deflection angle for the PDS system composed of different substrates. By having the deflection angle we can compute the amplitude and phase shift of the system which are the required values to measure the thermal conductivity.

2.7 Reference

[1]   Allan Rosencwaig, *Photoacoustic spectroscopy of solids*, University of British Columbia

[2]   T. Gotoh, S. Nonomura, S. Hirata, S. Nitta, *Photothermal bending spectroscopy and photothermal deflection spectroscopy of C_{60} thin films*, Department of Electronic and Computer Engineering, 1997

[3]   K. J. Blundell, and K. M. Blundell, *Concepts in Thermal Physics* (OUP), 1st ed

[4]   S.Ahmed Ph.D. Thesis, Western University, 2013

[5]   W. B. Jackson, N. M. Amer, A. C. Boccara, and D. Fournier, *Photothermal deflection spectroscopy and detection*, Appl. Optics, Vol. 20, Issue 8, pp. 1333-1344 (1981)

[6]   M.Terazima, J. Chem. Phys., 1996, 104, 4988-4998

[7]   M.S.Ahmed, S.Ezugwu, R.Divigalpitiya, and G.Fanchini, Carbon61 (2013) 595

[8]   S.Ezugwu, M.S.Ahmed, R.Bauld, R.Divigalpitiya, G.Fanchini, Thin Solid Films, 534 (2013) 520

[9]   Arfken Weber, *Mathematical Methods for Physics*, Sixth Edition, Elsevier Academic Press

[10]   P. L. Kapitza, Zh. Eksp. *Teor. Fiz.* 11, 1 (1941) (J. Phys. (USSR)4, 181, 1941); also in Collected Papers of P. L. Kapitza, Vol. 2, D. ter Haar, ed. (Pergamon, Oxford, 1965), p. 581.

[11]   E.T. Swartz, R.O. Pohl Rev. Mod. Phys., 61 (1989), pp. 605-668

[12]   Barrat, Jean-Louis, Chiaruttini, Molecular Physics, 2003, Volume 101, Issue 11

[13]   Deng, Chernatynskiy, J. Appl. Phys., 2014, Volume 115, Issue 8

[14]   M. L. Boas, *Mathematical Methods in the Physical Science* (John Wiley & Sons), 3rd ed

Chapter 3

Contactless scanning thermoreflectance imaging

3.1 Introduction

Determining and imaging the thermal properties at the nanoscale is a demanding experimental challenge. So far, virtually any techniques used to image nanoscale thermal properties require positioning the sample in contact with voluminous probes that act as undesirable thermal sinks and dramatically affect the measurements, in spite of poor interfacial thermal resistivity. Thermoreflectance, a contactless method in which the thermal conductivity is measured by probing the heat-induced changes in the optical properties of a sample, is extensively used for measuring the macroscopic and microscopic thermal properties of solids, but, so far, it has been limited by diffraction in its applicability at the nanoscale. Here, we present near-field scanning thermoreflectance imaging (NeSTRI), a new scanning probe technique in which an aperture-type near-field optical microscope at sub-wavelength resolution is used to determine the thermoreflectance of thin films in non-contact mode. As a case study, NeSTRI is here applied to multilayer graphene films on glass substrates. The thermal conductivity of micrometer-size multilayer graphene platelets is determined and is consistent with previous macroscopic predictions. We also find that the thermal conductivity is locally higher at specific crystallographic edges of multilayer graphene platelets, which is indicative of the spatial resolution of our method. NeSTRI is uniquely suited to understanding the thermal properties of a large class of nanostructured and nanoscale systems.

3.2 Near-field scanning thermoreflectance imaging

Modulated thermoreflectance[1-5] is a contactless technique commonly used to measure the thermal conductivity of solids, but is macroscopic in nature. With this technique, the sample is periodically heated at the surface, and heat transfers to air, or another fluid at the interface, which experiences periodic changes in density and refractive index due to the subsequent periodic

oscillations in temperature. The phase lag at which changes in the fluid refractive index occur depends on the thermal properties of the sample, which can thus be measured by means of a light beam. The use of light eliminates the necessity of physical contact between the sample and the probe. Thermoreflectance measurements are contactless and alleviate many of the thermal sinking problems commonly associated with other contact-based thermal measurements.

Micro-thermoreflectance was used to accurately map the thermal properties of micrometer-thick gold films[5]. However, differently, from scanning thermal microscopy (SThM), this technique suffers from inherent limitations in terms of lateral resolution. Light, the thermal probe used in thermoreflectance measurements, is limited by diffraction in its capability to characterize nanometer-size objects. Optical methods that are not diffraction-limited and combine the advantages of SThM and thermoreflectance will be vital to enable contactless thermal imaging at the nanoscale.

Scanning near-field optical microscopes (SNOM) are optical instruments that exploit the properties of evanescent waves generated by scattering of light in the proximity of a nanostructured sample to enable resolution beyond the diffraction limit[6]. SNOM measurements rely on the interaction of two distinct nanometer-size objects: a nanoscale feature in the illuminated sample and a nanometer-size probe. Apertureless SNOM utilizes nanoparticles as probes, while nanometer-size openings are used to detect the optical signal in aperture-type SNOM. With modern aperture-type instruments, the near-field optical signal is generated and detected by hollow scanning probe cantilevers and the sample topography is simultaneously scanned by atomic force microscopy (AFM). If visible light is used for SNOM experiments, the sample-probe distance can be extended up to several hundred nanometers during measurements[7], thus enabling SNOM imaging in non-contact mode, with negligible mechanical and thermal interaction between the cantilever and the sample.

Here, we demonstrate that an aperture-type SNOM system operating out of contact with the sample can be utilized to detect modulated thermoreflectance signals from a nanostructured thin film, thus enabling contactless thermal imaging with nanoscale resolution. Due to the combination of SThM and thermo-reflectance, the technique we are here introducing for the first time can be termed near-field scanning thermoreflectance imaging (NeSTRI). The implemented NeSTRI apparatus will include two distinct microscopes from which specimen under investigation can be illuminated: an inverted optical microscope from which the sample can be

uniformly irradiated and heated by an intense time-modulated "pump" laser, and an upright, aperture-type SNOM microscope, from which the surface irradiated from the inverted microscope can be scanned at sub-wavelength resolution by a low-intensity "probe" laser beam at different wavelength. In addition to illuminating the sample with the probe laser beam, the SNOM system will be used to collect the pump laser light that traverses the sample and to measure its intensity. In this way, the optical absorption coefficient of the sample can be locally determined. The SNOM instrument is complemented by a grazing-angle detector to collect and quantify the amount of "probe" laser light reflected by the sample. From the periodic modulation of the reflectivity of the probe beam, and its phase delay with respect to the modulation of the pump beam, the amplitude and phase of the temperature oscillations in the proximity of the sample can be determined.

Due to the flexibility of the NeSTRI apparatus, two distinct sets of images are obtained for each sample: (i) the heating profile H(x, y, t) locally generated in the sample from periodic illumination by the pump beam, and (ii) the amplitude $\delta\rho_0$ (x, y) and phase $\delta\varphi_0$(x, y) of periodic thermoreflectance oscillations experienced by the "probe" beam in the proximity of the periodically heated sample.

In this chapter by a combination of the above data sets, we solve the Fourier equation governing the diffusion of heat, and acquire thermal conductivity and heat capacity images, without any need of contacting the sample with a heat sink.

3.3 Experimental setup

The NeSTRI setup presented in this study has been implemented using a Witec Alpha 300S aperture-type AFM and SNOM system, equipped with hollow cantilever tips (SNOM-NC, NT-MDT Co.)[8-11]. Near-field optical response is obtained by illuminating the scanning near-field optical microscopes (SNOM) tip aperture through an upright confocal optical microscope. For reflection-mode SNOM imaging, evanescent waves locally generated at the tip aperture, and scattered by the sample, were collected at grazing angle by a subminiature accessory (SMA). For transmission mode SNOM, evanescent waves locally generated at the tip aperture and scattered through the sample were collected by an inverted optical microscope and conveyed to the photomultiplier tube. Combination of reflection and transmission SNOM images were acquired

with this assembly, shown in Figure 3.1(a), and provided maps of the sample absorbance, $A_0(x, y)$, via the relationship:

$$A_0(x, y) = 1 - \tau(x, y) - \rho(x, y), \qquad (3.1)$$

where $\tau(x, y)$ and $\rho(x, y)$ are, respectively, the transmittance and reflectance of the sample. Information on the absorbance, in conjunction with knowledge of the laser power P_0, was used to determine the sample heat profile upon uniform illumination. To record modulated thermoreflectance images, the setup is shown in Figure 3.1(b) was used with the tip lifted off from sample contact.
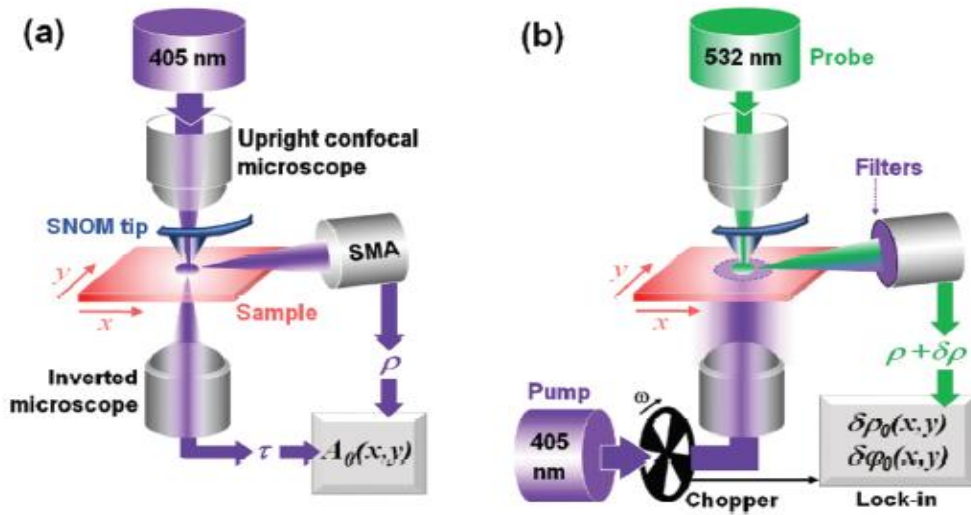
Figure 3.1: a) Setup used for transmission (τ) and reflection (ρ) SNOM images, from which $A_0(x, y)$, the sample absorbance can be obtained and used to determine the heat generation profile according to Eq. (3.2). b) NeSTRI setup used for thermoreflectance imaging in phase ($\delta\varphi_0$) and amplitude ($\delta\rho_0$). A 405 nm pump beam, modulated at frequency ω by a chopper, heats the sample over a large area from the inverted microscope. Heat, after diffusing along the thin film surface, is transferred to the air. Air changes in volume and thus experiences, at a certain phase, lag periodic changes in refractive index that induce small oscillations in reflectance at the air–sample interface. Such oscillations are probed, in amplitude and phase, by a 532 nm probe beam originating from the upright SNOM microscope and detected using a lock-in amplifier. A set of filters at the SMA coupler eliminates 405 nm light scattered from the pump beam.

Large sample areas are uniformly illuminated. The pump beam is intersected with a mechanical chopper operated at ω = (25-450) Hz angular frequencies. In this way, we obtain a pulsed "pump" beam that illuminates the sample and generates, at any time t, a periodic heat profile accordingly to:

$$H(x, y, t) = \frac{P_0 \cdot A_0(x, y)}{d(x, y)} \cdot \exp(i\omega t)$$
$$= H_0(x, y) \cdot \exp(i\omega t)$$
(3.2)

where $d(x, y)$ is the thickness of the absorbing film, and $H_0(x, y) \approx P_0 \cdot A_0(x, y)/d(x, y)$ represents the amount of heat locally deposited per sample unit volume. During pulsed heating from the pump beam, the sample surface was scanned in the near-field by evanescent light originating from a continuous "probe" laser beam with a significantly lower power than the pump beam. The amount of the probe beam evanescent radiation reflected at each point (x, y) of the surface was detected by the SNOM accessory. Upon heating, heat is transferred from the sample to air. Air decreases in volume and experiences a consequent decrease in refractive index. In thermoreflectance experiments, the change in refractive index of the sample is negligible over the change in refractive index of air, because thermal dilatation is significantly higher in gases than solids. The amplitude $\delta\rho_0(x,y)$ of thermoreflectance oscillations, experienced by the probe beam due to the periodic heating of air from sample heating, is proportional to the temperature oscillations at the sample surface. The phase lag $\delta\varphi_0(x, y)$ relative to the pump beam depends on the mean free path of the thermal waves reaching each point (x, y) from the surrounding region. The complex thermoreflectance at the sample surface is given by:

$$\delta\rho(x, y, t) = \delta\rho_0(x, y) \cdot \exp\{i[\omega t + \delta\varphi_0(x, y)]\}.$$
(3.3)

In NeSTRI, $\delta\rho_0(x, y)$ and $\delta\varphi_0(x, y)$ can be recorded independently at each point and phase and amplitude images of the complex thermoreflectance could thus be obtained.

3.4 Numerical model

The objective of our numerical model is to calculate the thermal conductivity $k_{th}(x, y)$ and volumetric specific heat $c(x, y)$ of inhomogeneous thin films from the quantities imaged by NeSTRI: the heat generation profile Eq. (3.2) and the amplitude and phase of the complex thermoreflectance at the sample surface Eq. (3.3). In our model, the substrate is assumed to be transparent and thermally insulating, a reliable assumption for our test samples and many other

thin films of practical interest. Our model requires the numerical solution of the inverse equation of heat[11] using a finite difference method.

Radiation from the pump beam is absorbed in different amounts at different locations of the thin film under investigation and heat locally generated by photons preferentially diffuses along the film surface, which leads to a thermal profile accordingly to the Fourier equation[11, 12]:

$$c(x, y)\frac{\partial T(x, y, t)}{\partial t} + \nabla \cdot \left[k_{th}(x, y)\nabla T(x, y, t)\right] = H(x, y, t). \tag{3.4}$$

Eq. (3.4) is reminiscent of the conservation of energy in a control region about point *(x, y)*, in which heat can be generated, transferred, and accumulated. It is worth noting that, in the present work, *T(x, y, t)* does not represent the absolute temperature, but corresponds to the temperature difference between the sample surface at point *(x, y)* and the environment.

In our experiments, *H(x, y, t)* is periodic with the same periodicity as the chopper frequency, as seen from Eq. (3.2). In this case, a solution of Eq. (3.4) can be written by considering that the temperature and thermoreflectance only carry the Fourier component oscillating at that specific frequency: $T(x, y, t) = T_0(x, y) \cdot exp\{i[\omega t + \delta\varphi_0(x, y)]\}$. Substitution of this solution into Eq. (3.4) leads to the following expression for the equation of heat written in the Fourier domain:

$$i\omega c(x, y)T_0(x, y)\exp\left[i\delta\varphi_0(x, y)\right] + \nabla\left\{k_{th}(x, y)\nabla[T_0(x, y)\exp\left\{i\delta\varphi_0(x, y)\right\}]\right\} = H_0(x, y). \tag{3.5}$$

Eq. (3.5) has two components, real and imaginary, and their physical meaning is associated to the finite thermal diffusivity at which heat propagates along the thin film surface, due to nonzero lateral thermal diffusion length.

Eq. (3.4) and (3.5) indicate that, for any given profile of heat generation, *H(x, y, t)* depends on the thermal conductivity and heat capacity at any other points on the thin film surface. In our case, *H(x, y, t)* is given by Eq. (3.2). At very short lateral thermal diffusion lengths, heat is released to air close to the point *(x', y')* at which it is generated, *T(x, y, t)* only depends on the value of *H(x', y', t)* at points situated in the very proximity of *(x, y)*, and Eq. (3.5) is real, with *δφ₀(x, y) ≈ 0*. Conversely, at large thermal diffusion lengths, heat travels relatively long distances along the surface, before being released to the air. In this way, relatively large heated domains will contribute to *T(x, y, t)*, and Eq. (3.5) will be predominantly imaginary, with *δφ₀(x, y)* closer to 90°. As the lateral thermal diffusion length along the surface is inversely

proportional to the pump beam frequency, NeSTRI measurements at varying ω, leading to different phase lags, are needed to exhaustively understand the film thermal properties.

As will be shown in the next chapter a linear relation exists between $T_0(x,y)$ and the thermoreflectance:

$$\delta\rho_0(x,y) = hT_0(x,y),\tag{3.6}$$

where h, a negative proportionality coefficient, is independent of x, y and ω. It is convenient to write Eq. (3.5) in terms of $\delta\rho_0(x,y)$ instead of $T_0(x,y)$ because this is the quantity actually measured by NeSTRI. By replacing Eq. (3.6) into Eq. (3.5), we can write a complex equation in the Fourier domain, which links the phase and amplitude of the complex thermoreflectance with the specific heat and thermal conductivity at any generic point of the thin film:

$$i\omega c(x,y)\delta\rho_0(x,y)\exp\{i\delta\varphi_0(x,y)\} + \nabla\{k_{th}(x,y)\nabla[\delta\rho_0(x,y)\exp\{i\delta\varphi_0(x,y)\}]\} = hH_0(x,y)$$
$$.\tag{3.7}$$

The physical meaning of the real and imaginary parts of Eq. (3.7) is the same as in the corresponding components of Eq. (3.5). The two components can be separately equated leading to the following identities:

$$\nabla k(x,y)\cdot\nabla\delta\rho_0(x,y) + k_{th}(x,y)\nabla^2\delta\rho_0(x,y) - k_{th}(x,y)\delta\rho_0(x,y)[\nabla\delta\varphi_0(x,y)]^2 = hH_0(x,y)\cos\delta\varphi_0(x,y),$$
$$\tag{3.8}$$

for the real part, and

$$\omega c(x,y)\delta\rho_0(x,y) + k_{th}(x,y)[\delta\rho_0(x,y)\nabla^2\delta\varphi_0(x,y) + 2\nabla\delta\rho_0(x,y)\cdot\nabla\delta\varphi_0(x,y)]$$
$$+ [\nabla k_{th}(x,y)\cdot\nabla\delta\varphi_0(x,y)]\delta\rho_0(x,y) = -hH_0(x,y)\sin\delta\varphi_0(x,y)\tag{3.9}$$

for the imaginary part. The solution of the real equation Eq. (3.8) provides $k_{th}(x,y)$, a map of the thermal conductivity of the thin film, which can then be replaced into Eq. (3.9). $c(x,y)$ can thus be explicitated. In this way, the solution of the imaginary equation Eq. (3. 9) provides a map of the film heat capacity.

Due to the nonanalytic nature of $\delta\rho_0(x,y)$, $\delta\varphi_0(x,y)$ and $H_0(x,y)$, the known quantities recorded by NeSTRI experiments, the solution of Eq. (3.8) must be obtained numerically, using a finite difference method. The generality of this solution makes it suitable to analyze a large variety of thin films measured by NeSTRI. The numerical computer routine used to solve Eq. (3.8) is described in detail in chapter 4. Boundary conditions for the numerical problem are the known values of $k_{th}(x_b,y_b)$ at $(x,y) = (x_b,y_b)$, the boundaries of the NeSTRI image, at which the

45

surface is made of glass and the thermal conductivity is known. In the specific case of our test samples, the thermal conductivity of glass was set at $k_{th}(x_b,y_b)$ = 1.1 W/m/K[13]. The quantity $k_{th}(x,y)/h$ can be extracted from the numerical solution of Eq. (3.8), and represents the thermal conductivity in specific arbitrary units that depend on the geometry of the used SNOM tip and its distance from the surface, via the proportionality coefficient of Eq. (3.6). Due to the difficulty to estimate the tip-sample distance, the actual value of h involved in the right-hand term of Eq. (3.8) needs to be determined experimentally. This can be done via Eq. (3.9) because the heat capacity of glass, $c(x_b,y_b)$ = 860 J/Kg/K, is also known[14]. In this way, the solution of Eq. (3.8) and (3.9) was implemented using a Matlab[TM] routine and leads to the determination of $k_{th}(x,y)$ and $c(x,y)$.

3.5 Sample absorbance

Although sample illumination from the pump beam is uniform, the value of $H(x,y,t)$ at a specific point also depends on the local value of the absorbance. Specifically, $H(x,y,t) = 0$ at any points on bare glass, at which $A_0(x,y) = 0$, while is more significant, up to 0.09 mW/μm^2, at points on relatively thick multilayer graphene. The result of these measurements is presented in Figures 3.2(a-c) that show, respectively, AFM topography, transmittance and reflectance images of the test sample.

Figure 3.2(d) shows the variation of $A_0(x,y)$ in multilayer graphene platelets as a function of the number of graphene layers. From the transmittance image shown in Figure 3.2(b), it can be observed that the glass substrate is always significantly more transmitting than multilayer graphene. On the other hand, from Figure 3.2(c), it can be noticed that the reflectance of glass and graphene are both relatively small and comparable, except at a few locations in which graphene flakes are particularly wrinkled and rich in ridges, and become highly reflecting with ρ up to 30%. There is a wide range of thicknesses and number of layers in the platelets shown in Figure 3.2. The average optical absorbance could be determined for different selected regions and is plotted in Figure 3.2(d).
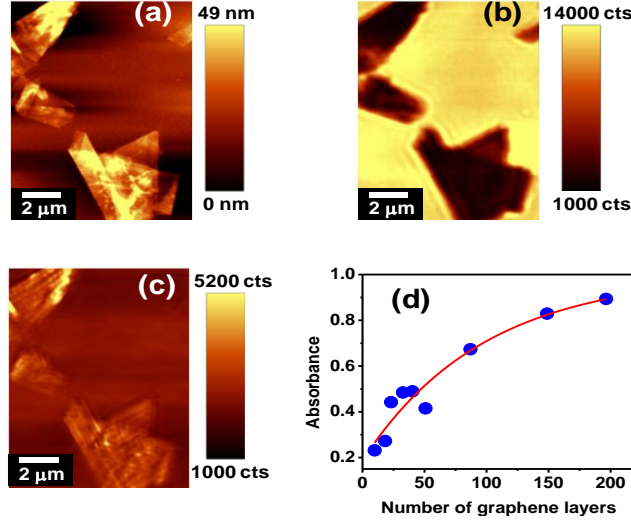
Figure 3.2: a) Topography, b) Transmission and c) Reflection SNOM images of the test sample. The shown topography was obtained during SNOM transmission-mode measurements. d) Absorbance vs. number of graphene layers. Thick platelets are relatively absorbing, while thinner platelets are more transparent. Fringes that can be observed in panel b are due to effects from edge modes of graphene flakes.

Figure 3.2(d) shows that $A_0(x,y)$ increases with increasing number of layers, consistently with previous macroscopic observations that showed absorbance increase according to the Beer-Lambert law, $A_0 \sim 1 - \exp(N/M)$ ($M \approx 50$) in multilayer graphene platelets[15]. We can thus infer that this relationship is valid at the nanoscale level. These results indicate that graphene platelets with less than 50 layers are locally transparent, with relatively low heat load applied to them. Darker areas in the SNOM transmittance image in Figure 3.2(b) are highly absorbing and will be affected by high thermal load. Due to such different levels of heat generated at each point of the sample, knowledge of optical absorbance, calculated from Eq. (3.2), will be critical for quantitative estimates of the thermal conductivity and thermal capacity of the test sample, as described in the next section.

3.6 Multi-frequency NeSTRI imaging
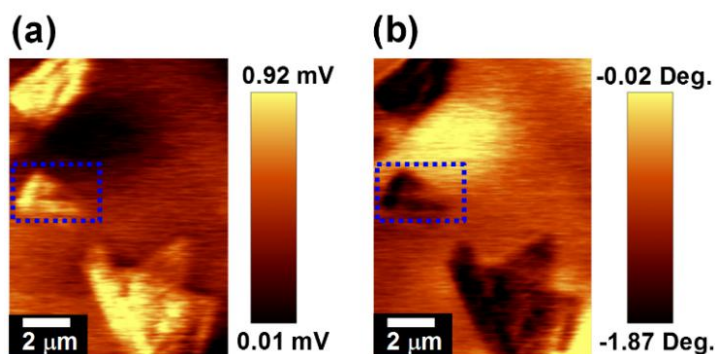
Figure 3.3: a) NeSTRI amplitude and b) phase images recorded at 75 Hz pump beam modulation frequency in non-contact from the test sample. Dotted squares highlight the detail that is further investigated. Negative phase is a consequence of h < 0 in Eq. (3.6) and is a strong indication of the fact that images are from genuine complex thermoreflectance signals. An excellent correlation between NeSTRI images in the present figure and the corresponding contact AFM and SNOM images from the figure (3.2) can be observed.

Figure 3.3 shows the NeSTRI images, amplitude, and phase, of the test sample, recorded at $\omega = 75$ Hz. A close correlation between these images, recorded in non-contact from the sample, and the corresponding SNOM and topography images, recorded in contact mode and reported in Figure 3.2, can be observed. The thermal diffusion length along the surface decreases as the pump beam modulation frequency increases. Therefore, thermoreflectance measurements at different values of ω lead to different amplitude and phase lags, and decrease the arbitrariness in the determination of the thermal properties[1-5]. Figure (3.4) shows multifrequency NeSTRI measurements on a detail of Figure (3.3). It shows the AFM topography Figure 3.4(a) SNOM reflectance Figure 3.4(b) and thermal amplitude and phase of the temperature profile for two different modulation frequencies of the pump beam.
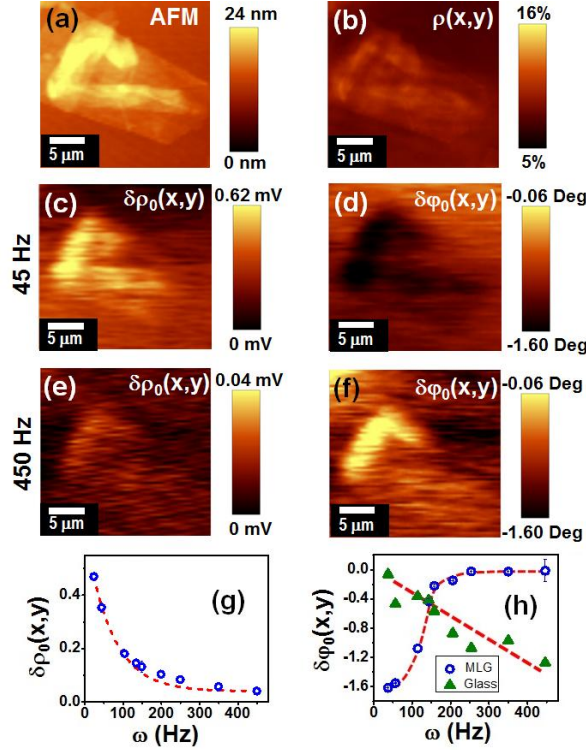
Figure 3.4: a) Detail of AFM and b) SNOM reflectance images of multilayer graphene flake from Figure (3.2). c) Multifrequency NeSTRI experiments: thermoreflectance amplitude and d) phase at ω = 45 Hz frequency and e) thermoreflectance amplitude and (f) phase at ω = 450 Hz. It is always observed $\delta\varphi_0(x,y) < 0$, as a consequence of h < 0 in Eq. (3.6) because $\delta\rho(x,y,t)$ and T(x,y,t) are in 180° phase opposition. g) The amplitude monotonically decreases as ω increases due to shorter thermal diffusion length at increasing frequency. h) Phase in multilayer graphene (MLG) increases from about -1.6° to nearly zero and, from comparison of panels d and f, it is evident that $\delta\varphi_0$ is lower in graphene than glass at 25 Hz, while, at 450 Hz, it is lower in glass than graphene.

Panels (c) (ω = 45 Hz) and (e) (ω = 450 Hz) in Figure (3.4) show that the thermoreflectance amplitude is significantly different between thin and thick regions of the flake on the one hand, and between graphene and the glass substrate on the other hand. When the changes in the reflectivity are larger due to stronger heat dissipation, the measured amplitude is higher, which leads to bright features in the amplitude images. In general, the magnitude of the amplitude always tends to monotonically decrease as ω

49

increases, due to shorter thermal diffusion length at increasing frequency, as demonstrated in panel (g). The thermal diffusion length[11] can be defined as:

$$L_{th} \approx (D/\omega)^{1/2}, \tag{3.10}$$

where $D(x,y) = k_{th}(x,y)/c(x,y)$ is the local thermal diffusivity of the sample, and the amplitude of the thermoreflectance signal is controlled by the thermal diffusion length.
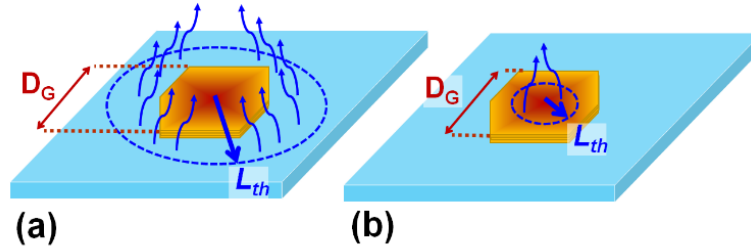
Figure 3.5: a) Large thermal diffusion length (L_{th}) at low frequency, dominated by the diameter (D_G) of graphene flake, with heat dissipation mainly occurring in the glass, and b) Low thermal diffusion length at high frequency, in which Eq. (3.10) holds and heat dissipation mainly occurs in graphene. A smaller phase lag occurs from the medium from which the largest amount of heat is dissipated to air.

While the amplitude is always decreasing at increasing ω, phase images exhibit a more intriguing trend that also depends on the specific sample location. Panels (d) and (f) of Figure 3.4 show NeSTRI phase images at 45 Hz and 450 Hz, respectively. It is immediate that in panel (d), at low frequency, the graphene flake exhibits a larger phase lag than glass. Conversely, in panel (f), at high frequency, the glass substrate exhibits a larger phase lag than graphene. It is worthwhile noting that heat generation only occurs in graphene because glass is optically non-absorbing. Instead, thermal dissipation may occur either from glass, which possesses a very short thermal diffusion length regardless of the used pump beam frequency, or graphene where the thermal diffusion length is significantly higher, up to several μm[16] and is determined by Eq. (3.10). At low frequencies, the thermal diffusion length in graphene is larger than the size of the flake probed in Figure 3.5 (i.e. about 10 μm). Thus, the heat generated within the graphene sample is transferred in significant amounts to glass and a more significant phase lag is observed in graphene than glass, as demonstrated in Figure 3.5(a). Conversely, at high frequencies, L_{th} is shorter than the flake size and heat generated in graphene is mostly

50

dissipated within the same flake and minimally transferred to glass, as demonstrated in Figure 3.5(b). The crossover between the high frequency and low frequency conditions can be estimated from Figure 3.4(f), to corresponds to about $\omega = 150$ Hz. From these considerations, it is evident that multifrequency NeSTRI will be a very powerful and effective technique to visualize the thermal diffusivity and thermal diffusion length in layered materials.

3.7 Recognition of potential NeSTRI artefacts

When developing a new scanning probe technique, it is imperative to recognize and avoid any possible measurement artefacts. In NeSTRI, they could be either mechanical artefacts, typical of AFM and caused by the non-ideal interaction of the tip with the sample, or optical artefacts associated with SNOM measurements. Specifically, it is worthwhile noting that the SNOM signal intensity is strongly affected by the interference between light scattered from the tip and the specular image of the sample, which provides an oscillatory dependence of the optical signal on the distance between the tip and the sample surface[7, 17-19]. In order to prevent NeSTRI artefacts associated to such oscillations, we anticipate it is vital to perform SNOM and NeSTRI scans at a tip-sample distance z corresponding to the first maximum of the optical signal[7], z_0. In this way, small distance fluctuations δz around z_0 will produce minima of the intensity of the SNOM signal both at $z_0-\delta z$ and $z_0+\delta z$. As demonstrated in Figure 3.6, oscillations of z at the same frequency of the pump pulses, will only produce intensity modulations of the NeSTRI signal at double frequency, 2ω, which do not affect the measurements, as the detector response is locked-in at the chopper angular velocity.

Avoiding the detection of SNOM artefacts associated to periodic tip-sample distance oscillations is particularly critical in NeSTRI. Intense heating may produce non-negligible and periodic thermal dilatation of the sample and, indeed, periodic modulations at the same frequency. We ruled out that such $z(\omega)$-oscillations significantly affect our NeSTRI scans by measuring a set of uniform aluminum films at different thicknesses, from 20 nm to 80 nm, as shown in Appendix II.
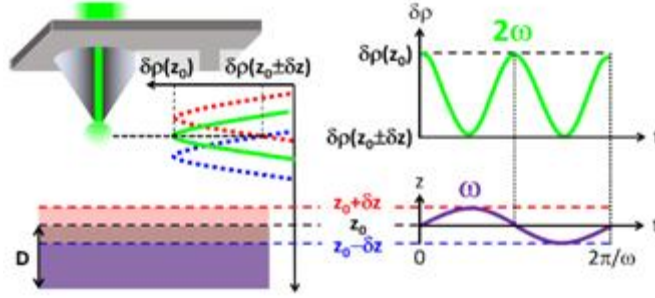
Figure 3.6: Demonstration of the mechanism for which, in case of tip-sample distance oscillations due to thermal dilatation of the sample, the NeSTRI signal at frequency ω is unaffected by near-field artefacts, because signal intensity fluctuations δρ(z₀±δz) < δρ(z₀) only occur at double-frequency 2ω.

If *z(ω)*-oscillations led to critical thermal-dilatation related artefacts, the signal amplitude of uniform Al thin films would increase at increasing thickness. In contrast, genuine NeSTRI scans result in a signal decrease for thicker Al layers, because, at larger thicknesses, heat is generated within a larger sample cross-section, which also results in lower surface temperatures (see Appendix II for quantitative details). Figure II.1 in the appendix clearly shows that the NeSTRI signal amplitude of uniform Al films decreases with their thickness, in good quantitative agreement (see Figure II.2) with a model that assumes a decreasing amount of volumetric heat generation in thicker films, due to stronger attenuation of the pump beam along their larger cross section. This is a strong indication of the genuineness of our NeSTRI measurements and corroborates the hypothesis that, when carefully performed, NeSTRI is insensitive to periodic, thermally induced, dilation and contraction of solid samples at their surface.

3.8 Conclusion

In this chapter, we introduced NeSTRI, a scanning near-field-based thermoreflectance imaging technique capable of mapping the thermal properties of thin solid films at the nanoscale. From NeSTRI measurements, the phase shift and amplitude of the sample thermoreflectance can be imaged and the sample optical absorbance and topography can be independently probed using SNOM measurements in contact with the sample. By analyzing the absorbance of our samples we found that thinner samples are more

transparent with respect to thick samples. Also by analyzing the phase shift and amplitude in different frequencies we observed that the amplitude and phase shift of the graphene flake decreases as we increase the frequency while the phase shift in the multilayer glass increases. In the end, we studied the role of artefacts in NeSTRI measurements and concluded that when NeSTRI measurements are carefully performed, they are insensitive to periodic, thermally induced dilation and contraction of solid samples at their surface.

3.9 References

[1]   L. J. Inglehart, A. Broniatowski, D. Fournier, A. C. Boccara, and F. Lepoutre, Appl. Phys. Lett., 1990, 56, 1749

[2]   L. Pottier, Appl. Phys. Lett., 1994, 64, 1618

[3]   B. Li, L. Pottier, J. P. Roger, and D. Fournier. AIP Conf. Proc., 1999, 463, 336

[4]   A. J. Schmidt, R. Cheaito, and M. Chiesa, Rev. Sci. Instrum., 2009, 80, 94901

[5]   G. Langer, J. Hartmann and M. Reichling, Rev. Sci. Instrum., 1997, 68(3), 1510

[6]   E. Betzig and J. K. Trautman, Science, 1992, 257, 189

[7]   S. Ezugwu, H. Ye, and G. Fanchini, Nanoscale, 2015, 7, 252

[8]   A. A. Balandin, Nature Materials, 2011, 10, 569

[9]   G. Eda, G. Fanchini, and M. Chhowalla, Nature Nanotech, 2008, 3, 270

[10]   Z. Wu, Z. Chen, X. Du, J. M. Logan, J. Sippel, M. Nikolou, K. Kamaras, J. R. Reynolds, D. B. Tanner, A. F. Hebard, and A. G. Rinzler. Science, 2004, 305, 1273

[11]   H. S. Carslaw and J. C. Jaeger, *Conduction of Heat in Solids* (2nd ed.), Oxford University Press, London 1959

[12]   N. W. Ashcroft and D. N. Mermin, *Solid State Physics*, Saunders College, Philadelphia, 1976

[13]   M. J. Assael, S. Botsios, K. Gialou, and I. N. Metaxa, International Journal of Thermophysics, 2005, 26, 1595

[14]   H. R. Philipp, in *Handbook of optical constants of solids* (E.D. Palik Ed.), Vol. 1, Academic Press, New York, 1985

[15]   M. S. Ahmed, S. Ezugwu, R. Divigalpitiya, and G. Fanchini, Carbon, 2013, 61, 595

[16]   D. L. Nika, S. Ghosh, E. P. Pokatilov, and A. A. Balandin, Appl. Phys. Lett., 2009, 94, 151911

[17]   U. T. During, D. W. Pohl, and F. Rohner, J. Appl. Phys., 1986, 59, 3318

[18]   P. G. Gucciardi and M. Colocci, Appl. Phys. Lett., 2001, 79, 1543-1545

[19]   S. I. Bozhevolnyi, J. Opt. Soc. Am. B, 1997, 14, 2254-2259

Chapter 4

Numerical solution of the Fourier's heat equation for the near-field scanning thermoreflectance imaging technique

4.1 Introduction

In the previous chapter, we presented near-field scanning thermoreflectance imaging (NeSTRI), a new non-contact scanning probe technique for acquiring thermal images at the nanoscale. Due to the nonanalytic nature of the known quantities recorded by NeSTRI which are the thermoreflectance amplitude and the amount of heat locally deposited per sample unit volume, Eq. (3.8) must be obtained numerically, using a finite difference method[7, 8]. In this chapter, we give a detailed proof of how the calculations are done to solve the Fourier's heat equation and acquire the thermal conductivity and heat capacity maps. We use Rayleigh's law[1] to obtain a relationship between the thermoreflectance amplitude and surface temperature. We then develop a finite difference method to generate the thermal conductivity images.

4.2 Linear relationship between thermoreflectance amplitude and surface temperature

4.2.1 Reflectance due to light scattering at the tip aperture

Here, we offer a proof of the existence of a direct proportionality between the amplitude of the thermoreflectance signal $\delta\rho_0(x,y)$, measured by near-field scanning thermoreflectance imaging (NeSTRI), and $T_0(x,y)$, the temperature at the sample surface, which is expressed by Eq. (3.6). The validity of Eq. (3. 6) is essential to infer $T_0(x,y)$ from NeSTRI measurements. In our proof, we will assume the validity of Rayleigh's assumptions[1] for electromagnetic radiation scattered at the aperture of the scanning near-field optical microscope (SNOM) tip. Rayleigh's law is valid for scattering by objects with individual dimensions that are small compared with the wavelength of incident radiation. We assume that incident oscillating electric and magnetic fields induce

electric and magnetic multipoles at the boundaries of the tip aperture, which oscillate in phase with the incident electromagnetic wave and radiate energy in different directions. Furthermore, the tip apertures used in our SNOM and NeSTRI experiments are coated with non-ferromagnetic metals, in which electric dipoles are more significant than magnetic dipoles, so our proof will only deal with electric dipoles. As far as the wavelength is long compared to the size of the aperture, only multipoles of the lowest order, electric dipoles, are important.

The geometry we utilize for our proof, which is a good approximation of our experimental setup, is shown in Figure 4.1. Incident radiation is a plane monochromatic wave at wavenumber k and wavelength $\lambda = 2\pi/k$, with the direction of incidence defined by the unit vector $\mathbf{n_0}$, and complex incident polarization vector $\mathbf{e_0}$. It impinges an aperture of radius a bored in a relatively flat SNOM cantilever of thickness L. The associated incident electric field of intensity E_0 can be expressed as

$$\mathbf{E}_{inc} = \mathbf{e_0} \mathbf{E}_0 e^{ik\mathbf{n_0}\cdot\mathbf{x}} . \tag{4.1}$$

$\mathbf{E}_{inc}$ induces electric dipoles moments $\mathbf{p}$ and magnetic dipole moments $\mathbf{\mu}$ on the cylindrical surface of the SNOM tip aperture, which acts as a scatterer. Dipoles radiate energy at any generic directions indicated by unit vectors $\mathbf{n}$ and polarization vectors $\mathbf{e}$. Far away from the aperture, the intensity of the scattered field along a generic direction is given by[1]:

$$\mathbf{E}_{sc}^{(\mathbf{n})} = \frac{1}{4\pi\varepsilon_0} k^2 \frac{e^{ikr}}{r} \left[(\mathbf{n} \times \mathbf{p}) \times \mathbf{n} - \mathbf{n} \times \mathbf{\mu}/c \right] \approx \frac{1}{4\pi\varepsilon_0} k^2 \frac{e^{ikr}}{r} (\mathbf{n} \times \mathbf{p}) \times \mathbf{n} , \tag{4.2}$$

where r is the distance between the tip aperture and the observer, c is the speed of light and ε_0 is the dielectric permittivity in the air, which is relatively close to that of vacuum. We neglect the second addend in Eq. (4.2) since our SNOM tips are non-ferromagnetic and $|\mathbf{\mu}|/c << |\mathbf{p}|$.

$$E_{inc} = e_0 E_0 e^{ikn_0 \cdot x}$$
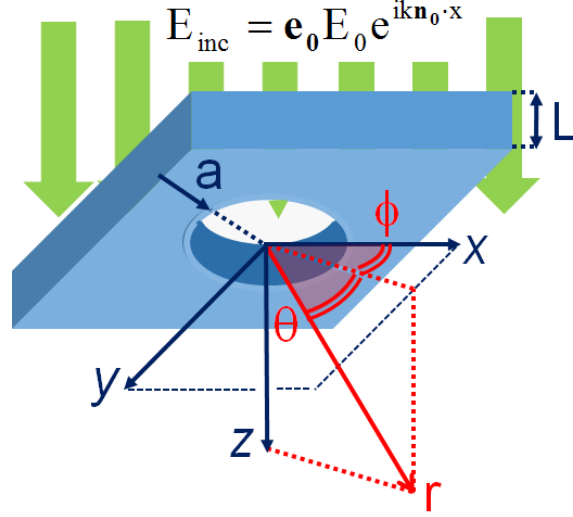
Figure 4.1: Small circular SNOM tip aperture of radius a and thickness L (a and L $<< \lambda =$ k/2π) drilled in a dielectric and non-ferromagnetic material and acting as a scatterer for plane and incident electromagnetic waves. The observer is positioned at a distance r and angle θ from the aperture.

Because the intensity of electromagnetic radiation is proportional to the square of the electric field, the amount of reflected light at any given direction is given by

$$\rho^{(n)} = \frac{\left| E_{sc}^{(n)} \right|^2}{\left| E_{inc} \right|^2}. \tag{4.3}$$

To calculate the reflectance, the scattered and incident electric fields given by Eq. (4.1) and (4.2) must be replaced into Eq. (4.3). In addition, it must be considered that the magnitude of the electric dipoles at the surface depend on the intensity of the incident electric field. Thus we have $|p| \sim E_0$, with a proportionality coefficient that also depends on the complex dielectric constant (or complex refractive index) of the tip material. Finally, scattering contributions at point r from all of the induced electrical dipoles at the scatterer surface must be superimposed by means of integration. For solving this scattering problem in an arbitrary geometry, it is convenient to decompose the two field vectors into components that are, respectively, parallel ($E_{//sc}^{(n)}$ and $E_{//inc}$) and perpendicular ($E_{\perp sc}^{(n)}$ and $E_{\perp inc}$) to n_0, and write them in a matrix form[2]. Eq. (4.2) can thus be generalized as:

$$\begin{bmatrix} E_{//sc}^{(n)} \\ E_{\perp sc}^{(n)} \end{bmatrix} = \frac{e^{ik(r-z)}}{-ikr} \cdot \mathbf{S} \cdot \begin{bmatrix} E_{//inc} \\ E_{\perp inc} \end{bmatrix}. \tag{4.4}$$

In our particular cylindrical geometry, $\mathbf{S}$, the scattering matrix, can be expressed as[2]:

$$\mathbf{S} = \frac{3ik^3}{4\pi} \cdot \left| \frac{m^2-1}{m^2+2} \right| \cdot V \cdot f(\theta,\phi) \cdot \begin{bmatrix} \cos\theta & 0 \\ 0 & 1 \end{bmatrix}. \tag{4.5}$$

This expression depends on the volume of the cylindrical aperture, $V = \pi a^2 L$, and on the form factor f, which is a consequence of the superimposition of the contributions from all of the dielectric dipoles in the particular geometry under consideration. For a cylinder, the form factor can be calculated as:

$$f(\theta,\phi) = \frac{1}{\pi L a^2} \int_{-\frac{L}{2}}^{\frac{L}{2}} dz \int_0^{2\pi} d\phi \int_0^a dr \cdot r \cdot \exp\left(\frac{2\pi i}{L} r \cos\theta\right), \tag{4.6}$$

from which it can be seen that $f(\theta,\phi) \approx -2$ in the long wavelength approximation, at a $<< \lambda$. Equation (4.5) also depends on the complex refractive indices of the two media, air, and the tip material, through the factor $|(m^2-1)/(m^2+2)|$ that is reminiscent of the proportionality factor between p and E_0 offered by Clausius-Mossotti relationship[3]. Also, in Eq. (4.5) m is the optical contrast coefficient

$$m = \frac{M_a}{M_t} \approx \frac{N_a}{N_t + iK_t}, \tag{4.7}$$

that represents the ratio between the complex refractive index of the tip material ($M_t = N_t + iK_t$) and air, for which $M_a \approx N_a \sim 1$. In the specific geometry used for NeSTRI and SNOM measurements, the SMA coupler used to collect the reflected light is placed at the same z-axis level of the tip and therefore, at $\theta = 90^o$. In these conditions, and for $f(\theta,\phi) \approx -2$, Eq. (4.4) and (4.5) lead to the relationship:

$$E_{sc}^2 = \frac{3}{2} \left| \frac{m^2-1}{m^2+2} \right| L^2 a^4 \frac{e^{2ikr}}{r^2} k^4 E_{inc}^2, \tag{4.8}$$

and, for $\langle \exp(2ikr) \rangle \approx \frac{1}{2}$, to the following expression of the reflectance at $\theta = 90^o$:

$$\rho = 12\pi^4 \frac{L^2 a^4}{r^2 \lambda^4} \cdot \left| \frac{m^2-1}{m^2+2} \right|. \tag{4.9}$$

58

The λ^4 dependence of Eq. (4.9) on the wavelength of the probe beam is reminiscent of a similar dependence in Rayleigh scattering[1], and is indicative of the fact that Rayleigh's law and Eq. (4.9) are derived under the same assumptions.

4.2.2 Amplitude of the thermoreflectance signal

In thermoreflectance measurements, the reflection coefficient determined via Eq. (4.9) changes with the temperature of air due to the temperature dependence of m. When light heats the sample, heat is transferred to air that decreases in density, and its refractive index decreases accordingly, as:

$$N_a(T) = N_a(0) - \chi T, \tag{4.10}$$

where $N_a(0) \approx 1$ is the refractive index of air under ambient conditions, in the absence of transferred heat, and $\chi \approx 6 \cdot 10^{-4}$ K^{-1} is the air thermo-optical coefficient[4]. It is worthwhile noting that, although χ is quite small, it has been demonstrated by several experiments in the literature to be sufficient to perform thermoreflectance measurements at the microscopic levels even with powers that are significantly lower than those used in our experiments[5]. In order to estimate how Eq. (4.10) affects the reflectance determined via Eq. (4.9), we consider that $N_t^2 \ll K_t^2$ for nontransparent tip materials such as, in our experiments, aluminum (for which $M_t = N_t + iK_t = 0.90 + i6.21$ at $\lambda = 532$ nm probe beam wavelength[6]). Thus, we can write:

$$m(T)^2 \approx \frac{\left(N_a(0) - \chi T\right)^2}{\left(N_t + iK_t\right)^2} \approx -\frac{1 - 2\chi T}{K_t^2}. \tag{4.11}$$

From this expression, by expanding the Clausius-Mossotti factor in Taylor series for sufficiently small values of m [i.e. $(m^2 - 1) / (m^2 + 2) \approx -\frac{1}{2} + \frac{3}{4} m^2$] and by substituting it into Eq. (4.9), we obtain the following expression for the temperature-dependent reflectance at the tip-air interface:

$$\rho(T) = \rho(0) + \delta\rho(T) \approx 12\pi^4 \frac{L^2 a^4}{r^2 \lambda^4} \left(\frac{1}{2} - \frac{2\chi}{K_t^2} T \right). \tag{4.12}$$

It is thus demonstrated that, under our specific assumptions, the thermoreflectance at the sample surface is given by:

$$\delta\rho_0(x, y) \approx -24\pi^4 \frac{L^2 a^4}{r^2 \lambda^4} \frac{\chi}{K_t^2} T_0(x, y), \tag{4.13}$$

Thus, from our derivation, the proportionality coefficient between $\delta\rho_0(x,y)$ and $T_0(x,y)$, which we introduced in Eq. (4.7), can be estimated as:

$$h = -24\pi^4 L^2 a^4 \chi \,/\, (r^2 \lambda^4 K_t^2). \qquad (4.14)$$

In Eq. (4.14), h does not depend on the specific location of the sample at which the thermoreflectance is measured. It only depends on the radius and length of the tip aperture, the optical properties of the system, the probe beam wavelength, and the distance between the sample and the detector. Consequently, due to the generality of our derivation which does not assume any significant tip-sample interaction, it remains demonstrated that the amplitude of the thermoreflectance signal measured by NeSTRI is linearly proportional to the temperature at the sample surface. It is worthwhile noting, from Eq. (4.14), that $h < 0$. Consequently, the thermoreflectance is lower at the times and locations at which the temperature is locally higher and the phases of $T_0(x,y)$ and $\delta\rho_0(x,y)$ are shifted by 180°. Therefore, the two quantities are in phase opposition.

4.3 Finite-difference method used to generate thermal conductivity images

4.3.1 Formulation of equations (3.8) and (3.9) in terms of finite differences

In this section, we develop a numerical algorithm capable of modeling, from phase $[\delta\varphi_0(x,y)]$ and amplitude $[\delta\rho_0(x,y)]$ thermoreflectance images, the diffusion of heat along an inhomogeneous thermally conducting thin film on a thermally insulating substrate. Objective of the algorithm is to reconstruct, from thermoreflectance phase and amplitude images, the thermal conductivity $k_{th}(x,y)$ that inhomogeneously varies from point to point of the film. We write Eq. (3.8) as:

$$\nabla k_{th}(x,y) \cdot \nabla \delta\rho_0(x,y) + k_{th}(x,y)\nabla^2 \delta\rho_0(x,y) - k(x,y)\delta\rho_0(x,y)[\nabla\delta\varphi_0(x,y)]^2 = hP_0 A_0(x,y)\cos[\delta\varphi_0(x,y)] \qquad (4.15)$$

Eq. (4.15) represents the real part of Fourier equation for periodic and inhomogeneous heat generation in a sample of optical absorbance $A_0(x,y)$. A pump laser at uniform power density P_0 impinges the imaged sample area, and heat is locally generated proportionally to the amount of power being locally absorbed by the thin film. In our experiments, the substrate is optically non-

absorbing. Both P_0 and $A_0(x,y)$ are known from independent experiments. The thermal conductivity $k_{th}(x,y)$ is unknown, and so is h, the proportionality coefficient given by Eq. (4.14) that is independent of x and y. Due to the arbitrary and nonanalytical nature of $A_0(x,y)$, $\delta\varphi_0(x,y)$ and $\delta\rho_0(x,y)$, Eq. (4.15) is a 2D first-order equation in $k_{th}(x,y)$ which needs to be solved numerically.

To solve Eq. (4.15), we here introduce a first-order, finite-difference method, in which the differential equation of an image of P×Q pixels, will be transformed into an algebraic system of P×Q linear equations in the same number of scalar unknowns. We write Eq. (4.15) in a way that each differential term, known or unknown is expressed by a finite difference (FD). The following known FD terms are calculated (for i = 1…P and j = 1… Q) from the thermoreflectance amplitude image [$\delta\rho_0(i,j)$]:

$$\nabla\delta\rho_0(x, y) \approx U_{i,j}\hat{\mathbf{i}} + V_{i,j}\hat{\mathbf{j}} = \frac{\delta\rho_0(i \pm 1, j)\text{-}\delta\rho_0(i, j)}{\delta x}\hat{\mathbf{i}} + \frac{\delta\rho_0(i, j \pm 1)\text{-}\delta\rho_0(i, j)}{\delta y}\hat{\mathbf{j}}, \tag{4.16}$$

$$\nabla^2\delta\rho_0(x, y) \approx \frac{U_{i\pm1,j}\text{-}U_{i,j}}{\delta x} + \frac{V_{i,j\pm1}\text{-}V_{i,j}}{\delta y}, \tag{4.17}$$

where $U_{i,j}$ and $V_{i,j}$ are the two scalar components of the thermoreflectance gradient and $\mathbf{i}$ and $\mathbf{j}$ represent two unit vectors along coordinate directions x and y, respectively. The following known FD term is calculated from both the thermoreflectance phase [$\delta\varphi_0(i,j)$] and amplitude images:

$$\delta\rho_0(x, y)[\nabla\delta\varphi_0(x, y)]^2 \approx Z_{i,j} = \delta\rho_0(i, j)\left\{\frac{[\delta\varphi_0(i \pm 1, j)\text{-}\delta\varphi_0(i, j)]^2}{\delta x^2} + \frac{[\delta\varphi_0(i, j \pm 1)\text{-}\delta\varphi_0(i, j)]^2}{\delta y^2}\right\}. \tag{4.18}$$

In equations (4.16-4.19), δx and δy are the width and height of each pixel, which are independent of i and j. In addition, in Eq. (4.15), the unknown term $\nabla k_{th}(x,y)$ is written as a finite difference in the form:

$$\nabla k_{th}(x,y) \approx \frac{k_{i\pm1,j} - k_{i,j}}{\delta x}\hat{\mathbf{i}} + \frac{k_{i,j\pm1} - k_{i,j}}{\delta y}\hat{\mathbf{j}}. \tag{4.19}$$

where $k_{th}(x,y) \approx k_{i,j}$ at any point (i,j). The FDs expressed by equations (4.16-4.19) can be replaced into Eq. (4.16) to obtain a set of algebraic finite-difference equations of the form

$$X_{i,j} \cdot K_{i\pm1,j} + Y_{i,j} \cdot K_{i,j\pm1} + H_{ij} \cdot K_{i,j} = G_{i,j}, \tag{4.20}$$

in which the following quantities have been defined for compactness:

$$X_{i,j} = U_{i,j}/\delta x$$
$$Y_{i,j} = V_{i,j}/\delta y$$
$$H_{i,j} = X_{i\pm1,j} - 2X_{i,j} + Y_{i,j\pm1} - 2Y_{i,j} - Z_{ij}/h \ . \qquad (4.21)$$
$$G_{i,j} = P_0 \cdot A_0(x,y) \cdot cos\big[\delta\varphi_0(i,j)\big]$$
$$K_{i,j} = (k_{i,j} - k_G)/h$$

Where k_G is the thermal conductivity of the substrate (i.e. $k_{th} = k_G = 1.1$ W/m/K in the case of glass). In total, a number of P×Q scalar equations of the form of Eq. (4.20) can be written to form an algebraic system in the set of unknowns $\{K_{i,j}\}$ which will be numerically solved, giving us a quantity proportional to thermal conductivity along the surface for each point, with a proportionality constant, h, to be determined.

4.3.2 Solution of the finite-difference system with appropriate boundary conditions

It is important to bear in mind that, although Eq. (4.20) is valid in general, for any pixel (i,j) of our images, the thermal conductivity at the boundaries (i.e. at points where $i = 1$ or P, or $j = 1$ or Q) is known and must be equal to the thermal conductivity of the substrate. Due to the linear character of Fourier's equation (4.15), for which the principle of superposition is valid, if we solve a system of equations of the form (4.20) with boundary conditions

$$K_G = K(i = 1 \text{ or } P, j) = K(i, j = 1 \text{ or } Q) = 0, \qquad (4.22)$$

the thermal conductivity at the sample surface will be determined as

$$k_{i,j} = h \cdot K_{i,j} + k_G. \qquad (4.23)$$

Consequently, our method is fully capable to reconstruct thermal conductivity images $\{k_{i,j}\}$ from NeSTRI experiments.

In order to solve our algebraic system, it is convenient to rearrange it by labeling the variables with a single index, $l = 1,\dots$, P×Q, in lieu of two of them, i and j. The scheme used for such a rearrangement is reported in Figure 4.2. Each column j forming the images of the known quantities $X_{i,j}$, $Y_{i,j}$, $H_{i,j}$, and $G_{i,j}$, and of the unknown $K_{i,j}$ is piled in a column vector of P×Q elements. This implies that for a certain number of equations of the form of Eq. (4.20) (specifically at $l = 1,\dots$P; $l = $ P×(Q−1), …, P×Q; $l = j$P; and $l = j$P+1) at least one of the addends at the left hand of Eq. (4.20) corresponds to a boundary condition, for which $K_l = K_G = 0$, and is therefore null. In the specific cases of l pointing to image corners, two of the addends at the left

hand of Eq. (4.20) correspond to boundary conditions and are null. We are dealing with four different types of finite-difference equations of the form (4.20), depending on the number of boundary conditions they involve.
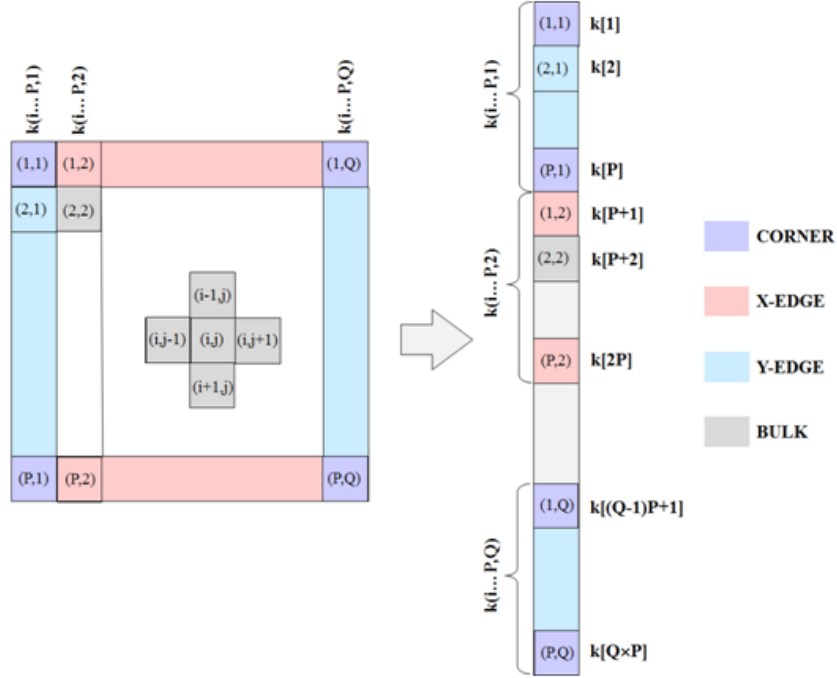
Figure 4.2: Scheme used in our numerical finite-difference calculations to transform pixel images K(j = 1…P, j=1…Q) into column vectors K[1,..., P×Q]. This scheme allows us to transform our finite-difference equation, Eq. (4.20), into an algebraic system of P×Q scalar equations in P×Q unknowns of the type A·K = B. Each scalar unknown, K[1], …, K[P×Q], represents the thermal conductivity of a specific pixel (i,j). The scalar equations have a different formulation depending if the pixel sits at the corner of the image, at an x-edge, at a y-edge, or in the bulk of the image, which is a consequence of the fact that we impose the boundary condition K[b] = k_G for any point at an edge or corner.

a) Corner equations correspond to pixels $(i, j) = (1,1)$; $(i, j) = (P, 1)$; $(i, j) = (1, Q)$ and $(i, j) = (P, Q)$ [for which $l = 1$, $l = P$, $l = (Q-1)×P+1$, and $l = P×Q$ if a single-index notation is used, as in Figure 4.2]. In these cases, we have both $K_{i\pm1,j} = K_G = 0$ and $K_{i,j\pm1} = K_G = 0$. By transferring the known terms to the right hand of Eq. 4.20, we obtain four linear equations of the form

$$H_{ij} \cdot K_{i,j} = G_{i,j} - X_{i,j} \cdot K_G - Y_{i,j} \cdot K_G = G_{i,j}. \tag{4.24}$$

b) x-edge equations correspond to pixels $(i, 1)$ and (i, Q) with $i = 2,\ldots$, P−1 [for which $l = j$P or $l = j$P+1, with $j = 2, \ldots$Q−1) if a single-index notation is used, as in Figure 3.3]. In these cases, we have $K_{i\pm1,j} = K_G = 0$. By moving the known term $X_{i,j}K_G$ to the right hand of Eq. 4.20, we obtain 2×(Q−2) linear equations of the form:

$$Y_{i,j} \cdot K_{i,j\pm1} + H_{ij} \cdot K_{i,j} = G_{i,j} - X_{i,j} \cdot K_G = G_{i,j}. \tag{4.25}$$

c) y-edge equations correspond to pixels $(1, j)$ and (P, j) with $j = 2,\ldots$, Q−1 [for which $l = 2,\ldots$P−1 and $l = $(Q−1)×P+2,$\ldots$,Q×P−1 if a single-index notation is used, as in Figure 4.2]. In these cases, we have $K_{i,j\pm1} = K_G = 0$. By moving the known term $Y_{i,j}K_G$ to the right hand of Eq. (4.20), we obtain 2×(P−2) linear equations of the form:

$$X_{i,j} \cdot K_{i\pm1,j} + H_{ij} \cdot K_{i,j} = G_{i,j} - Y_{i,j} \cdot K_G = G_{i,j}. \tag{4.26}$$

d) Bulk equations correspond to pixels that are not situated at the vicinity of the edges. This implies that, in general, each equation of the form of Eq. (4.20) presents three nonzero unknowns. Equations of type (4.20), in the forms a), b), c) and d), can be combined in a matrix form $\mathbf{A}\cdot K = \mathbf{B}$ that can be solved using sparse-function algorithms (e.g. using Matlab^{TM}) so that $\{K_{i,j}\}$ can be determined. By using the compact, single-index notation for which l = 1, …. P×Q our system $\mathbf{A}\cdot K = \mathbf{B}$ that can be written as:

$$
\begin{pmatrix}
H_{11} & 0 & 0 & 0 & 0 & 0 & 0 & 0 & 0 & 0 \\
-Y_{12} & H_{12} & 0 & 0 & 0 & 0 & 0 & 0 & 0 & 0 \\
0 & -Y_{13} & H_{13} & 0 & 0 & 0 & 0 & 0 & 0 & 0 \\
0 & 0 & . & . & 0 & 0 & 0 & 0 & 0 & 0 \\
0 & 0 & 0 & . & . & 0 & 0 & 0 & 0 & 0 \\
0 & 0 & 0 & 0 & . & . & 0 & 0 & 0 & 0 \\
-X_{21} & 0 & 0 & 0 & 0 & -Y_{1,P} & H_{I,Q} & 0 & 0 & 0 \\
0 & -X_{22} & 0 & 0 & 0 & 0 & . & . & 0 & 0 \\
0 & 0 & . & 0 & 0 & 0 & 0 & . & . & 0 \\
0 & 0 & 0 & . & 0 & 0 & 0 & 0 & Y_{P,Q-1} & H_{PQ}
\end{pmatrix}
\cdot
\begin{pmatrix}
K_{11} \\ K_{21} \\ K_{31} \\ . \\ . \\ . \\ K_{PI} \\ . \\ . \\ K_{PQ}
\end{pmatrix}
=
\begin{pmatrix}
G_{11} \\ G_{12} \\ G_{13} \\ . \\ . \\ . \\ G_{PI} \\ . \\ . \\ G_{PQ}
\end{pmatrix}. \tag{4.27}
$$

After inverting the equation (4.27) using a specially designed Matlab^{TM} routine and determining K, the column vector containing the values of (non-calibrated) thermal conductivity per each pixel have been rearranged into a P×Q matrix.

4.4 Results and Discussion

Figure 4.3 shows the specific heat images obtained by processing the thermoreflectance data by using equations (3.8) and (3.9). It can be observed that, within the experimental errors, the specific heat is independent of the frequency used in the measurements. It can be observed that the specific heat is not significantly different in glass (860 J/Kg/K) and graphite (720 J/kg/K). At room temperature, Dulong-Petit law holds for a large class of materials for which the thermal properties are determined by lattice properties[9]. Consequently, a slowly varying specific heat along the entire surface is realistic. Local variations can only be observed at locations in which the low-dimensional nature of the thin film is more evident, including graphene edges, defects, and particularly thin regions.
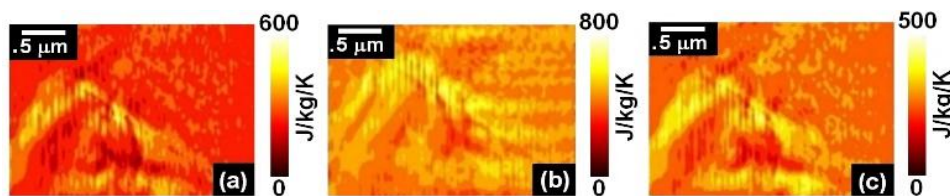
Figure 4.3: a) Images of specific heat for the multilayer graphene flake independently obtained at ω = 75 Hz, b) ω = 200 Hz, and c) ω = 450 Hz.

Figure 4.4 shows the thermal conductivity maps extracted from NeSTRI thermoreflectance images from the same regions and at different frequencies. To confirm our results we compare the thermal conductivity maps for a different number of pixels to make sure they are consistent with one another. From panel b we notice that the thermal conductivity is higher at certain edges than at the center of the graphene flake. There are two types of edges in graphene, armchair, and zigzag. Different atomic spacing along the armchair and zigzag edges result in distinctly different electron and phonon density distributions, with armchair edge atoms forming shorter and stronger bonds[9]. Although the zigzag edges are less dense than armchair edges, the armchair edges have lower energy due to the fact they can form triple bonds[10]. Armchair and zigzag edges also have different phonon distribution of states with the armchair edges having more zone boundary phonons than zigzag edges. Since umklapp processes[11] are responsible for thermal resistivity effects, it is expected that the edge modes with a higher density of states at the zone boundary would have a lower thermal conductivity. In addition, due to the anisotropy in the phonon dispersion for graphene multilayers, zigzag graphene edges

have higher thermal conductance than armchair graphene edges of comparable widths[12]. For the flake under consideration, we recognize both armchair and zigzag edges, in consideration of its triangular shape. Therefore, the different thermal conductivity at the edges may be related to the different edge nature.
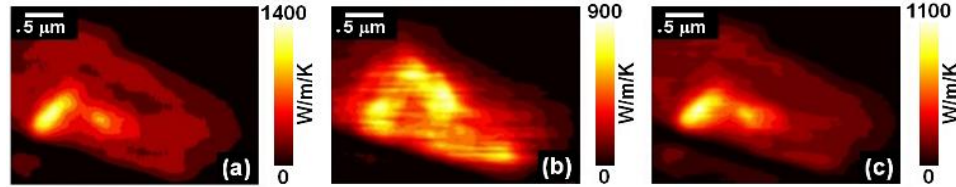
Figure 4.4: Thermal conductivity maps for three different frequencies, a) 75 Hz, b) 200 Hz and c) 450 Hz. The images are similar to each other consistently with the fact that the thermal conductivity is a property of the material, and does not depend on the modulation frequency of the pump beam.

4.5   Conclusion

In this chapter, we introduced the detailed calculations for acquiring thermal conductivity and thermal capacity maps using NeSTRI method. By using Raleigh's law for near-field scattering we found that there is a linear relationship between thermoreflectance amplitude and surface temperature. Finding the proportionality value between the surface temperature and the thermoreflectance amplitude we try to solve Fourier's heat equation. Having the complete set of data from the experiment we solve Fourier's heat equation numerically using the finite difference method. We then implemented the results of NeSTRI measurements discussed in chapter 3, into Fourier's heat equation and we derived the thermal conductivity and heat capacity at each point and therefore developed the thermal conductivity and heat capacity images for the sample. Our method is suitable to be extended to image the thermal properties of a large class of sparse, layered and thin film materials.

4.6   References

[1]   J. D. Jackson, *Classical Electrodynamics* (3rd ed.) New York, John Wiley & Sons

[2]   C. F. Bohren and D. R. Huffman, *Absorption and Scattering of Light by Small Particles*, New York, Wiley-VCH Verlag & Co

[3]   N. Ashcroft and N. D. Mermin, *Solid State Physics*, Saunders College, Philadelphia, 1976

[4]   S.E. Bialkowski, *Photothermal Methods for Chemical Analysis*, New York, Wiley, 1996

[5]   G. Langer, J. Hartmann and M. Reichling, Rev. Sci. Instr. (1997) 68, 1510

[6]   A.D. Rakić, A.B. Djurišic, J.M. Elazar and M.L. Majewski, Appl. Opt. (1998) 37, 5271 - See also http://refractiveindex.info database

[7]   K. A. Atkinson, *An Introduction to Numerical Analysis (2nd ed.)*, John Wiley & Sons, New York, 1989.

[8]   A. Taflove and S. C. Hagness, *Computational Electromagnetics: the finite difference time domain Method,* Artech House, Norwood, 2000

[9]   K. A. Atkinson, *An Introduction to Numerical Analysis (2nd ed.)*, John Wiley & Sons, New York, 1989

[10]   M. J. Assael, S. Botsios, K. Gialou, and I. N. Metaxa, International Journal of Thermophysics, 2005, 26, 1595

[11]   A. J. Schmidt, R. Cheaito, and M. Chiesa, Rev. Sci. Instrum., 2009, 80, 94901

[12]   S. Rudtsch, R. Stosch, and U. Hammerschmidt, in *Proc. 16*th *European Conference on Thermophysical Properties*, London, 2002, 10, 267

Chapter 5

On the role of localized charge transfer and Dirac electrons in limiting the thermal conductivity of graphene layers

5.1 Introduction

A critical application of graphene, that has been vital in translating this starting material from the realm of fundamental physics into applied research and industry, is related to its utilization in heat spreaders, and for thermal evacuation integrated electronic devices at high power density. Tremendous efforts have been done towards understanding the thermal properties of single-layer graphene, virtually a thermal superconductor, with nearly infinite thermal carrier mean free in nearly ideal phonon gases[1, 2]. The unprecedented thermal properties of single-layer graphene also extend to its few-layer counterparts, and to thin graphite, in which in-plane propagation of phonons is still relatively collision-free. To this end, controlling the thermal properties of graphene thin films by assembling metallic structures on their surface[3] would be a promising direction with significant applications. There have been many investigations on the thermal variation of graphene doped materials[4-12] however, the role of electron-phonon scattering in affecting the thermal properties of graphene composites has not been investigated in detail. In 1956, Ziman et al.[13] showed that the thermal conductivity of a material can decrease due to electron-phonon interactions. Although Zimans three particle process with an electron and phonon on one side and an electron on the other side is true in many cases it is unlikely to happen in graphene-based materials.

In this chapter, we study the thermal properties of multilayer graphene thin films decorated by copper particles. We acquire the thermal images of the sample under study by applying the perturbation method to the Fourier heat equation and using near filed thermoreflectance imaging (NeSTRI)[14]. By analyzing and comparing the thermal properties of the multilayer graphene films before and after being deposited by copper particles and later when the copper particles have been etched off the surface of the graphene flake we present a new

explanation based on electron-phonon interaction on the nature of the low local thermal conductivity on the surface of graphene thin films decorated by copper particles.

5.2 Experimental setup

The experimental setup is the same as we had for before for NeSTRI method. We measure the topography, amplitude, transmittance, reflectance and the phase shift of the sample at three different phases, once for when the graphene flake has not yet been decorated with copper particles, once when the graphene flake has been decorated with copper particles and in the end when the copper particles have been etched off the sample Figure 5.1. With the help of these data, we determine the thermal conductivity at the three aforementioned phases.
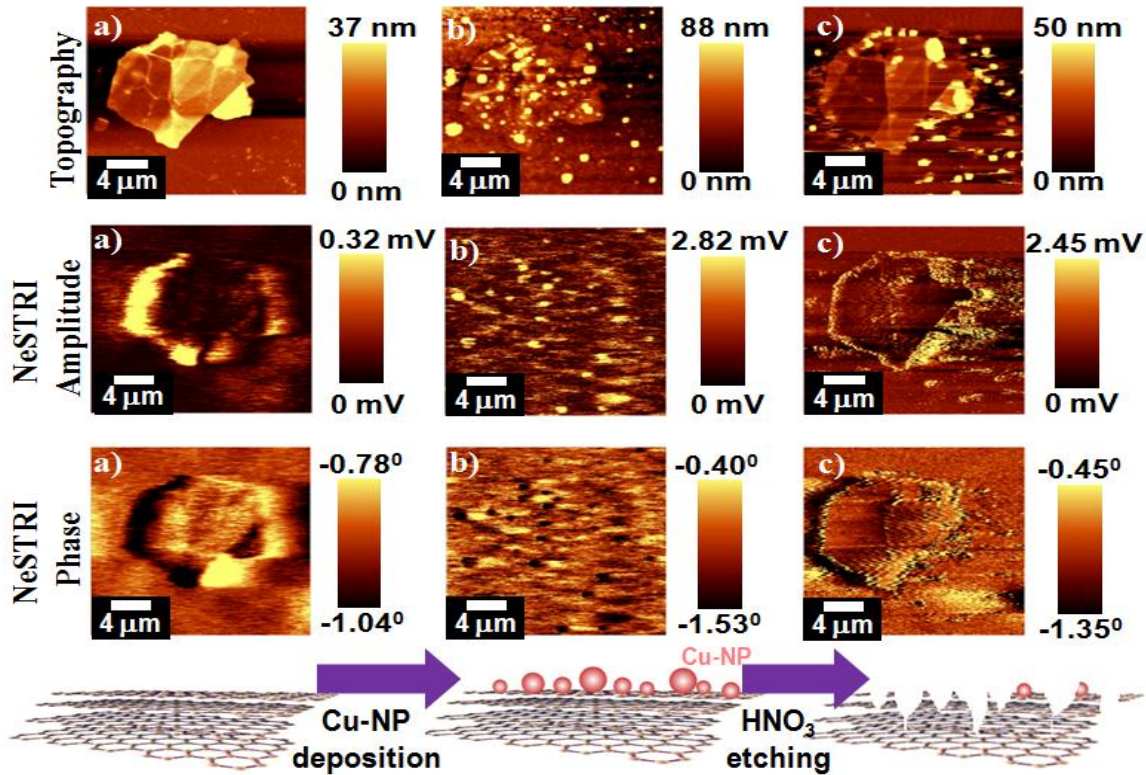
Figure 5.1: The topography, amplitude and the phase shift for a) the graphene flake, b) the graphene flake decorated with copper particles and c) the copper particles etched off the surface of the graphene flake.

5.3 Determining the value of thermal conductivity from measured data

For determining the thermal conductivity of the graphene flake before being decorated by copper particles and after being etched off from it we write Eq. (3.4) which is the Fourier's heat equation:

$$c(x, y)\frac{\partial T(x, y, t)}{\partial t} + \nabla \cdot \left[k_{th}(x, y)\nabla T(x, y, t)\right] = H(x, y, t). \tag{5.1}$$

For writing the Fourier's heat equation for the graphene flake being decorated by copper particles we add a small perturbation term to the primary heat capacity and thermal conductivity of the graphene flake, since the heat capacity and thermal conductivity of copper particles are much less than the heat capacity and thermal conductivity of the graphene flake[15] and we treat them as a perturbation to the system. We also add a small perturbation term to the temperature on the decorated graphene flake since copper particles cannot absorb and obtain much heat to change the temperature on the surface of the sample due to low thermal conductivity and low heat capacity with respect to the graphene flake. The Fourier's equation for the graphene flake decorated with copper particles is:

$$c'(x, y)\frac{\partial T'(x, y, t)}{\partial t} + \nabla \cdot \left[k'_{th}(x, y)\nabla T'(x, y, t)\right] = H'(x, y, t), \tag{5.2}$$

where $c'(x,y)$ and $k'_{th}(x,y)$ are the new heat capacity thermal conductivity of the sample, $H'(x,y,t)$ is the new amount of heat locally absorbed by the sample and $T'(x,y,t)$ is the new temperature. The amount of $H'(x,y,t)$ is measured by experiment in the same way $H(x,y,t)$ was measured in chapter 3. For the new thermal conductivity and heat capacity we write:

$$c'(x, y) = c_{graphene}(x, y) + c_{cu}(x, y), \tag{5.3}$$

$$k'_{th}(x, y) = k_{th,graphene}(x, y) + \lambda(x, y), \tag{5.4}$$

where we have added a first-order perturbation term in terms of $\lambda(x,y)$ and $c_{cu}(x,y,t)$, for the thermal conductivity and heat capacity of the copper particles decorating the surface of the graphene flake. For writing the new temperature we write the primary temperature of the graphene flake $T(x,y,t)$ and add the perturbation $\theta(x,y,t)$ for introducing copper particles.

$$T(x, y, t) = (T_0(x, y)) \cdot \exp\left[i(\omega t + \phi)\right], \tag{5.5}$$

$$\theta(x, y, t) = (\theta_{0//}(x, y)) \cdot \exp\left[i(\omega t + \phi)\right] + (\theta_{0\perp}(x, y)) \cdot \exp\left[i(\omega t + \phi + \pi/2)\right], \tag{5.6}$$

$$T'(x, y, t) = T(x, y, t) + \theta(x, y, t) . \tag{5.7}$$

To be able to solve Fourier's heat equation for the doped graphene sample we divide $\theta(x,y,t)$ into its parallel and perpendicular components, were the parallel component coincides with $T(x,y,t)$ and the perpendicular component is perpendicular to it Figure (5.2).
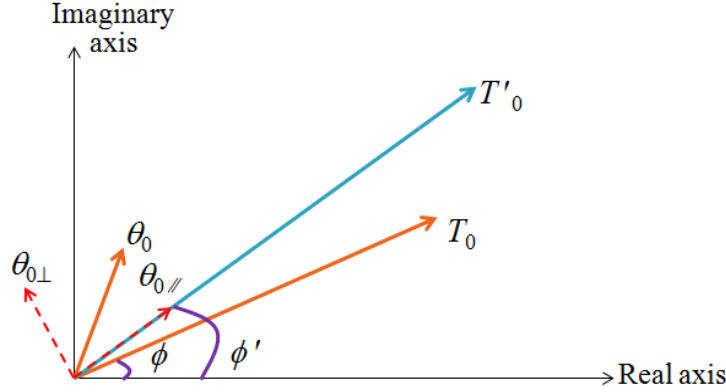
Figure 5.2: The temperature profile in the complex space. We add the primary temperature of the graphene flake $T(x,y,t)$ to the perturbation term $\theta(x,y,t)$ to get the new temperature. We write $\theta(x,y,t)$ in its parallel and perpendicular components with the parallel component coinciding with $T(x,y,t)$.

As can be deducted from Figure 5.2 $\theta_{0\perp}(x,y)$ and $\theta_{0/\!/}(x,y)$ are equal to:

$$\theta_{0\perp}(x, y) = T'_0(x, y)Sin(\phi' - \phi), \tag{5.8}$$

$$\theta_{0/\!/}(x, y) = T'_0(x, y)Cos(\phi' - \phi) - T_0(x, y) . \tag{5.9}$$

Implementing the new thermal conductivity $k'(x,y)$, heat capacity $c'(x,y)$ and temperature $T'(x,y,t)$ into Eq. (4.2) and calculating up to the first order of perturbation we have an equation with two components, real and imaginary, and their physical meaning is associated to the finite thermal diffusivity at which heat propagates along the thin film surface, due to nonzero lateral thermal diffusion length which has been discussed in full length in chapter four. The two components can be separately equated leading to the following identities:

$$\nabla\lambda(x,y)\cdot\nabla T_0(x,y)+\lambda(x,y)\nabla^2 T_0(x,y)-\lambda(x,y)T_0(x,y)\big(\nabla\phi(x,y)\big)^2 =$$
$$\big(H'(x,y)-H(x,y)\big)Cos\phi+\omega c_{graphene}\theta_{0\perp}(x,y)-\nabla k(x,y)\cdot\nabla\theta_{0/\!/}(x,y)-k_{th}(x,y)\nabla^2\theta_{0/\!/}(x,y)+$$
$$k_{th}(x,y)\theta_{0/\!/}(x,y)\big(\nabla\phi\big)^2+\big(\nabla k_{th}(x,y)\cdot\nabla\phi\big)\theta_{0\perp}(x,y)+2k_{th}(x,y)\big(\nabla\theta_{0\perp}(x,y)\cdot\nabla\phi\big)+k_{th}(x,y)\theta_{0\perp}(x,y)\nabla^2\phi$$

$$(5.10),$$

for the real part, and

$$\omega c_{cu}(x,y)T_0(x,y)=-\big(H'(x,y)-H(x,y)\big)Sin\phi-\omega c_{graphene}(x,y)\theta_{0/\!/}(x,y)-\big(\nabla k(x,y)\cdot\nabla\phi\big)\theta_{0/\!/}(x,y)$$
$$-2k(x,y)\big(\nabla\theta_{0/\!/}(x,y)\cdot\nabla\phi\big)-k(x,y)\theta_{0/\!/}(x,y)\nabla^2\phi-\nabla k(x,y)\cdot\nabla\theta_{0\perp}(x,y)-k(x,y)\nabla^2\theta_{0\perp}(x,y)$$
$$+k(x,y)\theta_{0\perp}(x,y)\big(\nabla\phi\big)^2-\big(\nabla\lambda(x,y)\cdot\nabla\phi\big)T_0(x,y)-2\lambda(x,y)\big(\nabla T_0(x,y)\cdot\nabla\phi\big)-\lambda(x,y)T_0(x,y)\nabla^2\phi$$

$$(5.11),$$

for the imaginary part. Given that we already have computed the thermal conductivity $k_{th}(x,y)$ and the heat capacity $c(x,y)$ of the graphene flake[14], the solution of Eq. (5.10) provides $\lambda(x,y)$, which can then be replaced into Eq. (5.11) and $c_{cu}(x,y)$ can be explicitated. Eq. (5.10) can be numerically solved in exactly the same manner that Eq. (5.8) was solved in MATLAB, using the finite difference method[16, 17]. We can then implement $\lambda(x,y)$ into Eq. (5.4) and get the thermal conductivity map of the doped graphene flake.

5.4 Thermal conductivity maps and results

In Figure 5.3 we plot the thermal conductivity map for the three stages of the experiment. Figure 5.3(a) is the thermal conductivity of the graphene flake, Figure 5.3(b) is the thermal conductivity of the graphene flake after being decorated with copper particles and Figure 5.3(c) is for when the copper particles have been etched off from the surface of the graphene flake. By comparing the three thermal conductivity maps we observe a local decrease in thermal conductivity at some points in Figure 5.3(b) and from Figure 5.3(c) we observe that the thermal conductivity again increases as we remove the copper particles off the surface of the graphene flake. The locally low thermal conductivity regions in Figure 5.3(b), are the regions of the graphene flake being decorated by copper particles, and after etching the surface of the graphene flake from copper particles we see that the thermal conductivity is restored to its initial value.
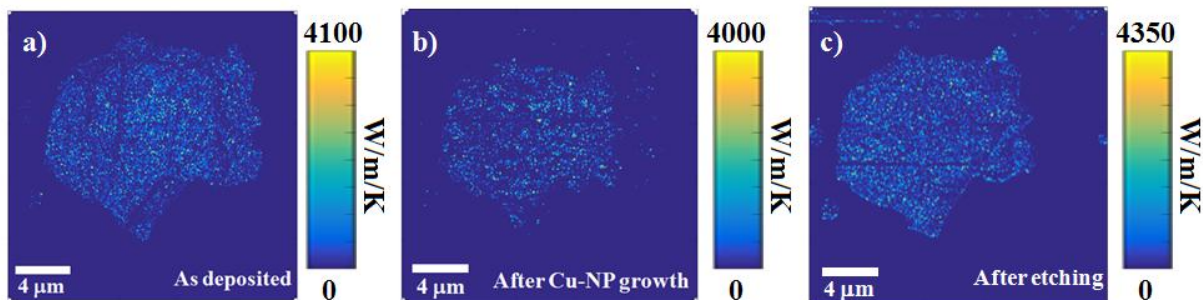
Figure 5.3: The thermal conductivity maps of the three stages of the experiment, a) the graphene flake before being deposited by copper particles, b) the graphene flake after being deposited by copper particles, c) the graphene flake after the copper particles have been etched off from its surface.

In Figure 5.4 we depict some points at the center of the copper particles on the doped graphene flake and move away from them. We observe a low thermal conductivity at the center of the copper particles and an increase in thermal conductivity as we move further away from the center. We also observe that the thermal conductivity varies due to the thickness of the graphene flake.
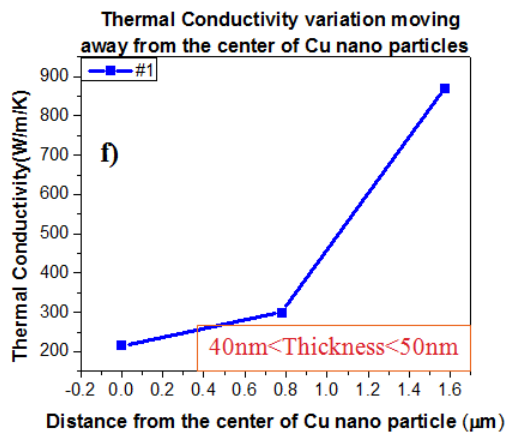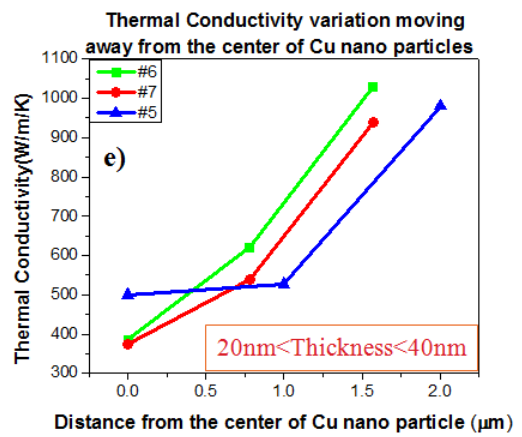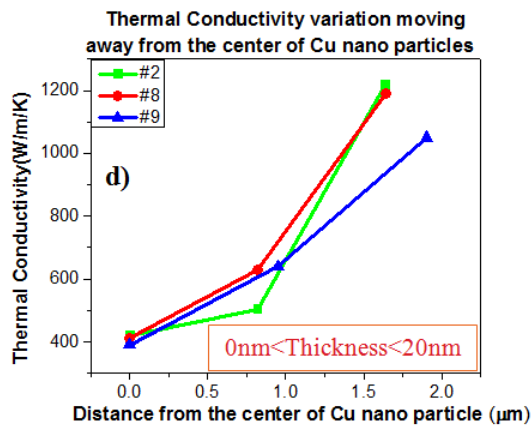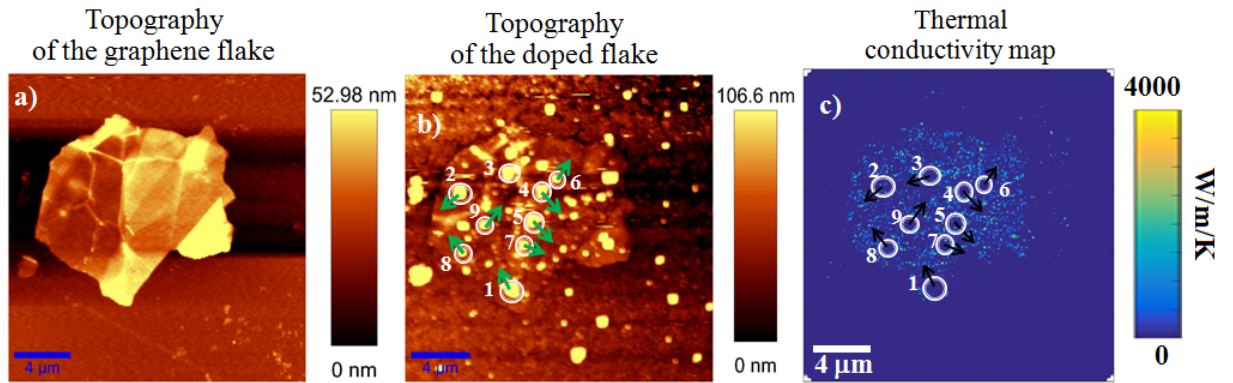
Figure 5.4: Thermal conductivity variations on the doped graphene. d), e), f) Thermal conductivity variation for some of the depicted particles embedded on different thicknesses of the graphene flake. We observe that as we move away from the center of the copper particles the thermal conductivity tends to increase.

In Figure 5.5 we compare the thermal conductivity of various copper particles with different diameters embedded on the surface of the graphene flake to see the relation between the thermal conductivity of copper particles residing on the graphene flake and their circumference. We observe that the thermal conductivity of copper particles decrease as we increase their diameter.
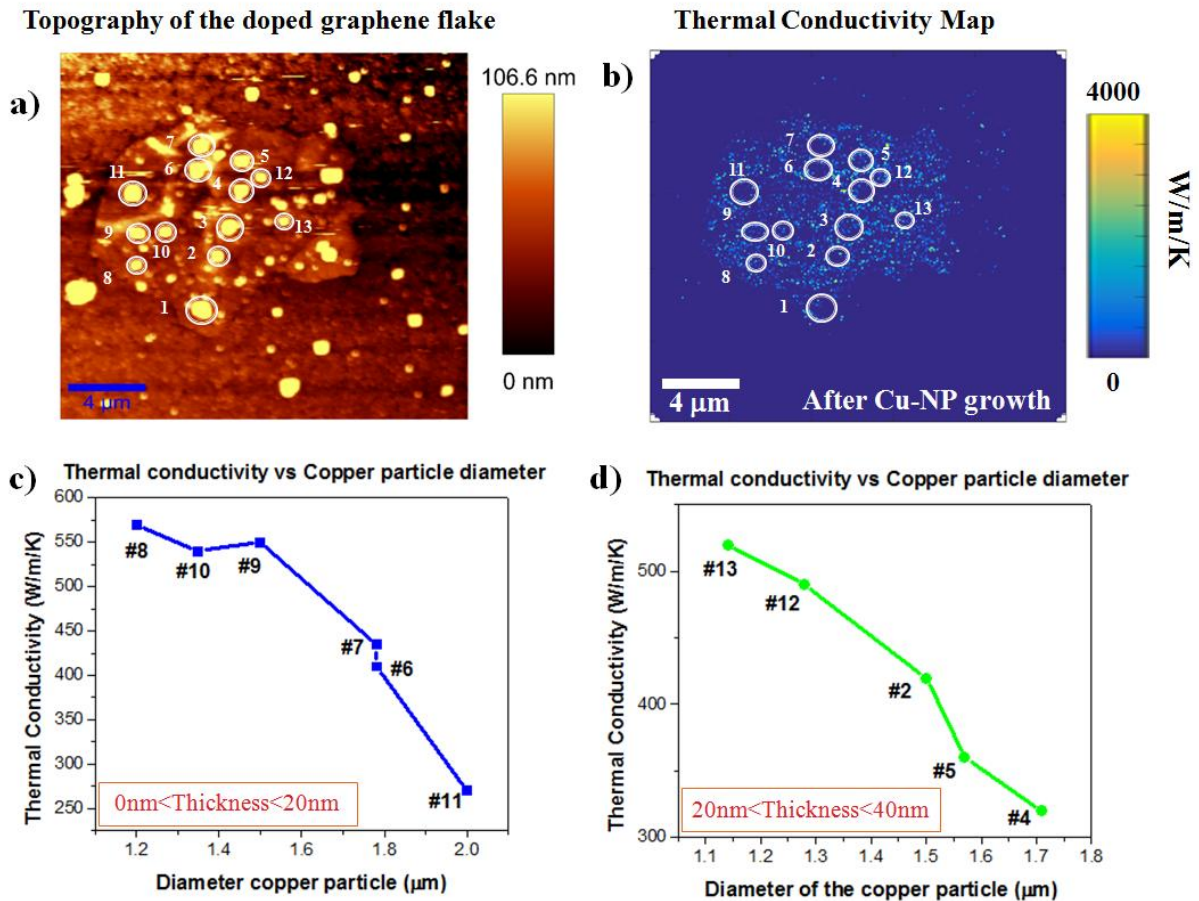
Figure 5.5: The plots for the relation between the diameter of copper particles and their thermal conductivity. a, b) The topography and the thermal conductivity of the graphene flake decorated with copper particles, c, d) the thermal conductivity versus the diameter of the copper particle on a certain region of the graphene flake with a given thickness.

Figure 5.6 shows the thermal conductivity variation along a line at the three stages of the experiment. In Figure 5.6 (d) we have analyzed the thermal conductivity variation along the line A-A′, on the surface of the sample at the three stages.
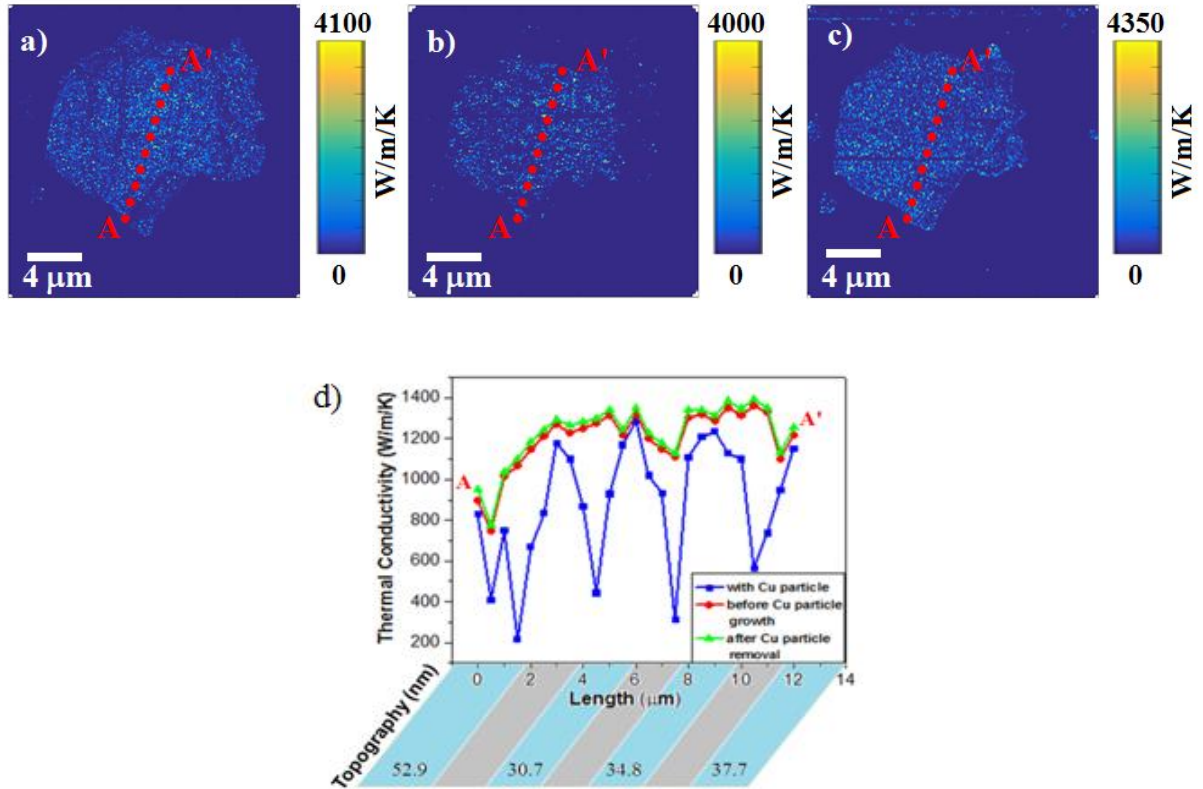
Figure 5.6: The thermal conductivity maps of the three stages of the experiment, a) the graphene flake before being deposited by copper particles, b) the graphene flake after being deposited by copper particles, c) the graphene flake after the copper particles have been etched off from its surface. d) Thermal conductivity variation along the line A-A′at the three stages.

By comparing the three thermal conductivity maps we observe a local decrease in thermal conductivity at areas of the graphene flake deposited by copper particles on the surface and then as we remove these particles from the surface of the graphene flake we observe that the thermal conductivity again increases reaching approximately its initial value.

5.5   Discussion

The local decrease in thermal conductivity on the graphene flake with deposited copper particles on its surface can be the result of one or several of the following phenomenon. Phonon-phonon interaction caused by lattice defects, interfacial thermal resistivity or electron-phonon scattering.

By comparing the thermal conductivity Figures 5.3 at the three stages we observe that as we etch off the copper particles from the surface of the graphene flake its thermal conductivity gets restored approximately to its initial value. This means that the local deficiency in thermal conductivity in regions covered by copper particles is not the result phonon-phonon scattering caused by lattice defects.

By analyzing Figures 5.4 and 5.6 we observe that the local decrease in thermal conductivity is not uniform throughout the whole region covered by copper particles and thermal conductivity increases gradually as we move away from the center of the copper particles and move towards its edges. This means that the local decrease in thermal conductivity cannot be the result of interfacial thermal resistivity either.

Therefore, to understand the main root of the local low thermal conductivity on the surface of the deposited graphene flake we study the nature of heat carriers in graphene thin films and in copper particles. In solids, heat is carried by phonons which are, ion-core vibrations in a crystal lattice and electrons so $k_{th} = k_{th,p} + k_{th,e}$, where $k_{th,p}$ and $k_{th,e}$ are the phonon and electron contributions, respectively. In metals such as copper, k_e is dominant owing to large concentrations of free carriers while in carbon-based materials such as graphene, thermal conductivity is dominated by phonons. The work of Akbari et al. has shown that depositing copper particles on the surface of graphene thin films turns graphene thin films from a band-gap semiconductor, into a semi-metal with Fermi level about 0.2 eV above the Dirac point[18], Figure 5.7.
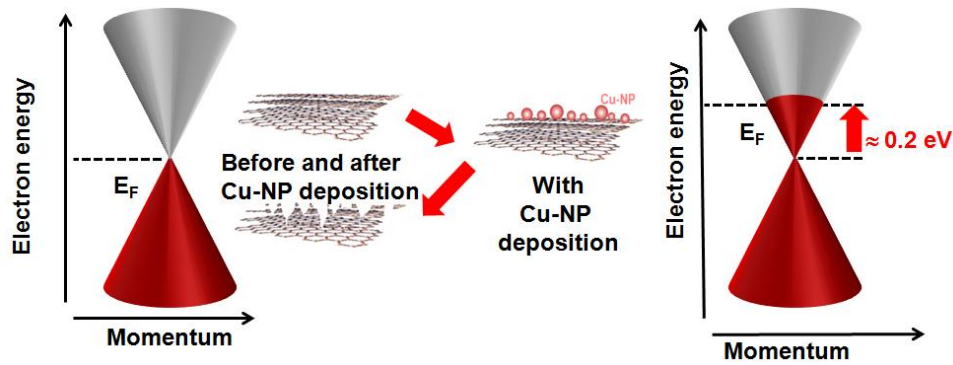
Figure 5.7: The Dirac cone representation. The energy level increases as we deposit copper particles on the surface of the graphene flake and then goes back to its initial value after being etched off.

We postulate that a small amount of the free electrons on the surface of the copper particles transfer to the graphene flake through quantum tunneling. These electrons interact with phonons

and cause a local decrease in thermal conductivity. As Ziemann et al. has shown the local decrease in thermal conductivity due to electron-phonon interaction can be the result of a three particle process between two electrons and a phonon[13], Figure 5.8(a). The process is between an electron and phonon on one side and an electron on the other side. This process is unlikely to happen in the deposited graphene flake under study since, the energy of acoustic phonons is $E_{aco,pho} \approx 0.028$ eV[19] while the energy of the electrons in the doped graphene flake is 0.2 eV and therefore electron-phonon scattering within the graphene flake will be nonresonant. Also, zone boundary electrons couple weakly with acoustic phonons that are mostly zone centered.

Since the local decrease in thermal conductivity due to electron-phonon scattering cannot be explained by a three particle process we study a four-particle process between two electrons and two phonons, figure 5.8(b). The process is between an electron and phonon on one side and an electron and a phonon on the other side. This process is more likely to happen in the deposited graphene flake under study since, to obey the conservation of energy rule we will have optical phonons instead of acoustical phonons with energies near to the electrons in the doped graphene flake[19] and therefore the process will be resonant. Also, since, zone boundary electrons strongly couple with zone boundary phonons we have strong electron-phonon coupling.

We assume the electron-phonon interaction happens in the first Brillouin zone and the outgoing phonon could be scattered in any of the eight neighboring Brillouin zones depicted in Figure 5.8(c, d). If the outgoing phonon is scattered to the 1st, 4th, 5th and 8th lattice sites the momentum of the phonon remains conserved and the collision will be elastic, Figure 5.8(c). If on the other hand the outgoing phonon is scattered to the 2nd, 3rd, 6th and 7th lattice sites the momentum of the phonon does not remain conserved due to Umklapp process[20] and we have to deduct the inverse lattice vector ΓK from the phonons momentum vector which makes the process to be inelastic, Figure 5.8(d).

Since phonons are the main heat carriers in graphene thin films, if we assume the four electron-phonon process to be elastic, Figure 5.8(c), there will be no change in the substance thermal conductivity but, if we assume the four electron-phonon process to be inelastic, figure 5.8(d), the phonons momentum vector will be very small and the lattice vibrations will be zone centred therefore conducting no heat across the lattice. With the probability of the phonon to be scattered equally in any of the eight neighboring lattice sites, we conclude that the local thermal

conductivity of the graphene drops by nearly half its original value when deposited by copper particles on top.
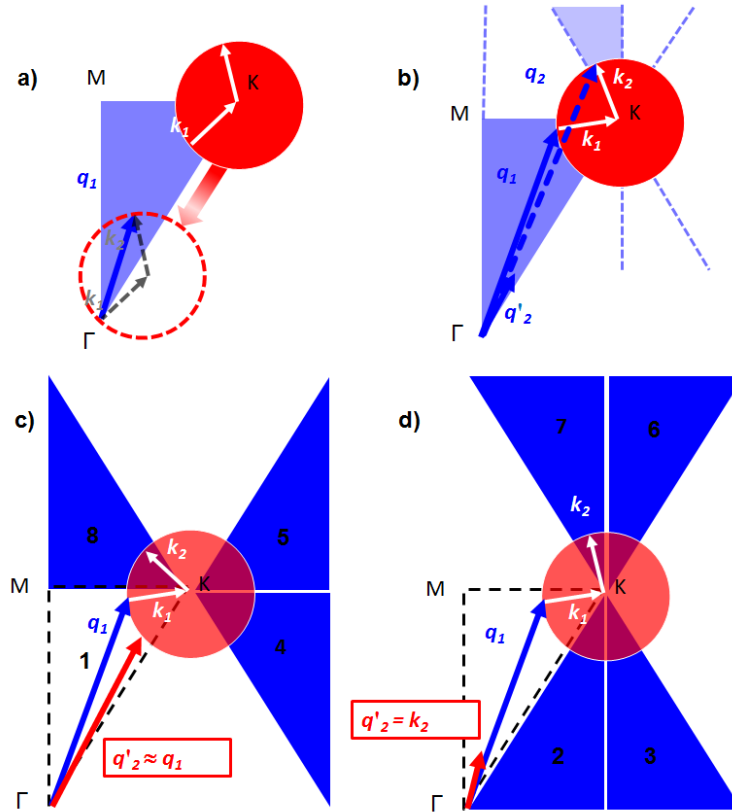
Figure 5.8: Electron-phonon scattering. a) The three particle process between an electron and phonon on one side and an electron on the other side. b) The four particle process between an electron and a phonon on one side and an electron and a phonon on the other side. c) The elastic scattering happening at the 1st, 4th, 5th and 8th lattice sites were k_1 is the momentum of the ingoing electron, k_2 is the momentum of the scattered electron, q_1 is the momentum of the ingoing phonon and q'_2 is the momentum of the scattered phonon. d) The inelastic scattering happening at the 2nd, 3rd, 6th and 7th lattice sites were due to umklapp process the momentum vector of the scattered phonon is deducted from the value of the inverse lattice size ΓK.

5.6   Conclusion

In this chapter, we investigated the thermal properties of multilayer graphene thin films decorated by copper particles. We used a scanning near-field-based thermoreflectance imaging technique to acquire thermal conductivity maps of multilayer graphene thin films at three phases

before and after being decorated by copper particles and later when we etch off the copper particles from its surface. By comparing the results we see a locally low thermal conductivity at regions of the graphene flake being decorated by copper particles, and later on, we see that the thermal conductivity is restored to its initial value after etching the surface of the graphene flake.

By analyzing the results we show that the thermal conductivity of the decorated graphene flake decreases due to electron-phonon scattering. The electron-phonon scattering will be a four particle process which involves an electron and phonon on one side and an electron and phonon on the other side. The scattered phonon could end up equally in any one of the eight nearest neighboring lattices for which half of them the process would be elastic and for the other half, the process would be inelastic. The inelastic process causes the thermal conductivity of the decorated graphene flake to decrease by about half its initial value. In the next chapter, we will discuss the theoretical aspects of electron-phonon scattering.

5.7   References

[1]   B. Tang, G. Hu, H. Gao, L. Hai, International Journal of Heat and Mass Transfer, Volume 85, June 2015, Pages 420-429

[2]   A. A. Balandin, Nature Materials, Aug 2011, Vol. 10, Issue 8, Pages 569-581

[3]   G. Giovannetti, P.A. Khomyakov, G. Brocks, V.M. Karpan, J. Van den Brink, P.J. Kelly, Phys. Rev. Lett., 101 (2008), pp. 026803-026804

[4]   J. C. W. Song, M. Y. Reizer, and L. S. Levitov, Phys. Rev. Lett. 109, 106602, 2012

[5]   L. Hu, T. Desai, P. Keblinski, Phys. Rev. B 83, 195423, 10 May 2011

[6]   Q. X. Pei, Y. W. Zhang, Z. D. Sha, V. B. Shenoy, Appl. Phys. Lett. 100, 101901, Mar 2012

[7]   D. Liu, P. Yang, X. Yuan, J. Guo, N. Liao, Phys. Lett. A, Volume 379, Issue 9, Pages 810-814, Apr 2015

[8]   B. S. Lee, J. S. Lee, Appl. Phys. A, Volume 121, Issue 3, pp 1193–1202, Nov 2015

[9]   J. H. Chen, C. Jang, S. Adam, M. S. Fuhrer, E. D. Williams, M. Ishigami, Nat. Phys 4, 377 – 381, Apr 2008

[10]   M. Trushin, J. Schliemann, Phys. Rev. Lett. 99, 216602, 21 Nov 2007

[11]   X. Z. Yan, Y. Romiah, C. S. Ting, Phys. Rev. B 77, 125409, 13 Mar 2008

[12]   S. Xiao, J.H. Chen, S. Adam, E.D. Williams, and M.S. Fuhrer, Phys. Rev. B 82, 041406, July 2010

[13]   J. M. Ziman, The *effect of free electron on lattice conduction*, Philosophical Magazine, Volume 1, Issue 2, 1956

[14]   S. Ezugwu, S. Kazemian, D. Choi, G. Fanchini, Nanoscale, 2017, 9, 4097-4106

[15]   A. A. Balandin, D. L. Nika, S. Ghosh, Applied Physics Letters, 2009, Volume 94, Issue 20

[16]   K. A. Atkinson, *An Introduction to Numerical Analysis (2nd ed.)*, John Wiley & Sons, New York, 1989.

[17]   A. Taflove and, S. C. Hagness, *Computational 81 electromagnetic: the finite difference time domain Method,* Artech House, Norwood, 2000

[18]   A. Akbari-Sharbaf, S. Ezugwu, M.S. Ahmed, M.G. Cottam, and G. Fanchini, Carbon, 95 (2015) 199-207

[19]   A. C. Ferrari and J. Robertson, Phys. Rev. B, Volume 61, Number 20, May 2000

[20]   N. W. Ashcroft and D. N. Mermin, *Solid State Physics*, Saunders College, Philadelphia, 1976

Chapter 6

Theory of phonon scattering by Dirac electrons in doped graphene

6.1   Introduction

In order to apply graphene-based materials in nanoscale systems, it is of paramount importance to establish the relationship between their molecular structure and their thermal properties. In the recent years, there has been a significant effort to locally modify the thermal and electrical properties of graphene and to characterize these local modifications[1, 2, 3].

There is a general census that indicates that the thermal conductivity of graphene decreases when it is doped substantially[4, 5]. In the previous chapter, we discussed the role of electron-phonon interactions in locally decreasing the thermal conductivity of the doped graphene. Studies on electron-phonon interactions in solids have been done for three particles processes consisting of two electrons and a phonon. In the three particle process an electron and a phonon collide with each other and get annihilated and a new electron is created or an electron decays into a new electron and phonon[6, 7]. Doing calculations for the three particle process, Ziman et al.[8] showed that the thermal conductivity of solid crystal decreases due to electron-phonon scattering. Although this is true in some solids in doped graphene films, the calculations must be carried out to higher order terms in which more than three particles are involved the electron-phonon interaction process.

In this chapter as a case study, electron-phonon interaction is applied to multilayer graphene thin films decorated with copper particles on top. We show through calculations that electron-phonon interactions are responsible for the local decrease in thermal conductivity along the surface of graphene doped materials. We show that the three particle process consisting of two electrons and one phonon is unlikely to happen and we carry out the calculations for a five particle process consisting of three electrons and two phonons. All the calculations are carried out at room temperature so that the Fermi-Dirac statistics is taken as a step function[9] and we assume that the particles move in a nonrelativistic framework.

6.2 Electron-phonon interaction

The basic idea underlying the electron-phonon interaction is that when ions sit at their equilibrium positions, the state of an electron is described by a Bloch function[10] of wave vector k and band index *n*. A phonon disturbs the lattice, and ions move out of their equilibrium positions. This causes a change in the potential of the electron which causes the electron to get scattered into another state with wave vector k'. For explaining the locally low thermal conductivity at regions of the graphene flake decorated by copper particles we calculate the electron-phonon interaction in the graphene flake. We assume that a small portion of the electrons in the copper particles transfer to the surface of the graphene flake through quantum tunneling and thus the thermal conductivity of the graphene flake in the regions covered by copper particles decrease due to electron-phonon interactions.

In order to understand this phenomenon, we consider two different models. The first model which is a three particle process involves two electrons and a phonon and the second model which is a five particle process involves three electrons and two phonons were one of the electrons acts as a fermion propagator.

We consider the graphene lattice consisting of *N* unit cells with a basis of *x* atoms. The displacement from equilibrium of atom *l* (l = 1, 2, .. , *x*) in unit cell *n* (n =1, 2, ... *N*) is denoted by the phonon wave function which is:

$$\varphi_{n,l} = \frac{1}{\sqrt{NM_l}} \sum_{q,\lambda} \sqrt{\frac{\hbar}{2\omega_{q\lambda}}} e^{-i(\omega_q t - qR_n)} \varepsilon_\lambda(q) b_{q\lambda} \,, \tag{6.1}$$

where M_l is the mass of atom *l* and ε_λ is the polarization vector that determines the direction of the displacement of the lattice vibration relative to the wave vector *q*. ω_q is the frequency of the of lattice vibration, b_q is the annihilation operator and we use $R_{n,l}$ to describe the location of the ion *l* = 1, ..., *r* belonging to unit cell *n* = 1, ..., *N*.

a) Three particle process

For simplicity of notation, we assume that there is one atom per unit cell. The Hamiltonian of the electron-phonon interaction for the three particle process Figure 6.1, within the lattice is[11]:

$$H_{el-ph} = -\frac{1}{\sqrt{NM}} \sum_{\substack{n,q \\ \lambda}} \sum_{\substack{k,k' \\ \sigma,\sigma'}} \sqrt{\frac{\hbar}{2\omega_{q,\lambda}}} \psi^*_{k'}(\vec{x}) e^{-i(\omega_q t - qR_n)} b_{q,\lambda} \varepsilon_\lambda(q) \cdot \frac{\partial V_l(\vec{x} - \vec{R}_{n,l})}{\partial \vec{R}_{n,l}} \psi_k(\vec{x}) c^*_{k'\sigma'} c_{k\sigma} \,, \tag{6.2}$$

where V_l is the Thomas-Fermi screening potential[16]. We can proceed a bit further if we adopt the effective mass approximation:

$$\psi_k(x) = \frac{1}{\sqrt{V}} e^{i\vec{k}\cdot\vec{x}} \;,$$

(6.3)

where V is the volume of the crystal. To calculate the interaction Hamiltonian we express the potential V_l in terms of its Fourier transform. This would be equal to:

$$V_l(\vec{x} - \vec{R}_{n,\alpha}) = \frac{1}{V} \sum_Q e^{iQ(x - R_{n,l})} V_Q \;,$$

(6.4)

where Q is the Fourier component of the potential.
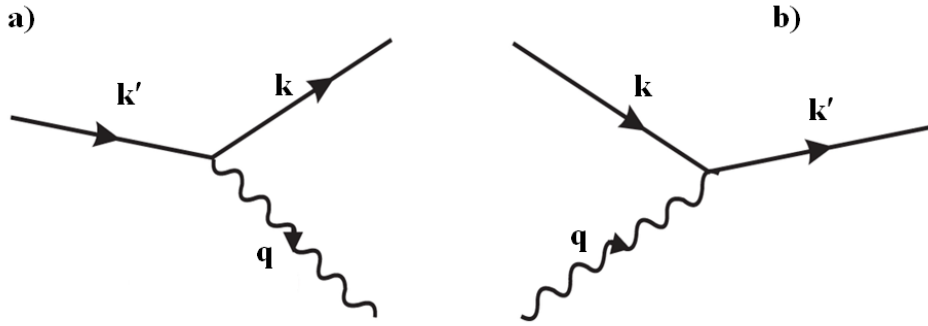
Figure 6.1: The three particle process of electron-phonon scattering. a) The electron decays into a new electron and a phonon. b) Electron and phonon collision creating a new electron

Now we apply Wick's theorem[12, 13] to the Hamiltonian of the electron-phonon interaction. By applying the Wick's theorem we can calculate the transition probability for the three particle process between its initial and final. According to Wick's theorem we write:

$$S = \sum_n \frac{1}{n!} \int_{-\infty}^{\infty} d^4x_1...d^4x_n T\{H_{int}(x_1)...H_{int}(x_2)\},$$

(6.5)

where T is the time ordering operator and n is the number of interactions that we have. For the three particle process we write:

$$S = -\frac{1}{\sqrt{NM}} \int_{-\infty}^{\infty} d^4x \sum_{\substack{n,q \\ \lambda}} \sum_{\substack{k,k' \\ \sigma,\sigma'}} \sqrt{\frac{\hbar}{2\omega_{q,\lambda}}} \psi^*_{k'}(\vec{x}) e^{-i(\omega_q t - qR_n)} b_{q,\lambda} \varepsilon_\lambda(q) \cdot \frac{\partial V_l(\vec{x} - \vec{R}_{n,l})}{\partial \vec{R}_{n,l}} \psi_k(\vec{x}) c^*_{k'\sigma'} c_{k\sigma} \;.$$

(6.6)

The following process is unlikely to happen in the doped graphene flake under study. If we assume the phonon to be acoustical its energy would be $E_{aco,\;pho} \approx 0.028$ eV[15] while the energy of the electrons in the doped graphene flake is 0.2 eV[14] and therefore electron-phonon

scattering within the graphene flake will be nonresonant. On the other hand, if we assume the phonon is optical its energy would be $E_{opt,pho} \approx 0.18$ eV[15] and therefore it would violate the conservation of energy. Also, zone boundary electrons couple weakly with acoustic phonons that are mostly zone centered.

b) Five particle process

The Hamiltonian of the electron-phonon interaction for the five particle process Figure 6.2, within the lattice, is:

$$H_{el-ph} = \frac{1}{NM} \sum_{\substack{n,l \\ \lambda,\lambda'' \\ q,q'' \\ k,k',k''}} \sqrt{\frac{\hbar^2}{4\omega_{q\lambda}\omega_{q''\lambda''}}}$$

$$\psi^*_{k''}(\vec{x}) c^*_{k''} b_{q''\lambda''} e^{i\left(\omega_{q''}t - q''R_n\right)} \varepsilon_{\lambda''}(q'') \cdot \frac{\partial V_l\left(\vec{x} - \vec{R}_{n,l}\right)}{\partial \vec{R}_{n,l}} c_{k'}\psi_{k'}(\vec{x})\psi^*_{k'}(\vec{x}) c^*_{k'} b_{q\lambda} e^{-i\left(\omega_q t - qR_n\right)} \varepsilon_{\lambda}(q) \cdot \frac{\partial V_l\left(\vec{x} - \vec{R}_{n,l}\right)}{\partial \vec{R}_{n,l}} c_k \psi_k(\vec{x})$$

$$. \quad (6.7)$$

The spin of the electron doesn't change in the electron-phonon interaction so we won't sum over the different spins.

By applying the Wick's theorem for the five particle process we calculate the transition probability between the initial and final state. To solve the integral we make use of the following equations:

$$\sum_n e^{i(q-Q)R_n} = N\delta_{q,Q}, \quad (6.8)$$

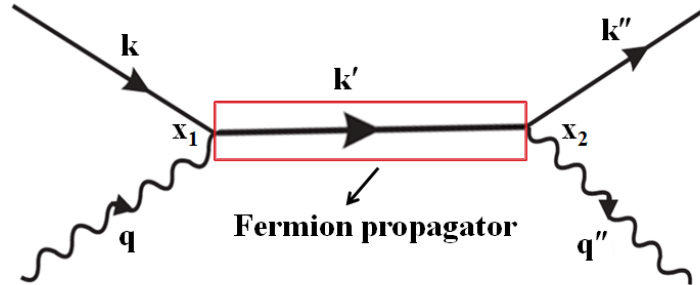$$\int \exp i(Q+k-k')d^3x = (2\pi)^3 \delta_{Q,k'-k}. \quad (6.9)$$

Figure 6.2: The five particle process of electron-phonon scattering. An electron and phonon collide with each other creating a medium electron which carries their momentum and energy and then the medium electron decays into a new electron and phonon

Since graphene thin layers are approximately two dimensional we do the calculations in the two dimensions of space and one dimension of time. Making use of the following equations the integral over the interaction Hamiltonian is:

$$S = \frac{N}{MV^4} \sum_{\substack{\lambda,\lambda'' \\ q,q'' \\ k,k''}} \sqrt{\frac{\hbar^2}{4\omega_{q\lambda}\omega_{q''\lambda''}}} \int d^2x_2 dt_2 d^2x_1 dt_1$$

,(6.10)

$$\left[c^*_{k''}b^*_{q''\lambda''}e^{iE''t-ik''x}e^{i\omega_{q'}t-iq''R_n}\varepsilon_{\lambda''}(q'')\cdot q''V_{q''}\right]_{2,x_2} iS_F(x_2-x_1)\left[c_k b_{q\lambda}e^{-iE''t+ik''x}e^{-i\omega_{q'}t+iq''R_n}\varepsilon_{\lambda}(q)\cdot qV_q\right]_{1,x_1}$$

Where the medium electron is the fermion propagator denoted as $iS_F(x_2-x_1)$. Solving the integral and taking its expectation value between the initial and final state we have:

$$\langle S_{fi} \rangle = \frac{N}{MV^4} \sum_{\substack{\lambda,\lambda'' \\ q,q'' \\ k,k''}} \sqrt{\frac{\hbar^2}{4\omega_{q\lambda}\omega_{q''\lambda''}}} \frac{i}{(2\pi)^3} \int d^3p \int d^2x_2 dt_2 \exp\left[-i(E'-\omega_{q''}-E'')t_2\right]\exp\left[-i(\vec{k}''+\vec{q}''-\vec{k}')x_2\right]$$

$$\vec{q}''\cdot\varepsilon_{\lambda''}(q'')V_{q''}S_F(p)\int d^2x_1 dt_1 \exp\left[-i(E+\omega_q-E')t_1\right]\exp\left[-i(\vec{k}+\vec{q}-\vec{k}')x_1\right]\vec{q}\cdot\varepsilon_{\lambda}(q)V_q$$

(6.11)

By inserting Eq. (6.8) into Eq. (6.11) we get:

$$\langle S_{fi} \rangle = i\frac{N(2\pi)^3}{MV^4} \sum_{\substack{\lambda,\lambda'' \\ q,q'' \\ k,k''}} \sqrt{\frac{\hbar^2}{4\omega_{q\lambda}\omega_{q''\lambda''}}} \delta(E''+\omega_{q''}=E+\omega_q)\delta(\vec{k}''+\vec{q}''-K=\vec{k}+\vec{q})$$

,(6.12)

$$\vec{q}''\cdot\varepsilon_{\lambda''}(q'')V_{q''}S_F(p)\vec{q}\cdot\varepsilon_{\lambda}(q)V_q$$

where the Dirac delta enforces energy and momentum conservation. If the emitted phonon and electron get scattered to a neighboring reciprocal lattice site the initial and final crystal momenta will differ by a nonzero reciprocal lattice vector, K. We write the fermion propagator in the momentum space in a nonrelativistic framework. The fermion propagator is:

$$S_F(p) = \frac{i}{E'-v_F\vec{k}'+i\varepsilon},$$

(6.13)

where v_F is the fermion velocity inside the lattice for room temperature and ε is a scalar with $\varepsilon \to 0$.

For the potentials V_q and $V_{q''}$ we make the following assumption. Since ions move very slowly compared to electrons, we can assume that the screening is static, similar to the screening of a fixed charged impurity. The screened Coulomb potential of an ion is thus taken to be 4π $Ze/q^2 \varepsilon(q, 0)$, where Ze is the ionic charge and $\varepsilon(q, 0)$ is the static dielectric function. In the

calculations we use the Thomas Fermi screening potential[16] and the screening potential will be 4π $Ze/(q^2+ q_{TF}^2)$, where q_{TF} is the Thomas Fermi wave number. We won't carry out the calculations to higher order terms since the screening potential is smaller than one and the process will become more and more unlikely if we add more interactions to the electron-phonon scattering process.

The transition probability for the absorption of an electron and phonon at point x_1 and the emission of an electron and phonon at point x_2 is:

$$W = \frac{\left|\langle S_{fi} \rangle\right|^2}{T},$$

(6.14)

where T is the time for the entire process to take place. Inserting Eq. (6.12) and Eq. (6.13) into Eq. (6.14) we get the following equation for the transition probability of the electron-phonon interaction:

$$W = \frac{N^2(2\pi)^6}{M^2V^7} \sum_{\substack{\lambda,\lambda'' \\ q,q'' \\ k,k''}} \left(\frac{\hbar^2}{4\omega_{q\lambda}\omega_{q''\lambda''}}\right) \delta\left(E'' + \omega_{q''} = E + \omega_q\right) \delta\left(\vec{k}'' + \vec{q}'' - \vec{K} = \vec{k} + \vec{q}\right)$$

$$\left[\vec{q}'' \cdot \varepsilon_{\lambda''}(q'')V_{q''} \frac{1}{E'' + \omega_{q''\lambda''} - v_F(\vec{q}'' + \vec{k}'')} \vec{q} \cdot \varepsilon_\lambda(q)V_q\right]^2$$

(6.15)

In the next section, we will find the value of W by summing over the electrons and phonons momentum values in the lattice.

6.3 Calculating the thermal conductivity

We carry out our calculations in the reciprocal lattice frame, Figure 6.3. Since we are working at sufficiently low temperatures, the momentum for the absorbed and emitted electrons will be:

$$k'' \approx k = \frac{E_F(eV)}{v_F(eV \cdot A)} \approx \frac{0.2}{6.5} \approx 3\times10^{-2}\mathring{A}^{-1},$$

(6.16)

where k is the momentum of the absorbed (incoming) electron and k'' is the momentum of the emitted (outgoing) electron. As the Fermi-Dirac function at sufficiently low temperature is nearly a step function, the joint density of occupied (i) and unoccupied (o) electronic states is close to being a Dirac delta in the proximity of the Fermi energy, E_F, of "doped" graphene and, therefore, both k and k'' are about $k = E_F/v_F$. Previous works have demonstrated that contact of

few-layer graphene with copper nanoparticles is actually very similar to a doping effect, with charge transfer from Cu to the π-electronic states of the graphene sheets[14]. Movements of the Fermi level associated with such a charge transfer "doping" effect moves the Fermi level up to 0 $< E_F < 0.2$ eV above the vertex of the Dirac cone of the π and π* electronic bands of graphene at the Dirac point K, with a constant and dispersionless Fermi velocity v_F =6.5 eV·Å. Therefore, charge transfer of Cu particles results in the appearance of conduction electrons at the zone-boundary K point. Such electrons scatter phonons to a neighboring Brillouin zone with a certain probability that determines the corresponding limitations in the thermal conductivity of "doped" graphene over its undoped counterparts.

Figure 6.3(b) shows the electron-phonon interactions in the reciprocal lattice were, q and k are the absorbed phonon and electron and q'' and k'' are the new emitted electron and phonon. We assume that the electron-phonon absorption occurs in the first reciprocal lattice site and based on the angle of the collision the new phonon and electron could be scattered in the first Brillouin zone or any of the 7 reciprocal neighboring lattice sites.
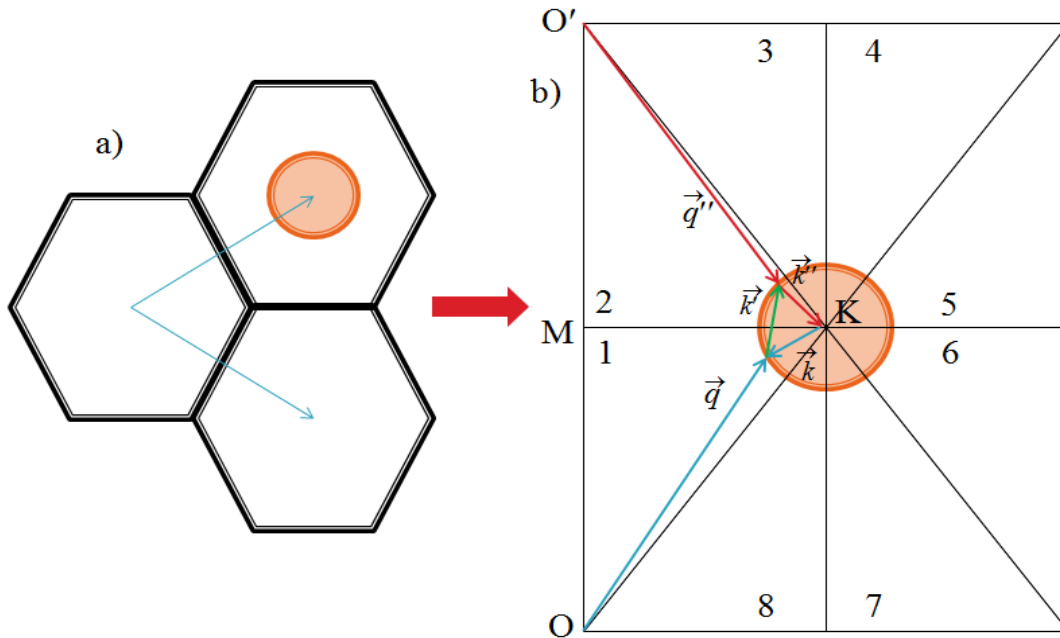

Figure 6.3: a) The copper particle at the center of the graphene lattice. b) The electron-phonon scattering in the reciprocal lattice.

Based on the umklapp process[16] the initial and final crystal momenta differ by a nonzero reciprocal lattice vector, K. As we studied in the previous chapter after the phonon has been scattered off by the electron there is a 50% chance for it to end up in the 1st, 2nd, 5th and 6th reciprocal lattice and a 50% chance for it to end up in the 3rd, 4th, 7th and 8th reciprocal lattice. In the first case, the phonons momentum does not change and we would have an elastic collision were $q'' - K = q$. In the second case, the collision would be inelastic and $q'' - K = k$.

To solve Eq. (6.15) we write:

$$W = \frac{N^2(2\pi)^6}{M^2 V^7} \frac{1}{(2\pi)^4} \int_{q_{min}}^{q_{max}} d^2q \int_{q''_{min}}^{q''_{max}} d^2q'' \sum_{\lambda,\lambda''} \left(\frac{\hbar^2}{4\omega_{q\lambda}\omega_{q''\lambda''}} \right) \delta\left(E'' + \omega_{q''} = E + \omega_q\right) \delta\left(\vec{k}'' + \vec{q}'' - K = \vec{k} + \vec{q}\right)$$

$$\left[\vec{q}'' \cdot \varepsilon_{\lambda''}(q'') V_{q''} \frac{1}{E'' + \omega_{q''\lambda''} - v_F(\vec{q}'' + \vec{k}'')} \vec{q} \cdot \varepsilon_{\lambda}(q) V_q \right]^2 \quad , (6.17)$$

where we have replaced the summation over the phonons momentum with an integration between its maximum and minimum values. Since the momentum of the electron should be $k = k'' = E_F/v_F$ in order for the electron-phonon interaction to take place we won't sum over the different values of the momentum of the electron. Integrating over the 8 reciprocal lattice neighboring sites we have:

$$W = \frac{4N^2(2\pi)^2}{M^2 V^7} \sum_{\lambda,\lambda''} \left(\frac{\hbar^2}{4\omega_{q\lambda}\omega_{q''\lambda''}} \right) \cdot$$

$$\left[\left[\int_{q_{min}}^{q_{max}} d^2q \left[\vec{q} \cdot \varepsilon_{\lambda''} V_{q''} \frac{1}{E + \omega_q - v_F(\vec{q} + \vec{k})} \vec{q} \cdot \varepsilon_{\lambda} V_q \right]^2 + \int_{q_{min}}^{q_{max}} d^2q \left[\vec{k} \cdot \varepsilon_{\lambda''} V_{q''} \frac{1}{E + \omega_q - v_F(\vec{k} + \vec{k})} \vec{q} \cdot \varepsilon_{\lambda} V_q \right]^2 \right] \right],$$

(6.18)

where, the electron-phonon collision is elastic when the emitted phonon gets scattered to 4 of the reciprocal lattice sites and, the electron-phonon collision is inelastic when the phonon gets scattered to the other 4 reciprocal lattice sites.

In order to find the maximum and minimum amount of the phonons momentum we write:

$$q_{max} = \sqrt{|OK|^2 + \frac{E^2_F}{v^2_F} - \frac{2|OK|E_F}{v_F}\cos\left(\frac{\pi}{3}\right)} \approx 1.205 A^{-1}, \quad (6.19)$$

$$q_{min} = |OK| - \frac{E_F}{v_F} \approx 1.19 A^{-1}, \quad (6.20)$$

wherein the particular case of graphene[16] |OK| = 1.22 Å^{-1}.

89

To calculate the thermal conductivity of the electron-phonon interaction in 2 dimensions we write[17]:

$$k_{th} = \frac{1}{2} c_v c^2 \frac{1}{W} \; . \tag{6.21}$$

Here c_v is the specific heat of the phonon and c is the speed of sound inside a specific medium. Calculating the ratio of the thermal conductivity without the copper particle and with the copper particle at the center of the graphene flake we arrive at the given result:

$$\frac{k_{th,after}}{k_{th,before}} < 1 \,, \tag{6.22}$$

This states that the thermal conductivity has decreased due to electron-phonon scattering. This was expected since the phonon momentum decreases significantly in half the reciprocal lattice sites due to the umklapp process.

6.4   Conclusion

In this chapter, we calculated the electron-phonon interaction in doped graphene. We did the calculations for a three particle process consisting of an electron and phonon on one side and an electron on the other side. We showed that due to the fact that the three particle process is nonresonant and there is weak coupling between electrons and acoustical phonons this process is unlikely to happen. We then studied higher order interactions consisting of three electrons and two phonons. We took the middle electron to be the Feynman propagator. We used Feynman diagram to find the transition probability of the electron-phonon interaction and from this, we calculated the thermal conductivity in doped graphene. By comparing the thermal conductivity of the graphene flake before and after being decorated by copper particles we observe a decrease in thermal conductivity for the decorated graphene flake which confirms our results in chapter 5.

6.5   References

[1]   A. A. Balandin, S. Ghosh, W. Bao, I. Calizo, D. Teweldebrhan, F.Miao, C.N. Lau, Nano Lett. 8, 902–907 (2008)

[2]   J. Jiang, J. Wang, and B. Li, Phys. Rev. B 79, 205418, May 2009

[3]   T. Ouyang, Y. Chen, Y. Xie, G. M. Stocks, J. Zhong, Appl. Phys. Lett. 99, 233101, 2011

[4]   S. Hu, J. Chen, N. Yang, B. Li, Carbon, Volume 116, Pages 139-144, May 2017

[5]   B .S. Lee, J .S .Lee, Appl Phys. A, Volume 121, Issue 3, pp 1193–1202, Nov 2015

[6]   Jishi, A. Radi, *Feynman diagram techniques in condensed matter physics*, Cambridge University Press, 2013

[7]   J. C. W. Song, M. Y. Reizer, and L. S. Levitov, Phys. Rev. 109, 106602, Sep 2012

[8]   J. M. Ziman, The *effect of free electron on lattice conduction*, Philosophical Magazine, Volume 1, Issue 2, 1956

[9]   Pathria, R. K, *Statistical mechanics*, Butterworth-Heinemann, 1996, 2nd ed.

[10]   N. W. Ashcroft and D. N. Mermin, *Solid State Physics*, Saunders College, Philadelphia, 1976

[11]   Rose, Albert, *Electron phonon interactions*, World Scientific, 1989

[12]   Mandl, Shaw, Quantum field theory, J.Wiley 1993, Rev.ed.

[13]   T.S. Evans, D.A. Steer, Nuclear Physics B 474, 481-496, 1996

[14]   A. Sharbaf, S. Ezugwu, M. S. Ahmed, M. G. Cottam, G. Fanchini, Carbon, Volume 95, Pages 199-207, Dec. 2015

[15]   A. C. Ferrari and J. Robertson, Phys. Rev. B, Volume 61, Number 20, May 2000

[16]   C. N. R. Rao and A. K. Sood, *Graphene synthesis, properties, and phenomena*, Wiley-VCH, Weinheim Germany, 2013

[17]   N. W. Ashcroft and D. N. Mermin, *Solid State Physics*, Saunders College, Philadelphia, 1976

7.   Conclusion and Future Work

In chapter 2 we studied the thermal property at the macroscopic level. We used PDS which is a contactless method to measure the thermal conductivity of a thin films-substrate system for the first time. By using different models constructed for measuring two-side PDS systems we managed to compute the amplitude and phase shift of the deflection angle of the probe beam which led to the measurement of the thermal conductivity in such systems. In future studies, we can study a three-dimensional temperature profile and apply the Fermat's principle to observe the deflection angle for more complicated and accurate results.

In chapter 3 and 4 we studied the thermal property at the mesoscopic level. We introduced NeSTRI, a scanning near-field-based thermoreflectance imaging technique capable of mapping the thermal properties of thin solid films at the nanoscale and presented the mathematical technique which we used to get the thermal images using NeSTRI. We developed the thermal conductivity and the heat capacity maps and studied the properties of the material under study. In future studies, a new method can be devised to map the thermal diffusivity of the sample. Also by having the thermal images of different nanocomposites, we can study the interfacial thermal resistivity between them in depth. In addition in the near-field scattering, we neglected the magnetic dipole effect and only studied the electric dipoles since it was much larger than the magnetic dipole. In future studies, we can come up with a set of solutions when we only take the magnetic dipole into account and neglect the electric dipoles.

In chapter 5 we again studied the thermal property at the mesoscopic level. By the help of the perturbation theory, we managed to get thermal conductivity map of the graphene flake decorated with copper particles using NeSTRI method. We then studied the reason behind the local decrease in thermal conductivity of doped graphene by comparing thermal conductivity maps of the graphene flake at the different stages of the experiment. In the end, we concluded that the local decrease in thermal conductivity of the doped graphene is due to electron-phonon interactions. In future studies, we can decorate the graphene flake with elements like cobalt and palladium in which case we won't have a weakly doped graphene anymore and the momentum

of the phonon is close to the momentum of the electron. By observing the thermal conductivity maps of graphene flake decorated by these elements we can then study their thermal properties.

In chapter 6 we studied the thermal property at the microscopic level. We drew out the mathematical framework for electron-phonon interaction in a graphene flake decorated by copper particles. In our study, we took the electrons to be nonrelativistic and we carried out our calculations in a two-dimensional framework. In future, more complicated research can be done by taking into account by taking electrons moving at high speeds and by assuming a three-dimensional model and figuring out how adding an extra dimension influences the thermal conductivity.

Appendix I

a) Symmetric temperature profile of the substrate

Conducting a change in variables changing $b = c^2$, the integral in Eq. (2.57) would be:

$$T_{b'}(x, y, t) = \frac{q_0 e^{i\omega t}}{k_{th,b}} \int_{-\infty}^{\infty} dc \frac{2c(e^{-\left(\frac{i\omega}{D_b}-c^4\right)^{1/2} x} + e^{\left(\frac{i\omega}{D_b}-c^4\right)^{1/2} x})e^{-c^2|y|}}{\left[\left(\frac{i\omega}{D_b}-c^4\right)^{1/2} - 2c^2\right] \cdot e^{-\left(\frac{i\omega}{D_b}-c^4\right)^{1/2}\frac{L}{2}} - \left[\left(\frac{i\omega}{D_b}-c^4\right)^{1/2} + 2c^2\right] \cdot e^{\left(\frac{i\omega}{D_b}-c^4\right)^{1/2}\frac{L}{2}}} \cdot$$

$$(I.1)$$

To solve the symmetric temperature profile of the substrate we go to the complex space and draw a contour to find the poles necessary to solve the integral.

At first, we study the temperature profile of a 2-dimensional substrate with no thickness. Then we go to the realistic model in hand were the substrate is 3-dimensional. Shrinking the thickness of the substrate to zero makes us have no component in the x direction and Eq. (I.1) would be:

$$T_{b'}(x, y, t) = \frac{2q_0 e^{i\omega t}}{k_{th,b}} \int_{-\infty}^{\infty} dc \cdot \frac{2ce^{-c^2|y|}}{-4c^2}. \tag{I.2}$$

Taking the integral to the complex space and trying to solve it we have:

$$T_{b'}(x, y, t) = -\frac{q_0}{k_{th,b}} \oint dz \frac{e^{-z^2|y|}e^{i\omega t}}{z}. \tag{I.3}$$

The pole would be at $z = 0$. We draw the following contour Figure I.1 to solve Eq. (I.3).
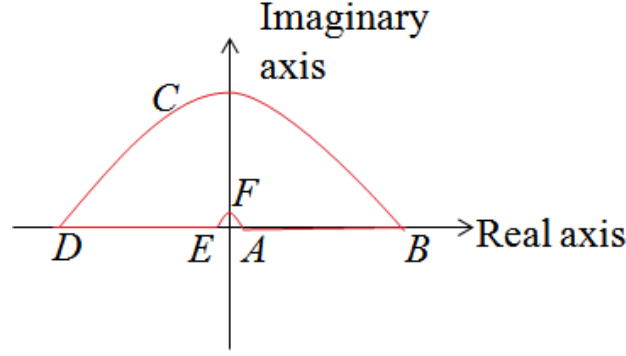
Figure I.1: The contour is drawn to solve Eq. (I.3). We start from A and go all the way to F in a counterclockwise direction.

We start from A and go in a counterclockwise direction. The calculations along the contour are:

$$AB \rightarrow z = c \rightarrow dz = dc, \quad BCD \rightarrow z = \mathrm{Re}^{i\theta} \rightarrow dz = i\,\mathrm{Re}^{i\theta}\,d\theta, \tag{I.4}$$

$$DE \rightarrow z = ce^{i\pi} \rightarrow dz = -dc, \quad EFA \rightarrow z = \varepsilon e^{i\theta} \rightarrow dz = i\varepsilon e^{i\theta}d\theta. \tag{I.5}$$

Inserting these into the integral in Eq. (I.3) we arrive at:

$$T_{b'}(x, y, t) = \frac{q_0 e^{i\omega t}}{k_{th,b}} \int_{-\infty}^{\infty} dc.\frac{e^{-c^2 y}}{-c} = -\frac{i\pi q_0}{k_b} e^{i\omega t} = \frac{q_0}{k_b} \pi e^{i\frac{3\pi}{2}} e^{i\omega t}, \tag{I.6}$$

where we have taken R→∞ and ε→0.

Now we study the realistic case were we have a 3-dimensional thin substrate with the following condition:

$$\left(\frac{i\omega}{D_b} - c^4\right)^{1/2} \frac{L}{2} \ll 1 \Rightarrow e^{(\frac{i\omega}{D_b} - c^4)^{1/2}\frac{L}{2}} = 1 + \left(\frac{i\omega}{D_b} - c^4\right)^{1/2} \frac{L}{2}. \tag{I.7}$$

Therefore the temperature profile in Eq. (I.1) would be:

$$T_{b'}(x, y, t) = \frac{q_0}{k_{th,b}} \cdot$$

$$\int_{-\infty}^{+\infty} dc \frac{2c(e^{-(\frac{i\omega}{D_b}-c^4)^{1/2}x} + e^{(\frac{i\omega}{D_b}-c^4)^{1/2}x})e^{-c^2|y|}e^{i\omega t}}{\left[\left(\frac{i\omega}{D_b}-c^4\right)^{1/2} - 2c^2\right] \cdot \left[1-\left(\frac{i\omega}{D_b}-c^4\right)^{1/2}\frac{L}{2}\right] - \left[\left(\frac{i\omega}{D_b}-c^4\right)^{1/2}+2c^2\right] \cdot \left[1+\left(\frac{i\omega}{D_b}-c^4\right)^{1/2}\frac{L}{2}\right]}.$$

(I.8)

If we put $L=0$ we get the same integral as in Eq. (I.2) for a 2-dimensional substrate. To solve the integral in Eq. (I.8) we go to the complex space as follow:

$$T_{b'}(x, y, t) = -\frac{q_0}{k_{th,b}} \int_{-\infty}^{+\infty} dc \frac{(e^{-(\frac{i\omega}{D_b}-c^4)^{1/2}x} + e^{(\frac{i\omega}{D_b}-c^4)^{1/2}x})e^{-c^2 y}e^{i\omega t} 2c}{\left(\frac{i\omega}{D_b} - c^4\right)L + 4c^2} \Rightarrow$$

$$T_{b'}(x, y, t) = -\frac{2q_0}{k_{th,b}} \oint dz \frac{(e^{-(\frac{i\omega}{D_b}-z^4)^{1/2}x} + e^{(\frac{i\omega}{D_b}-z^4)^{1/2}x})e^{-z^2|y|}e^{i\omega t} z}{\left(\frac{i\omega}{D_b} - z^4\right)L + 4z^2}.$$

(I.9)

To solve the integral in the complex space we have to find the poles, therefore we have:

$$\left(\frac{i\omega}{D_b} - z^4\right)L + 4z^2 = 0 \Rightarrow \Delta = 16 - i\frac{4\omega L^2}{D_b} \Rightarrow z^2 = \frac{+4\pm\sqrt{\Delta}}{L} = \frac{+4\pm(16-4i\frac{\omega L^2}{D_b})^{1/2}}{L}$$

$$z_1 = \pm\frac{\left(+4+(16-4i\frac{\omega L^2}{D_b})^{1/2}\right)^{1/2}}{L^{1/2}} \quad z_2 = \pm\frac{\left(+4-(16-4i\frac{\omega L^2}{D_b})^{1/2}\right)^{1/2}}{L^{1/2}}.$$

(I.10)

The poles in Eq. (I.10) depend on the width of the substrate L, the frequency of the chopper ω which indicates the rate the pump beam illuminates the sample and the thermal diffusivity of the substrate itself D_b. To solve the integral in Eq. (I.9) we draw the following

contour Figure I.2. From the four poles that we find in Eq. (I.10) the two positive poles would fall within the contour boundary.
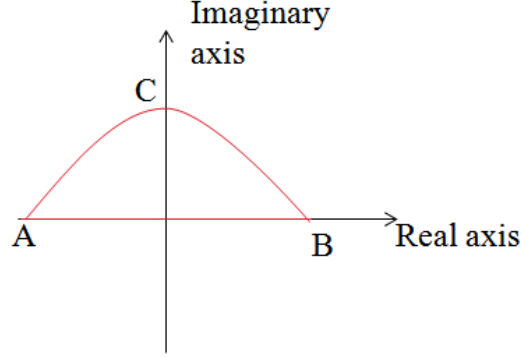

Figure I.2: The contour is drawn to solve Eq. (I.9). Two of the four poles fall within the contour boundary.

Writing Eq. (I.9) with the given contour gives us:

$$T_{b'}(x,y,t) = -\frac{2q_0}{k_{th,b}}\oint dz\, \frac{(e^{-(\frac{i\omega}{D_b}-z^4)^{1/2}x} + e^{(\frac{i\omega}{D_b}-z^4)^{1/2}x})e^{-z^2|y|}e^{i\omega t}z}{\left(\frac{i\omega}{D_b}-z^4\right)L+4z^2} =$$

$$-\frac{2q_0 e^{i\omega t}}{k_{th,b}}\left\{\int_{-\infty}^{+\infty} dc\, \frac{(e^{-(\frac{i\omega}{D_b}-c^4)^{1/2}x} + e^{(\frac{i\omega}{D_b}-c^4)^{1/2}x})e^{-c^2|y|}c}{\left(\frac{i\omega}{D_b}-c^4\right)L+4c^2} + \int_0^{\pi} d\theta\, \frac{(e^{-(\frac{i\omega}{D_b}-R^4 e^{4i\theta})^{1/2}x} + e^{(\frac{i\omega}{D_b}-R^4 e^{4i\theta})^{1/2}x})e^{-R^2|y|e^{2i\theta}}iR^2 e^{2i\theta}}{\left(\frac{i\omega}{D_b}-R^4 e^{4i\theta}\right)L+4R^2 e^{2i\theta}}\right\}$$

.

$$(I.11)$$

By taking a large radius which approaches infinity $R \to \infty$ and by using the residue theorem we have:

$$T_{th,b'}(x,y,t) = 2\pi i\left(\frac{q_0}{k_b}\right)e^{i\omega t}$$

$$\left[\left(e^{-\left(\frac{i\omega}{D_b}-z_1^4\right)^{1/2}x} + e^{\left(\frac{i\omega}{D_b}-z_1^4\right)^{1/2}x}\right)\cdot e^{-z_1^2|y|}\cdot 2z_1 + \left(e^{-\left(\frac{i\omega}{D_b}-z_2^4\right)^{1/2}x} + e^{\left(\frac{i\omega}{D_b}-z_2^4\right)^{1/2}x}\right)\cdot e^{-z_2^2|y|}\cdot 2z_2\right]$$
$$.(I.12)$$

This is the symmetric temperature profile of the substrate.

b) Antisymmetric temperature profile of the substrate

We write Eq. (2.67) as:

$$T_{b'}(x,y,t) = \frac{q_0 e^{i\omega t}}{k_{th,b}} \int_{-\infty}^{\infty} dc \, \frac{2c(e^{\left(\frac{i\omega}{D_b}-c^4\right)^{1/2}x} - e^{-\left(\frac{i\omega}{D_b}-c^4\right)^{1/2}x})e^{-c^2|y|}}{\left[\left(\frac{i\omega}{D_b}-c^4\right)^{1/2} - 2c^2\right]\cdot e^{-\left(\frac{i\omega}{D_b}-c^4\right)^{1/2}\frac{L}{2}} + \left[\left(\frac{i\omega}{D_b}-c^4\right)^{1/2} + 2c^2\right]\cdot e^{\left(\frac{i\omega}{D_b}-c^4\right)^{1/2}\frac{L}{2}}} \quad .\text{(I.13)}$$

We have changed the variable $b = c^2$. As we did for the symmetric temperature profile at first we study the temperature profile of a 2-dimensional substrate with no thickness. Then we go to the realistic model in hand were the substrate is 3-dimensional. Shrinking the thickness of the substrate to zero makes us have no component in the x direction and Eq. (I.13) would be:

$$T_{b'}(x,y,t) = 0. \tag{I.14}$$

This is exactly what we expect since heat is being generated and extracted from the same surface leading the temperature profile to remain zero.

Now solving for the realistic case where we have a 3-dimensional thin substrate with the following condition:

$$\left(\frac{i\omega}{D_b}-c^4\right)^{1/2}\frac{L}{2} \ll 1 \Rightarrow e^{\left(\frac{i\omega}{D_b}-c^4\right)^{1/2}\frac{L}{2}} = 1+\left(\frac{i\omega}{D_b}-c^4\right)^{1/2}\frac{L}{2}. \tag{I.15}$$

By this assumption the temperature profile is:

$$T_{b'}(x,y,t) = \frac{q_0}{k_{th,b}} \int\limits_{-\infty}^{+\infty} dc \frac{2c(e^{(\frac{i\omega}{D_b}-c^4)^{\frac{1}{2}}x} - e^{-(\frac{i\omega}{D_b}-c^4)^{\frac{1}{2}}x})e^{-c^2|y|}e^{i\omega t}}{\left[\left(\frac{i\omega}{D_b}-c^4\right)^{1/2} - 2c^2\right]\cdot\left[1-\left(\frac{i\omega}{D_b}-c^4\right)^{1/2}\frac{L}{2}\right] + \left[\left(\frac{i\omega}{D_b}-c^4\right)^{1/2} + 2c^2\right]\cdot\left[1+\left(\frac{i\omega}{D_b}-c^4\right)^{1/2}\frac{L}{2}\right]}$$

$$\Rightarrow T_{b'}(x,y,t) = \frac{q_0}{k_{th,b}} \int\limits_{-\infty}^{+\infty} dc \frac{2c(e^{(\frac{i\omega}{D_b}-c^4)^{\frac{1}{2}}x} - e^{-(\frac{i\omega}{D_b}-c^4)^{\frac{1}{2}}x})e^{-c^2|y|}e^{i\omega t}}{2\left(\frac{i\omega}{D_b}-c^4\right)^{1/2} + 2c^2\left(\frac{i\omega}{D_b}-c^4\right)^{1/2}L}.$$

(I.16)

In order for us to solve this integral, we again go to the complex space and write the temperature profile as:

$$T_b(x,y,t) = \frac{q_0}{k_{th,b}} \oint dz \frac{2z(e^{(\frac{i\omega}{D_b}-z^4)^{\frac{1}{2}}x} - e^{-(\frac{i\omega}{D_b}-z^4)^{\frac{1}{2}}x})e^{-z^2|y|}e^{i\omega t}}{2\left(\frac{i\omega}{D_b}-z^4\right)^{1/2} + 2z^2\left(\frac{i\omega}{D_b}-z^4\right)^{1/2}L}.$$ (I.17)

To solve the integral in the complex space we should first find the poles of the integral in Eq. (I.17). Finding the poles we have:

$$2\left(\frac{i\omega}{D_b}-z^4\right)^{1/2} + 2z^2\left(\frac{i\omega}{D_b}-z^4\right)^{1/2}L = 0 \Rightarrow z^2 = -\frac{1}{L} \Rightarrow z_3 = \overset{+}{\underset{-}{}} i\sqrt{\frac{1}{L}}.$$ (I.16)

From Eq. (I.16) we see that the poles depend on the width of the substrate L, the frequency of the chopper ω which indicates the rate the pump beam illuminates the sample and the thermal diffusivity of the sample itself D_b. To solve the integral in Eq. (I.17) we draw the same contour as the previous case for finding the symmetric temperature profile Figure I.2. From the two poles that we find in Eq. (I.16) one of them would be within the contour that has been drawn. Writing Eq. (I.15) with the given contour gives us:

$$T_b(x,y,t) = \frac{q_0}{k_{th,b}} \oint dz \frac{(e^{(\frac{i\omega}{D_b}-z^4)^{\frac{1}{2}}x} - e^{-(\frac{i\omega}{D_b}-z^4)^{\frac{1}{2}}x})e^{-z^2|y|}e^{i\omega t}z}{\left(\frac{i\omega}{D_b}-z^4\right)^{1/2} + z^2\left(\frac{i\omega}{D_b}-z^4\right)^{1/2}L} =$$

99

$$\frac{q_0 e^{i\omega t}}{k_{th,b}} \left\{ \int_{-\infty}^{\infty} dc \frac{(e^{(\frac{i\omega}{D_b}-c^4)^{\frac{1}{2}}x} - e^{-(\frac{i\omega}{D_b}-c^4)^{\frac{1}{2}}x})e^{-c^2|y|}c}{\left(\frac{i\omega}{D_b}-c^4\right)^{1/2} + c^2\left(\frac{i\omega}{D_b}-c^4\right)^{1/2}L} + \int_{0}^{\pi} id\theta \frac{(e^{(\frac{i\omega}{D_b}-R^4 e^{4i\theta})^{\frac{1}{2}}x} - e^{-(\frac{i\omega}{D_b}-R^4 e^{4i\theta})^{\frac{1}{2}}x})e^{-R^2 e^{2i\theta}|y|}R^2 e^{2i\theta}}{\left(\frac{i\omega}{D_b}-R^4 e^{4i\theta}\right)^{1/2} + R^2 e^{2i\theta}\left(\frac{i\omega}{D_b}-R^4 e^{4i\theta}\right)^{1/2}L} \right\}$$

.

$$\tag{I.17}$$

By taking a large radius which approaches infinity $R\to\infty$ and by using the residue theorem we have:

$$T_b(x, y, t) = 2\pi i \left(\frac{q_0}{k_{th,b}}\right) e^{i\omega t} \left(e^{\left(\frac{i\omega}{D_b}-z_3^4\right)^{1/2}x} - e^{-\left(\frac{i\omega}{D_b}-z_3^4\right)^{1/2}x} \right) \cdot e^{-z_3^2|y|} z_3 .$$

$$\tag{I.18}$$

This is the antisymmetric temperature profile.

Appendix II

The objective of this section is to demonstrate the genuineness of the amplitude and phase images measured using our experimental apparatus, and show they are originating from thermoreflectance oscillations at the air-sample interface, and not from scanning near-field artefacts, including periodic changes of the tip-surface distance due to the periodic thermal expansion of the sample.

To this end, a set of negative test samples, consisting of thermally evaporated aluminum thin films, have been deposited and analyzed. These samples were designed as shown in Figure II.1, with a step between a large (several cm^2) and 20-nm thick Al thin film, and an equally large, but thicker (D = 40 nm, 68 nm, or 80 nm), Al film on the right. Samples were prepared by thermal evaporation of Al pellets (K.J. Lesker) in a vacuum chamber integrated to a glovebox operating in a nitrogen atmosphere (Nexus II, Vacuum Atmospheres Co.) that is described elsewhere[1]. A uniform, the 20-nm film is initially grown on glass, and the growth rate is checked using a Sycom STM2 quartz crystal monitor. As soon as the desired thickness is reached, a part of the sample is masked, and the deposition continues on the unmasked side of the sample until the desired thickness D is reached. All samples were measured by NeSTRI, as described in the experimental section of the paper. The presence of a similar, 20-nm thick, region in all of the samples serves as a reference control for the NeSTRI amplitudes and ensures that measurements performed on different samples are comparable.

Our goal is to demonstrate that all these samples produce NeSTRI images, with amplitudes that are proportional to the volumetric heat that is locally generated within each sample and phases that are independent of the sample thickness. Our negative test samples will ensure that the thermal properties obtained from NeSTRI images do not depend on the sample geometry, but only on the material properties of aluminum. In addition, these experiments are useful to rule out near-field optical artefacts due to periodic thermal dilatation of the samples at the same frequency of the pump beam pulses used for sample heating. If thermal dilatation could not be neglected, it would produce a shift $\delta z(\omega)$ of the sample surface that is proportional to the sample thickness D. A subsequent change of the tip-sample distance, $z_0 - \delta z(\omega)$, will then occur. Consequently, signal amplitudes due to thermal dilatation artefacts would be proportional to the film thickness:

$$\delta\rho_0 \propto D. \tag{II.1}$$

Conversely, in the case of a genuine NeSTRI signal, the equation of heat (Eq. 3.4) for a uniform thin film region becomes

$$c_{Al}\, dT(t)/dt = H_0 \exp(i\omega t), \tag{II.2}$$

where c_{Al} [J/m^3/K] is the volumetric specific heat of Al and H_0 [W/m^3], the heat generated per unit volume of the sample corresponds to the amount of light being absorbed by the entire cross section of an Al thin film at the pump-beam wavelength of 405 nm:

$$H_0 = (P_0/D^2) \int_0^D \exp(-\alpha_{Al}z)\, dz = [P_0/(\alpha_{Al}D^2)][1- \exp(-\alpha_{Al}D)], \tag{II.3}$$

Where P_0 [in W/m^2] is the photon flux of the pump beam, and $\alpha_{Al} = 1.5\ 10^8$ m^{-1} is the optical absorption coefficient of Al at 405 nm, the pump beam wavelength. As discussed in the text, a tentative uniform solution of the form

$$\delta\rho(t) = -hT(t) = -hT_0 \exp[i(\omega t - \delta\varphi_0)] = \delta\rho_0 \exp[i(\omega t - \delta\varphi_0)] \tag{II.4}$$

can be sought and replaced into Eq. II.2. In Eq. II.4, h is a proportionality coefficient (see Supplementary Information Section 1) and $\delta\rho(t)$ is the oscillatory thermoreflectance signal of amplitude $\delta\rho_0$ and phase $\delta\varphi_0$, caused by temperature oscillations of amplitude T_0. By replacing eqs. II.3 and II.4 into Eq. II.2, we then obtain

$$\delta\rho_0 = hP_0/(\omega c_{Al}\alpha_{Al}D^2)[1- \exp(-\alpha_{Al}D)]$$

$$\delta\varphi_0 = -90^0 = const(D). \tag{II.5}$$

Contrarily to Eq. II.1, Eq. II.5 indicates that genuine NeSTRI amplitude signals decrease at increasing thickness because of lower power density generated in thicker and more voluminous samples, which produce smaller temperature raises. This can be appreciated from II.1, which shows that the left (20-nm thick) side of the image of $\delta\rho_0$ exhibits a significantly higher amplitude of the right side (40-nm thick) of the image. Conversely, the image of $\delta\varphi_0$ does not exhibit any significant difference or thickness dependence far away from the interface between the two thicknesses. Since Eq. II.5 indicates that $\delta\rho_0$ does not depend on the thermal conductivity k in a homogeneous and flat region, but only on the volumetric specific heat c, the information on k contained in $\delta\varphi_0(x, y)$, for values of x within a few thermal diffusion lengths in the proximity of an edge, are critical to determine k in uniform thin films by NeSTRI.
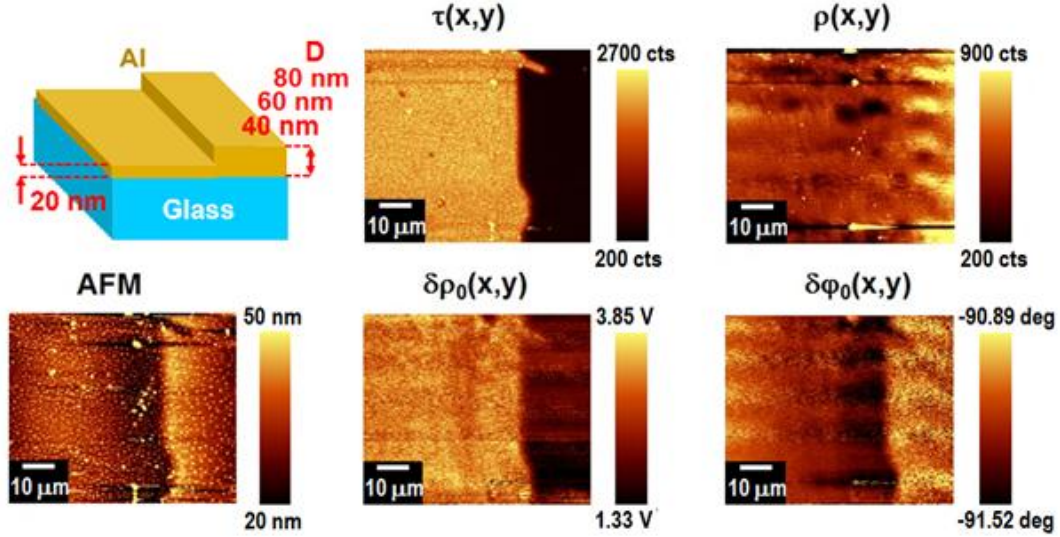
II.1. *The geometry of negative test samples, with corresponding 405-nm SNOM images in transmittance (τ) and reflectance (ρ). AFM shows that images are taken at the edge between 20-nm thick and 40-nm thick Al regions. The granular structures of aluminum present on both regions are not visible in the thermal images, of which the phase ($\delta\varphi_0$) becomes thickness-independent at ~30 μm from the edge, while the amplitude ($\delta\rho_0$) decreases with thickness accordingly to Eq. II.5.*
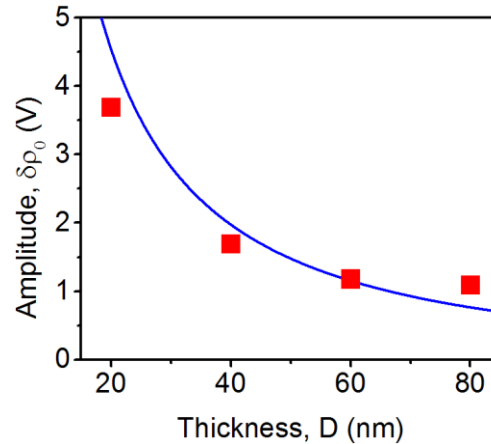
II.2. NeSTRI signal amplitude ($\delta\rho_0$) as a function of Al thin film thickness (D). The blue line is a data fitting accordingly to Eq. II.5. The fact that $\delta\rho_0$ decreases at increasing D, as well as the good quality of the fit, are a strong indication of the genuineness of the NeSTRI signal, originated from thermoreflectance effects at the air-sample surface. Conversely, near-field optical artefacts would have led $\delta\rho_0$ to increase proportionally to the thin-film volume per unit surface area and, consequently, with D.

103

The findings presented in II.1 are quantified and further substantiated in II.2 that reports the NeSTRI signal amplitude as a function of Al thickness for the entire set of negative test samples. The blue line in II.1 is a data fitting accordingly to Eq. II.5. The fitting quality is remarkably good, which is an additional strong indication that the NeSTRI signal originates from thermoreflectance effects at the air-sample surface, and not from thermal expansion artefacts that would have led the amplitude of the signal to linearly increase with D. Finally, from II.1, it is apparent that the granular Al structures that can be observed in the AFM image are also reproduced in the reflection (ρ) and transmission (τ) SNOM images, but do not significantly affect the NeSTRI images, neither in phase nor amplitude. We can thus infer that NeSTRI is free from nano-optical artefacts[2] producing images that are mere optical readouts of the AFM topography.

[1]   S. Ezugwu, MSc Thesis, The University of Western Ontario (2012) – Available online at http://ir.lib.uwo.ca/etd/1025/ (consulted: Feb-14-2017)

[2]   P.G. Gucciardi and M. Colocci, Appl. Phys. Lett. (2001) 79, 1543-1545

<div align="center">

Sina Kazemian

Curriculum Vitae

</div>

Educations

2013 – 2017	*University of Western Ontario*, London, ON, Canada, Doctor of Philosophy (Ph.D.), Physics

- Adviser: Prof. Giovanni Fanchini
- Thesis titled: "Modelling the thermal conductivity of layered materials from photothermal measurements"
- Average Grade: 90/100, (Electrodynamics [Jackson] : 90/100, Mathematical Methods in Physics [Group theory and Lie Algebra]: 96/100)
- Achievements: Succeeded in the written and oral comprehensive exam; Western Graduate Research Scholarship

2010 – 2012	*Shahid Beheshti University*, Tehran, Iran, Master of Science (M.Sc.), Physics Gravitation and Astrophysics

- Adviser: Prof. Shahram Jalalzadeh
- Thesis titled "Super Symmetry and Quantum Cosmology"
- Average Grade: 16.13/20, (Advanced General Relativity: 18/20)

2006 – 2010	*Shahid Beheshti University*, Tehran, Iran, Bachelor of Science (B.Sc.), Physics

- Adviser: Prof. Hosein Shojaie
- Average Grade of the last 2 years: 16/20
- Project titled "The Thermodynamics Properties of Black Holes"

Research Experiences

2013 – Present	*University of Western Ontario*, London, ON, Canada Research Assistant
2010 – 2012	*Shahid Beheshti University*, Tehran, Iran, Research Assistant
2009 – 2010	*Shahid Beheshti University*, Tehran, Iran, Undergraduate Researcher

Publications

Papers Published	
Feb-2017	**Contactless scanning near-field thermoreflectance imaging;** *Sina Kazemian, Sabastine Ezugwu, Dong-Yup William Choi, Giovanni Fanchini, (The first two authors contributed equally)* ***Nanoscale Journal***

Papers in preparation	
Nov-2017	**Near-field imaging of electron-phonon coupling at the nanoscale and its role in limiting the lattice thermal conductivity of graphene;** *Sina Kazemian, Sabastine Ezugwu,Giovanni Fanchini, (The first two authors will be contributed equally)*
Dec-2017	**The effect of electron phonon scattering in lattice conduction from a quantum field approach;** *Sina Kazemian,Giovanni Fanchini*
Feb-2018	**Thermal conductivity of metallic thin films on a substrate by two-side Photothermal Deflection Spectroscopy measurements;** *Sina Kazemian, Reg Bauld, Giovanni Fanchini*

Unpublished Research	
2013	**Weyl Theory for the combination of Gravitational-Electromagnetic Fields;** *Sina Kazemian, Saeed Gravi, Shahram Jalalzadeh,*

Presentations

Aug.2017	Canadian Semiconductor Science and Technology Conference (CSST), Electron-phonon coupling at the nanoscale in graphene, Waterloo University
Jul.2016	Canadian Association of Principals conference (CAP), Contactless thermal imaging in nanoscale, *Ottawa University*
Aug.2015	Canadian Semiconductor Science and Technology Conference (CSST), Near Filed Scattering, Sherbrooke University